DESIGN, CONSTRUCTION AND EXPERIMENTAL STUDIES

WITH AN S-BAND PHOTOINJECTOR

By

SHANKAR LAL

Enrolment number: PHYS03200704007

Raja Ramanna Centre for Advanced Technology

Indore-452013

India

A thesis submitted to the

Board of Studies in Physical Sciences

In partial fulfillment of requirement

for the Degree of

DOCTOR OF PHILOSOPHY

Of

HOMI BHABHA NATIONAL INSTITUE

September, 2013

Homi Bhabha National Institute

Recommendation of the Viva Voce Board

As members of the Viva Voce Board we certify that we have read the dissertation prepared by Shankar Lal entitled **"Design, Construction and Experimental Studies with an S-band Photo-injector"** and recommended that it may be accepted as fulfilling the dissertation requirement for the Degree of Doctor of Philosophy.

______________________ Date: 13.3.2015

(Chairman – Prof. S. B. Roy, RRCAT, Indore)

______________________ Date: 13/3/15

(Guide – Prof. S. Krishnagopal, BARC, Mumbai)

______________________ Date: ———

(Member 1 – Prof. P. Singh, BARC, Mumbai)

______________________ Date: 18/3/2015

(Member 2– Prof. V. S. Pandit, VECC, Kolkata)

______________________ Date: 13/3/2015

(Member 3 – Prof. V. Kumar, RRCAT, Indore)

______________________ Date: 13/3/2015

(Co-opted Member – Prof. P. A. Naik, RRCAT, Indore)

______________________ Date: 13/3/2015

(External Examiner – Prof. R. G. Pillay, TIFR, Mumbai)

Final approval and acceptance of this dissertation is contingent upon the candidate's submission of the final copies of the dissertation to HBNI.

I hereby certify that I have read this dissertation prepared under my supervision and recommended that it may be accepted as fulfilling the dissertation requirement.

Date: 13/3/2015
RRCAT, INDORE

Guide: ______________________

STATEMENT BY AUTHOR

This dissertation has been submitted in partial fulfillment of requirements for an advanced degree at Homi Bhabha National Institute (HBNI) and is deposited in the Library to be made available to borrowers under rules of the HBNI.

Brief quotations from this dissertation are allowable without special permission, provided that accurate acknowledgement of source is made. Requests for permission for extended quotation from or reproduction of this manuscript in whole or in part may be granted by the Competent Authority of HBNI when in his or her judgment the proposed use of the material is in the interests of scholarship. In all other instances, however, permission must be obtained from the author.

शंकर लाल

(Shankar Lal)

DECLARATION

I hereby declare that the investigation presented in the thesis has been carried out by me. The work is original and has not been submitted earlier as a whole or in part for a degree/diploma at this or other Institution/University.

(Shankar Lal)

List of Publications arising from the thesis

Journal

1. "A new two-step tuning procedure for a photocathode gun" , **Shankar Lal**, K. K. Pant, S. Krishnagopal, Nuclear Instruments and Methods in Physics Research, A592 (**2008**), 180-188.

2. "A novel scaling law relating the geometrical dimensions of a photocathode RF gun to its RF properties", **Shankar Lal**, K. K. Pant and S. Krishnagopal, Review of Scientific Instruments, **82**,123304 (**2011**), 1-10.

3. "Brazing of photocathode RF gun structures in Hydrogen atmosphere: Process qualification, effect of brazing on RF properties and vacuum compatibility", Ajay Kak, P. K. Kulshreshtha, **Shankar Lal**, Rakesh Kaul, P Ganesh, K K Pant and Lala Abhinandan, Journal of Physics: Conference Series **390** (**2012)** 012025,1-6.

Conferences

1. "Thermal Simulation of a Laser Photocathode rf gun", B. Biswas, **Shankar Lal**, K. K. Pant, Arvind Kumar and S. Krishnagopal, in Proceedings of Asian Particle Accelerator Conference 2007, January 29-February 2, **2007**, Indore, India, pp 482.

2. "Tuning of the waveguide to cavity coupling coefficient for a PWT linac and a photocathode gun", S. Krishnagopal, **Shankar Lal**, K. K. Pant, Umesh Kale, in Proceedings of European Particle Accelerator Conference 2008, Genoa, Italy, **2008**, pp.2734.

3. "Development of Brazing technique for a 1.6 cell BNL/SLAC/UCLA type phocathode guns by hydrogen brazing", Ajay Kak, P. K. Kulshreshtha, **Shankar Lal,** Proceedings of Indian Particle Accelerator Conference 2009, RRCAT, Indore, **2009**.

4. "An analytical formulation for prediction of geometrical dimensions of a photocathode gun for desired RF properties", **Shankar Lal,** K. K. Pant, BP&FEL Lab., MAASD, RRCAT, Indore, India, S. Krishnagopal, NPD, BARC, Mumbai, India, in Proceedings of International Particle Accelerator Conference 2010, Kyoto, Japan, **2010**, pp. 3679-81**.**

5. "Brazing of Photocathode RF gun structures in Hydrogen atmosphere: Process qualification, Effect of brazing on RF properties, and Vacuum compatibility", Ajay Kak, P. K. Kulshreshtha, **Shankar Lal**, Rakesh,Kaul, P. Ganesh, K. K. Pant and Lala Abhinandan, in Proceedings of the International Vacuum Symposium 2012, VECC, Kolkata, **2012.**

(Shankar Lal)

I dedicate this work

To

My Family

ACKNOWLEDGMENTS

There are many people I need to acknowledge for their support, contribution and direct/indirect involvement in the production of this thesis.

I am extremely thankful to my thesis guide ***Dr. S. Krishnagopal,*** for his valuable guidance, constant support, encouragement, motivation throughout my entire Ph. D. I sincerely thank him for his valuable suggestions and sharing his abundance of knowledge with me without which it was not possible to complete the thesis work. I also thank him for correcting and proofreading of various drafts of this thesis and synopsis which helped me to present the research work in coherent manner.

I would also like to thank ***Dr. K. K. Pant***, Head Free-Electron Laser Laboratory, RRCAT for his great efforts, valuable suggestions and deep involved support in the theoretical analysis, fabrication, RF characterization, brazing and vacuum testing of the photocathode RF gun structures. I also thank him for his help to analysis and interpretation of experimental results to present in form of research papers.

My sincere thanks are due to ***Mr. Bhaskar Biswas*** for his support by doing thermal simulations and design of magnetic elements presented in this thesis, to ***Dr. Arvind Kumar*** for his guidance and support in performing the 2-D electromagnetic and beam dynamics simulations, and to ***Dr. Vinit Kumar*** for useful discussions and critical comments.

I would also like to thanks ***Mr. S. Chouksay***, and ***Mr. Saket Kumar Gupta*** of Mechanical Design and Engineering Laboratory, RRCAT for their support in preparing mechanical drawings of the photocathode RF gun and other beam line components.

I express my thanks to staff of Accelerator Workshop, Chemical Treatment Facility and Accelerator Components Design and Fabrication Section of RRCAT for their support during development of the photocathode RF gun structures.

I am extremely tankful to ***Mr. Ajay Kak*** and ***Mr. P.K. Kulshreshtha*** for their support in brazing the gun structures.

I would like to thank ***Dr. S. B. Roy***, Head, Material Advanced Accelerator Science Division (MAASD) and ***Dr. P. D. Gupta***, Director, RRCAT for supporting the activities related to this research and development work.

My thanks are due to my colleagues ***Mr. Umesh Kale***, ***Mr. Pravin Nerpagar, Mr. Rajkumar Bhart Bhowate***, ***Mr. Akhil Patel***, ***Mr. Ravi Kumar Pandit, Mr. Mohammad Khursheed*** and ***Mr. A. K. Sarkar*** for their valuable support and help at different stages of this work and for providing friendly environment.

I take this opportunity to thank former FEL Lab members ***Mr. V. Kodiarasan***, ***Mr. Rohin Parkar*** and ***Miss. Partima Jain*** for their help during tuning and RF measurements.

I also thank M/s National Engineering Works, Indore for fabrication of prototypes of the photocathode RF gun structures and M/s IGTR, Aurangabad for machining of final photocathode RF gun structures.

I render my thanks to doctoral committee members ***Dr. K. C. Mittal***, ***Dr. P. Singh, Dr. V. S. Pandit*** and ***Dr. Vinit Kumar*** for their constructive advice and useful discussions.

I am extremely thankful to my wife ***Pushpa*** for the support she had extended during this work. I also thank my daughters ***Aanchal*** and ***Saanvi*** for loan my computer to me at home for writing the thesis and providing unconditional love to bring smile on my face at home that I will always crave. I would like to express my sincere gratitude to my parents, my brother, his family and friends for their never ending love and affection to me.

There are many people that I wish to thank who have helped me to completing this thesis work. Although I do not mention by name, you are not forgotten –thanks you all!

(Shankar Lal)

CONTENTS

Page No.

SYNOPSIS

Homi Bhabha National Institute

Ph. D. PROGRAMME

1. **Name of the Student:** SHANKAR LAL
2. **Name of the Cconstituent Institution:** Raja Ramanna Centre for Advanced Technology, Indore
3. **Enrolment No.:**PHYS03200704007
4. **Title of the Thesis:** Design, Construction and Experimental Studies with an S-band Photoinjector
5. **Name of guide:** Prof. Srinivas Krishnagopal
6. **Board of Studies:** Physical Sciences

High-brightness (high current, low emittance) electron beams are required for many applications such as short-wavelength Free-Electron Lasers (FELs), injectors for synchrotron radiation sources, particle colliders, plasma wake-field accelerators, energy recovery linacs, laser Compton scattering, etc. Applications to particle colliders and Self Amplified Spontaneous Emission (SASE) FELs particularly impose stringent requirements on the electron beam in terms of high brightness and short bunch length. Photocathode RF guns have proven to be promising sources of high brightness electron beams and many laboratories worldwide have successfully developed and used photo-injector technology for such applications.

The Raja Ramanna Centre for Advanced Technology (RRCAT) in India is a light source lab with ongoing Research and Development activities related to Synchrotron Radiation Sources (SRS) and free-electron lasers (FELs). Hence, it was decided to initiate activity for in-house development of photoinjectors that could prove to be useful in future accelerator projects of the Centre. After studying existing literature, it was proposed to focus on the design and development of a BNL/SLAC/UCLA Gun-3 design of a 1.625 cell photocathode RF gun which has demonstrated generation of electron beams with an emittance as low as 1π mm-mrad employing the emittance compensation technique first proposed by B.E. Carlsten in 1989.

The motivation for the present dissertation is: (i) to study and understand RF design issues related to photocathode RF gun design, (ii) to identify critical issues related to the development and tuning of photocathode guns for a desired set of RF properties, and to perform analytical/experimental studies to address these issues, and (iii) to develop and characterize a photocathode RF gun for possible future use as an injector for a light source or FEL.

A study of existing literature reveals that beam emittance for the BNL/SLAC/UCLA Gun-3 design is minimum when the ratio of on-axis accelerating field in the half-cell and that in the full-cell (defined as field balance e_b) is unity. RF efficiency is a maximum when waveguide to cavity coupling coefficient (β_π) is also unity for the desired 'π-mode' of operation with a frequency f_π, which is 2856 MHz for our case. Hence, design and tuning of a photocathode RF gun involves RF design using available 2-D and 3-D codes to obtain the desired geometrical dimensions of the RF structure, and subsequently tuning of the machined structure for the desired RF parameters discussed above.

Literature also reveals that in spite of employing 3-D simulations codes to design a photocathode RF gun for a desired set of RF properties, inherent inaccuracies/limitations of the codes and machining imperfections can result in significant deviation in RF properties of the final structure from desired values. Conventionally, an iterative cut-and-measure technique is employed to tune a photocathode gun. In this method, alternate steps of measurement of RF properties and machining of some geometrical dimensions of independent cells is done till the desired set of RF properties is achieved for the gun. Since multiple RF parameters are to be achieved simultaneously, this procedure is slightly involved for a photocathode RF gun due to the strong inter-dependence of its different RF parameters.

Better appreciation of the above problems was obtained by carrying out actual tuning of aluminum prototypes of a photocathode RF gun using the iterative cut-and-measure technique. Initial dimensions of these prototypes were determined by employing 2-D and 3-D codes to target a higher frequency for the π-mode and a lower β_π. This gave us margin for tuning the resonant frequency by taking machining cuts on the inside diameters of the cells, and for tuning of β_π by taking machining cuts on the slot dimensions. Our study revealed that if the RF parameters of independent cells, required for a desired set of RF parameters for the π mode operation of the gun, can be determined precisely in advance, tuning of the gun is simplified considerably since the problem introduced in tuning due to the inter-dependence of different RF parameters of the gun is eliminated. Our first analytical study focused on this issue of tuning of a photocathode RF gun.

To predict the dependence of RF parameters of a gun on independent cell RF parameters, we performed an analytical study by representing it as an LCR equivalent circuit. Earlier LCR circuit analyses of coupled RF cavities have incorporated the inter-cell coupling and predicted the dependence of f_π and e_b on independent-cell resonant frequencies. However, these studies do not simultaneously consider the desired waveguide-to-cavity coupling coefficient. Similarly, J. Gao has analytically studied coupling of a single cell to waveguide to predict the dimensions of the RF coupling slot for a desired value of the waveguide-to-cavity coupling coefficient β. However, this cannot be applied directly to a photocathode RF gun since it also involves coupling of two RF cavities. In our analysis, we have simultaneously studied the inter-cell coupling as well as waveguide to cavity coupling for a two-cell structure with RF power coupling in one cell to predict the dependence of RF parameters of gun (f_π, e_b and β_π) on independent cell resonant frequencies and independent full-cell to waveguide coupling coefficient. The analysis requires the value of quality factor (Q) and shunt impedance (R) of both the cells, and the inter-cell coupling coefficient (k_{fh}). Two cases have been studied where, in the first case these values have been taken from electromagnetic simulations, and in the second case, these values have been measured experimentally, as discussed later. While the first method is easy and straightforward, it is not accurate since it does not consider the effect of inaccuracies of the code or machining errors, which can significantly affect the values of Q, R and inter-cell coupling. In the second method, the quality factor and shunt impedance of independent cells are measured experimentally by de-coupling the cells by detuning one of the cells and making the measurement on the other cell. The inter-cell coupling k_{fh} is determined by measuring the FB and frequency of the π-mode. With these measured values, our analysis predicts that to achieve f_π =

2856 MHz with e_b and β_π both equal to unity, the independent half-cell should be tuned to 2854.3 MHz while the full-cell should be tuned to 2854.8 MHz with an independent full-cell to waveguide coupling coefficient (β_f) of 1.62. This analysis has been verified experimentally on a prototype RF gun by a 'simulated tuning' procedure prior to final tuning by taking machining cuts. This procedure involved tuning of the independent cell frequencies to predicted values by inserting plungers to obtain desired values for f_π and e_b. Since the independent full-cell to waveguide coupling coefficient could not be tuned using plungers, the waveguide to gun coupling coefficient β_π could not simultaneously be tuned to unity. However, the measured ratio of waveguide to cavity coupling coefficient for the π-mode to that of the independent full-cell agrees well with our analytical prediction.

A new two step tuning procedure has now been established to tune a photocathode RF gun which involves the following steps: (1) prediction of the required independent cell RF parameters (f_h, f_f, β_f) for a desired set of RF parameters of the gun using our analytical formulation, (2) tuning of the half-cell for required f_h and the full-cell for the required f_f and β_f. The assembled gun has the desired set of RF parameters f_π, e_b, and β_π. This method has been successfully used to tune true-to-scale aluminum and ETP copper prototypes of a photocathode RF gun, and a paper on this work has been published in Nucl. Instrum. Methods A.

Although the two step tuning procedure significantly simplifies the tuning of a photocathode RF gun, independent cell RF parameters (f_h, f_f, and β_f) still have to be tuned by employing the iterative cut-and-measure technique, which is not desirable as finish-machined cells are subjected to multiple machining cuts. To avoid this, the two-step tuning procedure has been further extended to predict the geometrical dimensions of independent gun cells, viz. ID of half-cell (Φ_h), ID of full-cell (Φ_f) and length of RF coupling slot (L_{RF}), to achieve a desired set of independent cell RF parameters (f_h, f_f and β_f). Since the gun cell geometries are different from a pillbox cavity due to presence of inter-cell coupling iris and beam exit port, the variation in resonant frequency has been modeled as $f_i = a_i R_{ci}^{-bi}$, where a_i and b_i are constants and depend upon the geometry of the i^{th} cell. The values of the constants in the above expression can be calculated either by performing a SUPERFISH simulation with different radius of a particular cell while the other cell is detuned, or by machining the cells to be slightly undersized and measuring the independent cell resonant frequencies for two different radii. The second approach gives a more accurate result as machining errors in the profiles of cell geometries are automatically incorporated. Once the values of constants are known, the ID of independent cells can be predicted for any desired resonant frequency. Tuning of β_f for the independent full-cell can be done by employing J. Gao's scaling law to predict the desired dimensions of RF coupling slot.

Although the independent cell resonant frequency mainly depends upon its ID, it is also affected by the presence of different ports openings, *viz.* vacuum port, RF power coupling port, and laser ports. The variation in resonant frequency of an independent cell due to port openings can be calculated by employing Slater's perturbation theorem or Gao's scaling law. Incorporating this effect due to port openings, our scaling law for independent cell resonant frequency is modified to $f_i = a_i R_{ci}^{-bi} \sum \left(1 - \Delta f_n\right)$, where Δf_n is the variation in resonant frequency due to the n^{th} port, which depends upon the shape and size of the port. The half-cell contains two elliptical ports for the laser, while the full-cell contains one oblong port for RF power feeding, one oblong port for vacuum pumping and two circular ports for frequency tuning. The variation in half-cell frequency due to the laser ports is expected to be only ~ 85 kHz and tuning of the half-cell is achieved by taking machining cut on its ID. On the other hand, tuning of the full-cell is complicated as the perturbation of its resonant frequency due to slots at the RF and vacuum ports is significant, and the dimensions of these slots are also varied in the tuning process to simultaneously tune the β_f.

If the length of the RF coupling slot is increased to tune β_f after tuning the full-cell for the desired frequency, it causes a reduction of the full-cell frequency, which can only be compensated by further reducing the ID of full-cell, which is not possible. Similarly, if the resonant frequency of the full-cell is tuned to the desired value after tuning the β_f to the desired value, it causes an increase in β_f which needs to be compensated by reducing the length of the RF coupling slot, which is again not possible. Hence, simultaneous tuning of both f_f and β_f needs to be done while tuning the independent full-cell. To incorporate this inter-dependence of f_f and β_f, the analysis has been further extended by incorporating the effect of length of RF coupling slot on f_f and effect of ID on β_f. Finally, two coupled equations have been formulated, the solution of which give the required values of full-cell ID and length of RF coupling slot to achieve the desired values of f_f and β_f simultaneously.

Since the desired RF parameters f_π, β_π and e_b have to be achieved after brazing and under vacuum, while tuning is usually done before brazing and in air, the change in physical condition after brazing and also in the dielectric constant from air to vacuum varies the RF parameters of the gun. Hence the contributions of these two effects have to be incorporated in predicting the independent cell RF parameters for a desired set of RF parameters for the gun. A brazing clearance of 25-50 μm, usually maintained at the location of brazing joint between the full- and half-cells, is present during the initial tuning, but is filled up after brazing. This change affects the f_f and β_f only as the brazing joint affects only the full-cell geometry. The change in frequency due to vacuum can be calculated analytically by employing LC-circuit analogy where the value of capacitance is changed due to a change of the dielectric constant. This analysis predicts that the resonant frequency of the π-mode is increased by 0.842 MHz when the gun is pumped down from atmosphere to vacuum. Hence, if the desired f_π under vacuum is 2856 MHz, one has to target 2856 - 0.842 = 2855.158 MHz during tuning in air. The variation in f_f due to brazing is estimated by conducting SUPERFISH simulations by varying the brazing clearance. The study predicts that f_f decreases linearly with brazing clearance with a gradient of -0.127 MHz/10 μm. The study also predicts that the variation in β_f is like as step function and it becomes 1.17 times its value before brazing. After incorporating these effects of vacuum and brazing, the geometrical dimensions of the gun cells are predicted in order to achieve the desired RF parameters under operational conditions. This analysis effectively eliminates the need of 3-D electromagnetic simulations and considerably simplifies the tuning of a photocathode RF gun. Using this analysis, two photocathode RF gun structures have been successfully developed and tuned, and a paper on this work has been published in Rev. Sci. Instrum.

Since the scope of the dissertation also included development of a photocathode RF gun structure for possible future use as an injector for a light source or FEL, a brazing procedure has been established by brazing multiple true-to-scale prototypes after tuning by the procedure formulated by us. The gun is brazed in hydrogen atmosphere in two steps and the brazing joints on prototypes have been qualified by vacuum testing of the brazed structure and subsequent destructive tests on the joints. The leak test of the brazed gun structures demonstrate a leak rate of the order of 10^{-10} mbar l/s. Work on the development of the brazing procedure has been published in Journal of Physics-Conference Series.

The RF characterization of the photocathode RF guns has been done by measuring its RF parameters like resonant frequency, quality factor and waveguide to cavity coupling coefficient using a Vector Network Analyzer (VNA). The on-axis accelerating field profile has been measured by conducting bead perturbation experiments from which shunt impedance and field balance have been determined. A high power RF conditioning setup comprising one FCT, bending magnet based energy analyzer and two beam profile monitors has been designed and developed. This setup has been pumped down by using three ion pumps to achieve vacuum of 3×10^{-8} mbar. An electron beam transport line with an emittance compensation solenoid has been also been designed and developed, and a vacuum of 10^{-8} mbar has been achieved in this line. The development of the high power RF system required for testing of the gun is in an advance stage.

The organization of the dissertation is as follows:

Chapter 1 gives an overview of different electron sources ranging from DC guns to photocathode RF guns. A review of the basics of RF accelerating structures including figures of merit like resonant frequency, quality factor, shunt impedance, transit time factor, RF power coupling coefficient etc. and experimental techniques used for measuring the RF parameters of gun is presented in **Chapter 2**. The theory of photocathode RF guns and an analytical approach to fix the RF parameters for desired beam qualities are described in **Chapter 3**. The RF design to determine the geometrical dimensions and the associated tolerances for fabrication of the gun structures is presented in **Chapter 4**, which also discusses the beam dynamics simulations and a study of the thermal design of the gun. The analytical formulation devised by us to tune a photocathode gun structure is discussed in **Chapter 5**. This chapter also discusses the development of the final gun structures, and their low power RF characterization. Development of sub-systems like vacuum beam line components, emittance compensation solenoid, magnetic elements, beam diagnostics and development of high power RF conditioning setup are described in **Chapter 6**. A brief discussion on possible future work is given in **Chapter 7**.

List of Publications

Journal Articles

(Included in thesis)

[1] A new two-step tuning procedure for a photocathode gun

Shankar Lal, K. K. Pant, S. Krishnagopal, Nuclear Instruments and Methods in Physics Research, A592 (2008), 180-188.

[2] A novel scaling law relating the geometrical dimensions of a photocathode RF gun to its RF properties

Shankar Lal, K. K. Pant and S. Krishnagopal, Review of Scientific Instruments, **82**,123304 (2011).

[3] Brazing of photocathode RF gun structures in Hydrogen atmosphere: Process qualification, effect of brazing on RF properties and vacuum compatibility

Ajay Kak, P. K. Kulshreshtha, **Shankar Lal**, Rakesh Kaul, P Ganesh, K K Pant and Lala Abhinandan, Journal of Physics: Conference Series **390** (2012) 012025.

Conference Presentations /Publications

[1] Thermal Simulation of a Laser Photocathode rf gun,

B. Biswas, **Shankar Lal**, K. K. Pant, Arvind Kumar and S. Krishnagopal, in Proceedings of Asian Particle Accelerator Conference 2007, January 29-February 2, 2007, Indore, India, pp 482.

[2] Tuning of the waveguide to cavity coupling coefficient for a PWT linac and a photocathode gun,

S. Krishnagopal, **Shankar Lal**, K. K. Pant, Umesh Kale, in Proceedings of European Particle Accelerator Conference 2008, Genoa, Italy, 2008, pp.2734.

[3] Development of Brazing technique for a 1.6 cell BNL/SLAC/UCLA type phocathode guns by hydrogen brazing

Ajay Kak, P. K. Kulshreshtha, **Shankar Lal,** Proceedings of Indian Particle Accelerator Conference 2009, RRCAT, Indore, 2009.

[4] An analytical formulation for prediction of geometrical dimensions of a photocathode gun for desired RF properties,

Shankar Lal, K. K. Pant, BP&FEL Lab., MAASD, RRCAT, Indore, India, S. Krishnagopal, NPD, BARC, Mumbai, India, in Proceedings of International Particle Accelerator Conference 2010, Kyoto, Japan, pp. 3679-81**.**

[5] Brazing of Photocathode RF gun structures in Hydrogen atmosphere: Process qualification, Effect of brazing on RF properties, and Vacuum compatibility,

Ajay Kak, P. K. Kulshreshtha, **Shankar Lal**, Rakesh,Kaul, P. Ganesh, K. K. Pant and Lala Abhinandan, in Proceedings of the International Vacuum Symposium 2012, VECC, Kolkata.

List of Figures

List of Tables

CHAPTER 1

ELECTRON SOURCES: HISTORY AND OVERVIEW

INTRODUCTION

Electron accelerators have numerous applications, including high-energy linear colliders, short wavelength free electron lasers, wakefield accelerator experiments, drive beam for two-beam accelerators, Energy Recovery Linacs (ERLs), coherent radiation sources and radiochemistry *etc.*, that require high brightness electron sources [1, 2]. The development of such electron sources is in continuous progress starting from DC thermionic electrons guns to advanced photocathode RF guns to increase the brightness of electron beams. In this chapter we shall present a brief review of electron sources from DC thermionic guns to state of the art photocathode RF guns, and discuss their virtues and drawbacks.

1.1 DC ELECTRON SOURCE

1.1.1 Thermionic DC Electron Sources

The typical layout of a Thermionic DC electron source is shown in Fig.1.1. Electrons are emitted when a cathode is heated and get accelerated by the potential difference between anode and cathode. Although these sources are capable of producing high charge, up to few nCs, electrical breakdown at high DC voltage limits the maximum energy of electron beams to few 100’s of keV. The switching of high voltage pulses restrictes the bunch length to few ns, and for producing shorter bunches, bunching is necessary before injecting in the accelerator to boost the energy of electron beam, as shown in Fig.1.1. For example, the CLIO-FEL injector comprises a

90 keV thermionic electron source producing electron pulses of 1 ns duration. These are compressed by a factor of 12.5 by a sub-harmonic pre-buncher working at 500 MHz (1/6th of accelerator frequency of 3 GHz), and further compressed by another factor of 10 by a fundamental frequency buncher working at 3 GHz [3]. Similarly the Boeing Corporation injector uses two stages of bunching. The first stage is at 119 MHz which is the 24th sub-harmonic, and the second stage at 476 MHz, which is the 6th sub-harmonic, of the linac frequency of 2856 MHz [4].

Although thermionic DC electron sources are widely used for FEL and other accelerator applications, due to space charge effects at low energy and the presence of nonlinear RF fields in the bunching cavities, the emittance is of the order of 10-50 π mm-mrad and brightness is limited to ~10^{10} A/m^2 rad^2 [5].

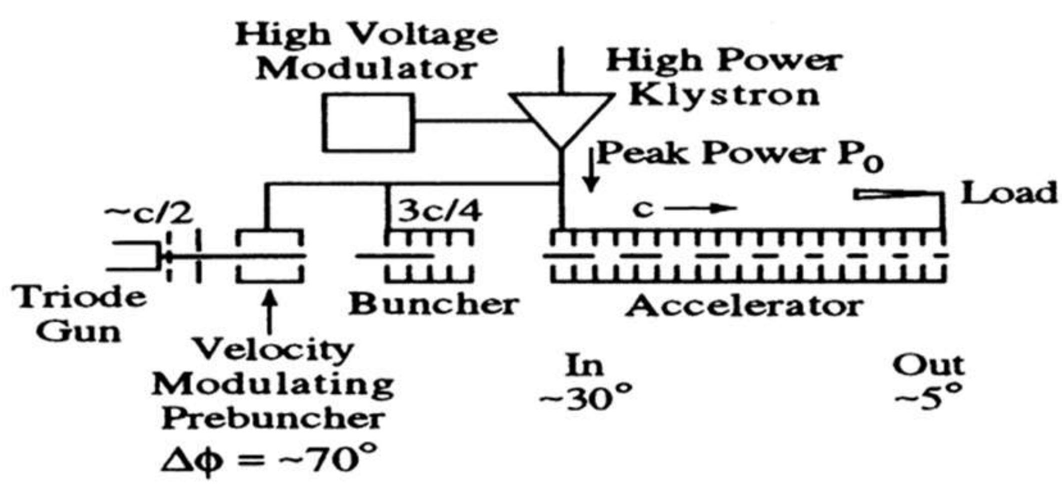

Fig.1.1: Typical layout of accelerator with DC thermionic electron source as an injector.

1.1.2 Photocathode DC Electron Sources

The limitation of the requirement of bunching sections in the case of DC thermionic electron sources was overcome by invention of photocathode DC electron guns. In these guns, electrons are produced through the photo-electric effect. When a laser pulse shines on a cathode electrons are born with temporal and special characteristics of the laser beam, and accelerated by a DC field applied between anode and cathode. Since lasers are available with pulse of few ps to few 10's of fs, bunching sections are not required in photocathode DC guns. However the energy of the electron beam is again limited to few 100's of keV due electric breakdown limit of DC fields, while the brightness of the electron beam is limited by the presence of space charge forces. Photocathode DC electron guns are mainly used to generate polarized electron beams required for high energy colliders [6].

1.2 RF ELECTRON SOURCES

As the electric breakdown limit of RF fields is much higher than the DC fields, in 1993 Madey and Westenskow proposed to put the cathode in an RF cavity and named this type of gun as 'RF Gun' [1]. Since an RF cavity can support accelerating gradients of the order of few 10's to 100's of MV/m, electrons are accelerated to relativistic energies within a very short distance, hence eliminating the problem of emittance growth due to space charge forces. As the bunch length of the electron beam from an RF gun is typically few 10s of degrees of the RF phase (for example for an S-band RF gun it is ~10 ps), this eliminates the requirement of any bunching system. Depending upon the type of electron generation process, RF electron sources are further classified as thermionic and photocathode RF sources as described below.

1.2.1 Thermionic RF Electron Source

The simplest design of a thermionic RF electron source is a pillbox cavity with a thermionic cathode being part of one end-wall and with a beam exit hole in the opposite end-wall. When the cathode is heated it continuously emits electrons and when they see the RF field in the cavity in the accelerating phase, electrons are accelerated and come out from beam exit port. With proper design, a large fraction of these electrons exit the cavity before the fields go into the decelerating phase. Those that do not exit the cavity are decelerated and turned around, and may return to impact the cathode (a phenomenon referred to as "back-bombardment") which limits the life of the cathode. As long as RF power is supplied to the gun, this cycle is repeated at every RF period, resulting in a train of bunches spaced at the RF period [7].

Although the electron beam pulse that actually comes out the cavity is very long typically a quarter of the RF period, and has very large energy spread, with an "α-magnet" and momentum filters RF thermionic guns are capable of producing very short beams with very low energy spread [1]. The injector of the Stanford Synchrotron Radiation Laboratory (SSRL) comprises a thermionic RF electron gun of two cells operating at 2856 MHz with an "α-magnet" and produces beam of 2-3 MeV, 0.3 nC with micro-pulse width of 2-5ps [7].

1.2.2 Laser driven RF Electron Source: Photocathode RF gun

When a photocathode placed in an RF accelerating cavity is illuminated by a short laser pulse, it can generate a very short electron beam with very high peak charge and low emittance. The electrons are rapidly accelerated to relativistic energies by high accelerating field (of the order of 100-200 MV/m) in the RF cavity, and hence emittance growth due to space charge is negligible. The great advantage of laser driven photocathode RF guns lies in the fact that the initial temporal and special distribution of the electron beam is governed by the laser beam parameters, and hence the electron beam parameters can be controlled by manipulating the laser beam parameters. As laser beams with very short pulse duration, of the order of few ps or even shorter, are commercially available, and this duration is typically less than the width of the phase-stable region for acceleration, hence photocathode RF guns are capable of generating bunched electron beams with very low energy spread and eliminate the requirement of bunching and momentum filters required in conventional electron sources [8, 9].

The first photocathode RF gun was proposed in 1985 by Fraser *et al.* and demonstrated experimentally in 1988, producing a 2.7 MeV electron beam with a normalized emittance of 40 π mm-mrad and peak charge of 15 nC in 22 ps [10, 11]. Thereafter, many laboratories around the world have been involved in developing and improving the capabilities of photocathode RF guns in order to achieve lower and lower emittance with higher and higher peak charge per pulse. A modified photocathode RF gun comprising 1.5 cells was proposed and developed at the Brookhaven National Laboratory (BNL), USA, in 1988 [12]. This was a side-coupled structure where RF was fed in both the half- and full-cells using a waveguide with two RF slots at a distance $\lambda/2$ apart (to suppress the zero mode), as shown in Fig. 1.2. The experimental as well as theoretical understanding of high brightness photo-injectors improved after Carlsten's invention of emittance compensation in 1989 [13-15].

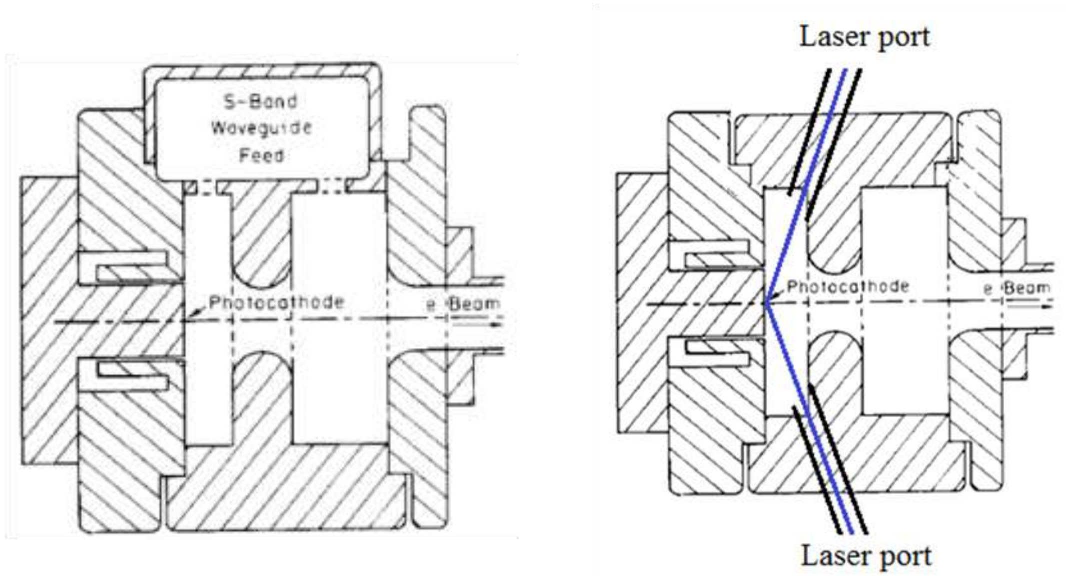

Fig. 1.2: BNL 1.5 cell side coupled zero mode suppressed photocathode RF gun.

The asymmetry introduced by RF ports in the half- and full-cells limits the minimum emittance achievable to 4π mm-mrad for 1 nC charge per micro pulse of 5 ps [16]. In the 1990's a SLAC, UCLA and BNL collaboration modified the design to an axi-symmetric structure by removing the RF port from the half-cell. In the new design RF power is fed only into the full-cell through an oblong slot on its outer wall and fields are setup in the half-cell through the inter-cell coupling iris, which is increased to 25 mm in diameter (from 20 mm in the 1.5 cell BNL design), to improve the coupling. In the new design asymmetry is removed by symmetrizing the RF coupling hole into the full-cell with a vacuum port of the same dimensions as the RF coupling slot and located exactly opposite it. Similarly, all other penetrations in both the cells are also symmetrized. This modified design is named the 1.6 cell BNL/SLAC/UCLA type photocathode RF gun and became a popular design for photocathode RF guns [17, 18]. We too have also designed and developed the 1.6 cell BNL/SLAC/UCLA type photocathode RF gun which is a standing wave, S-band structure resonating at 2856 MHz in the π-mode. The half-cell is 0.625

$\lambda/2$ long and comprises of two laser ports, while the full-cell is $\lambda/2$ long and has RF, vacuum and tuner ports. A single emittance compensation magnet is placed around the gun [19]. Beam dynamics simulations show that an emittance of < 2π mm-mrad can be obtained for an electron beam of 1 nC charge and 10 ps pulse length. The minimum achievable emittance of the beam is limited by the thermal and physical emittances.

1.3 BEAM PARAMETERS

Any charged particle (electron or ion) beam consists of many (>10^9) particles. Hence, it is important to understand the density distribution of the beam and its evolution in accelerating structures. In this Section we briefly specify the beam properties and their quality.

1.3.1 Phase Space and Emittance.

Each particle of the beam can be specified by six coordinates in phase space: three position and three momentum coordinates *(q_x, q_y, q_z, p_x, p_y, p_z)*. In accelerators the longitudinal component of momentum (p_z) is much larger than the transverse momentum component (p_x, p_y) and total energy of the particle is given by $E^2 = m_0^2c^4 + \left(p_x^2 + p_y^2 + p_z^2\right)^{1/2} \approx m_0^2c^4 + \left(p_z^2\right)^{1/2}$. Though the transverse momentum is small, it is not zero, and therefore the beam diverges, the slope of which is defined as $dx/dz = (dx/dt)/(dt/dz) = v_x/v_y = p_x/p_z$. Therefore, for particle beams, instead of the transverse momentum, it is more direct and convenient to measure the divergence [20]. At any given distance z along the direction of propagation of the beam, every particle represents a point in x-x′(and y-y′) space, known as *trace space*. The area occupied by the points that represent all the particles in the beam, in *trace space*, divided by π, is known as the *trace* or *geometrical* emittance. For a Gaussian beam distribution, the beam phase space contours in an accelerator are elliptical, as shown in Fig. 1.3. The lower the emittance the better the quality of the beam. The highest quality beams are laminar beams, for which emittance is zero. In accelerators where the beam is passed through accelerating as well as focusing elements, the *trace space* emittance does not describe the beam quality fully as it does not distinguish between a well behaved beam in a linear focusing system (occupying a regular elliptical/circular *trace space* area) and a beam with the same trace-space area but a distorted shape due to non-linear forces, as shown in Fig. 1.4. To eliminate this drawback of the trace space/geometrical emittance, Lapostolle and Sachere in 1997 introduced the concept of equivalent beam and RMS quantities of beam, such as radius and emittances [21, 22]. The concept of RMS equivalence states that two beams of the same particle species with same energy and current are equivalent, if the second moments of the distributions are same. This implies that RMS width and RMS emittance in two orthogonal directions (x, y) at some location z are identical for equivalent beams. Mathematically the RMS emittance is defined as

$$\varepsilon_{rms} = \sqrt{< x^2 >< x'^2 > - < xx' >^2}\,, \tag{1.1}$$

where

$$< x^2 > = \frac{\iint x^2 \rho(x, x', y, y') dx dx' dy dy'}{\iint \rho(x, x', y, y') dx dx' dy dy'}\,, \tag{1.2}$$

$$< x'^2 > = \frac{\iint x'^2 \rho(x, x', y, y') dx dx' dy dy'}{\iint \rho(x, x', y, y') dx dx' dy dy'}\,, \tag{1.3}$$

$$< xx' > = \frac{\iint xx' \rho(x, x', y, y') dx dx' dy dy'}{\iint \rho(x, x', y, y') dx dx' dy dy'} . \tag{1.4}$$

Similarly RMS emittance is also defined for the y direction. The RMS ellipse is defined by Courant-Snyder or Twiss parameters α_T, $\beta_{T,}$ γ_T and RMS emittance ε_{RMS} and is given by (Fig. 1.3),

$$\gamma_T x^2 + 2\alpha_T xx' + \beta_T x'^2 = \varepsilon , \tag{1.5}$$

$$\beta_T \gamma_T - \alpha_T^2 = 1 . \tag{1.6}$$

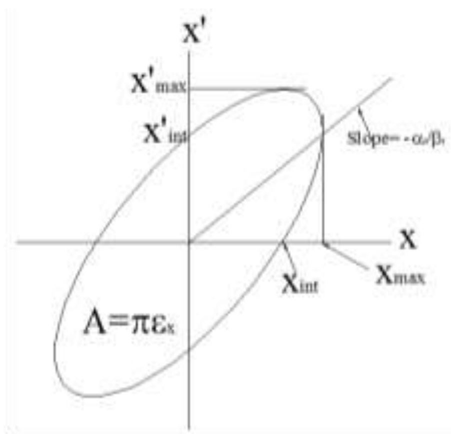

Fig.1.3: Trace space RMS ellipse. The maximum projections are $X_{max}=\sqrt{\varepsilon / \beta_T}$ and $X'_{max}=\sqrt{\varepsilon / \gamma_T}$, and the intercepts are $X_{int}=\sqrt{\varepsilon / \gamma_T}$ and $X'_{int}=\sqrt{\varepsilon / \beta_T}$.

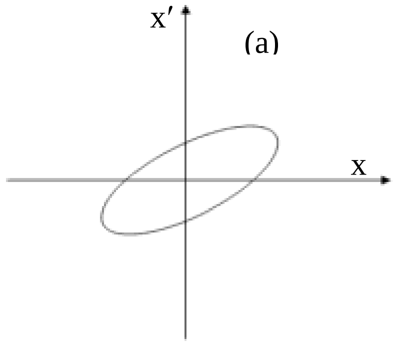

Fig. 1.4: Trace space of beam (a) under linear forces and (b) under non-linear forces.

During the acceleration process the longitudinal momentum of the particle beam increases while the transverse momentum is constant if non-linear forces are ignored and there is no particle loss. In this case the RMS emittance reduces with the energy of the beam while according to Liouville's theorem if a system of particles moves under conservative forces, the density of the particle distribution in phase space remain constant [23]. This is graphically represented in Fig. 1.5 in which the phase space of a collection of particles (beam) evolves with time from one configuration to another. Although the shape of the phase space changes, the density of phase space is constant if the applied force is conservative. Therefore it is more convenient to normalize the emittance by the momentum of the charged particle beam and define a *normalized emittance* which is constant during acceleration and transportation of the beam through linear and conservative forces. The normalized emittance is related to the trace emittance through

$$\varepsilon_{n,RMS} = \beta\gamma\varepsilon_{g,RMS} \,, \tag{1.7}$$

where $\beta = v/c$ is the normalized velocity of the particle and γ is the relativistic factor.

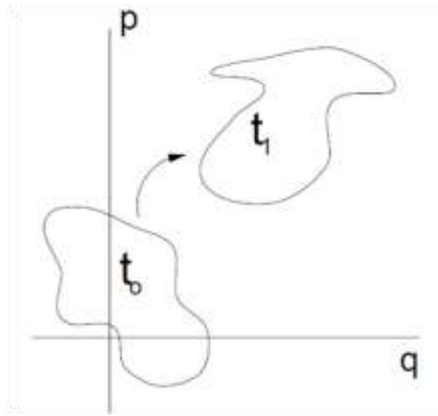

Fig.1.5: phase space density as function of time.

The normalized emittance $\varepsilon_{n,RMS}$ is the quantity that is invariant through the acceleration process, while $\varepsilon_{g,RMS}$ is the quantity revealed by experimental measurements. Here integration in Eqs. (1.1-1.4) are implicit over the whole longitudinal length of the beam. If the integrals are limited to a thin longitudinal slice of the beam between '*z'* and '*z*+*dz'*, then one defines a '*slice normalized*' emittance. For designing transport optics, the standard 2-D projected phase space area ("emittance") is generally adequate, while for Free-Electron Lasers (FELs) the electrons in particular phase space configuration contribute appreciably to the radiation field, motivating usage of the "slice emittance" [23, 24]. The different terms contributing to the emittance of a beam will be discussed in details in Chapter 3.

1.3.2 Brightness

The phase space density of the beam is called the *brightness* and is a very important figure of merit of the beam. It is defined as the peak current, I_P, divided by the transverse normalized emittance $\varepsilon_{nx,ny}$ [10],

$$B_n = \frac{2I_p}{\varepsilon_{nx}\varepsilon_{ny}}\,. \tag{1.8}$$

The definition of high quality beams is given in terms of high brightness, *i.e.* high current and low emittance. The relative importance of these figures of merit depends on the particular application of interest, and in many cases the physical processes are critically dependent on certain aspects such as emittance, current or energy spread. The brightness of an electron beam (or charged particle beam in general) can be increased by increasing the peak current and by reducing the transverse emittance of the beam. The peak current of beam can be increased by compressing the beam in time. The emittance can be minimized by controlling the emittance growth during generation, acceleration and transport of the beam by reducing the non-linear effects. An electron pulse with 100 A peak current and 1 π mm-mrad transverse emittance will results in brightness of the order of 10^{14} A/(m.rad)^2.

1.4 APPLICATIONS OF HIGH BRIGHTNESS BEAMS

The typical requirement of high brightness electron beams for accelerator applications like short wavelength Free-Electron Lasers (FELs) in the X-UV regime, wake-field accelerators and linear colliders are shown in Table 1.1 [26]. The output power of a free-electron laser and the luminosity of a linear collider are related to the brightness of the component beam [27-29]. The conventional electron sources are unable to satisfy the beam requirement of the above applications while the photocathode RF gun is a suitable device to generate high brightness electron beams with few ps bunch length, 1 nC charge and < 2π mm-mrad emittance.

Table 1.1: Typical electron beam requirements for various applications.

Application	**I(A)**	**ε_n (mm-mrad)**	**σ_t (ps)**	**Brightness (A/m^{2}rad^2)**
SASE FEL	200	2	6	9.10^{13}
Wake driver	1000	3	0.2	2.10^{14}
Linear collider	500	1 (y), 20 (x)	8	1.10^{13}
ERL	50	1	3	1.10^{14}

1.4.1 FEL Applications

The wavelength, power gain and operating conditions of the free-electron laser depend strongly on the electron beam parameters [30, 31]. The short wavelength FELs *i.e.* SASE FELs in the X-ray regime, impose stringent conditions on the electron beam pulse width in time, energy spread and peak current. The electron beam for an FEL should satisfy the following requirements:

- Electron beam emittance should be less than the natural emittance of the undulator radiation.
- The electron beam current should be high, in order to give as much charge per micro bunch as possible. The necessary beam current is derived from the desired gain length.
- The initial momentum / energy spread of the electron bunches should small enough to be within the bucket created by the FEL radiation field.

SUMMARY

The different types of electrons sources ranging from DC to laser driven photocathode RF guns have been reviewed. The axi-symmetric 1.6 cell BNL/SLAC/UCLA type photocathode RF gun is capable of producing an electron beam of few ps duration, with 1nC charge and emittance of less than 2π mm-mrad, required for many advanced accelerator applications.

We have designed and developed a 1.6 cell photocathode RF gun with emittance compensation solenoid and other beam transport elements. The remainder of this dissertation will discuss the RF design, beam dynamics simulations, fabrication, tuning, low level RF characterization and experimental studies with the photocathode RF gun developed by us.

CHAPTER 2

BASICS OF RF ACCELERATORS

INTRODUCTION

From the Lawson-Woodward theorem it follows that an electromagnetic wave cannot accelerate a charged particle if the field is in vacuum, without boundaries, and the region of interaction is infinite [32, 33]. One way to violate the conditions of the Lawson-Woodward theorem is to use guided structures that impose boundaries. Even in this case, if we want to accelerate a beam of charged particles moving in a certain direction, two conditions must be satisfied. Firstly, the electromagnetic wave must have an electric field component in the direction of particle motion, and, secondly, the wave and the particle must travel with same velocity or in other words the wave must be synchronized with the particle. The simplest guided structure is the uniform waveguide which supports the propagation of waves that have a longitudinal component of the electric field, and can hence satisfy the first condition. The second condition, however, cannot be fulfilled by a wave propagating in a uniform waveguide as the phase velocity of the wave is higher than the velocity of light, while the particle velocity is always less than velocity of light. The solution is to slow down the wave velocity in the waveguide to match with the velocity of the charged particle. Classically, the velocity of any object can be reduced by putting an obstacle or perturbation in its path and can be manipulated to the desired value by putting obstacles repeatedly. Using the same analogy it is also possible to slow down the wave velocity by introducing periodic perturbations in the uniform waveguide. The reduction in wave velocity depends upon the perturbations and by employing a suitable design of perturbations the wave velocity can be matched with the particle velocity. Therefore a waveguide with periodic perturbations along the length can be used to accelerate a charged particle. Looking rigorously the velocity of the wave reduces due to its reflection from each perturbation. The reflected part of the wave travels in the opposite direction and again gets reflected from the previous perturbation and this way the wave starts oscillating between two consecutive perturbations, the pair of them therefore acting like a resonating cavity. Since the perturbations are periodic in nature the whole structure can be described as an array of coupled cavities. As the photocathode RF gun is also a coupled cavity structure, the understanding of cavity basics and behaviour of an array of coupled cavities is important in the development of a photocathode RF gun. Therefore the basics of an RF cavity and coupled cavity structure are discussed in detail in this chapter before move towards the design of a photocathode RF gun.

2.1 PILLBOX CAVITY BASICS

The simplest resonating structure can be formed by shorting the ends of a uniform waveguide with conducting plates, thus forming a uniform cylindrical cavity or a pillbox cavity, which serves as fundamental building block in accelerating structures. The boundary conditions imposed at the cavity walls (transverse as well as longitudinal) allow only certain discrete field patterns known as cavity modes (sometimes electromagnetic modes of the cavity) and can be derived by solving Maxwell's equations. They can be divided in two categories based on the characteristics satisfied by the longitudinal component of the electric or magnetic field: (1) Transverse Magnetic (TM) for those with $B_z = 0$ everywhere in the structure and (2) Transverse Electric (TE) for those with $E_z = 0$ everywhere in the structure. To describe any particular mode three indices are necessary and modes are specified by TM_{mnp} or TE_{mnp}. Here subscript ‘m’ (m=0,1,2,…) is the number of full period variation of field in Φ direction, ‘n’(n=1,2,3…) is the number of zeros of the axial field component in the radial direction in the range $0 < r \leq R_c$ (radius of cavity), excluding r = 0 and ‘p’(p = 0,1,2…) is the number of half –period variations of the field along the z-axis [34, 35]. As the TE modes, by definition, have no electric field in the ‘z’ direction they are not suited for acceleration in this geometry, while TM modes have non-zero E_z components and hence can be used for acceleration. The resonant frequencies for the TM_{mnp} modes in a pillbox of radius R_c and length L are given by

$$f_{mnp} = \frac{1}{2\pi\sqrt{\mu\varepsilon}} \sqrt{\left(\frac{\chi_{mn}}{R_c}\right)^2 + \left(\frac{p\pi}{L}\right)^2}, \tag{2.1}$$

where ε and μ are the permittivity and permeability of the medium inside the cavity and χ_{mn} is the n^{th} root of the m^{th} order Bessel function with $J_m(\chi_{mn}) = 0$. The lowest TM mode is TM_{010} which has an electric field parallel to the z-axis while the magnetic field circles around it. The field patterns are rotationally symmetric and have no *z* dependence as shown in Fig. 2.1. Furthermore, the resonant frequency is independent of the length of the pillbox. This mode is used in almost all electric field (E-type) accelerators. Its resonant frequency and fields are given by:

$$f_{010} = \frac{\chi_{01}}{2\pi\sqrt{\mu\varepsilon}R_c}, \tag{2.2}$$

$$\chi_{01} = 2.405, \tag{2.3}$$

$$E_z(r,t) = E_0 J_0\left(\frac{\chi_{01} r}{R_c}\right) e^{j\omega t}, \tag{2.4}$$

$$B_\phi(r,t) = -j\sqrt{\frac{\varepsilon}{\mu}} E_0 J_1\left(\frac{\chi_{01} r}{R_c}\right) e^{j\omega t}, \tag{2.5}$$

where E_0 is the peak electric field, J_0 and J_1 are the 0th and 1st order Bessel function and $\omega=2\pi f$. Since the resonant frequency of the TM_{010} mode is independent of the cavity length, this length can be tuned for optimum acceleration. For a charge entering a pillbox cavity with speed v, the length for maximum energy gain is $\pi L/\beta\lambda$, where $\beta=v/c$ [34].

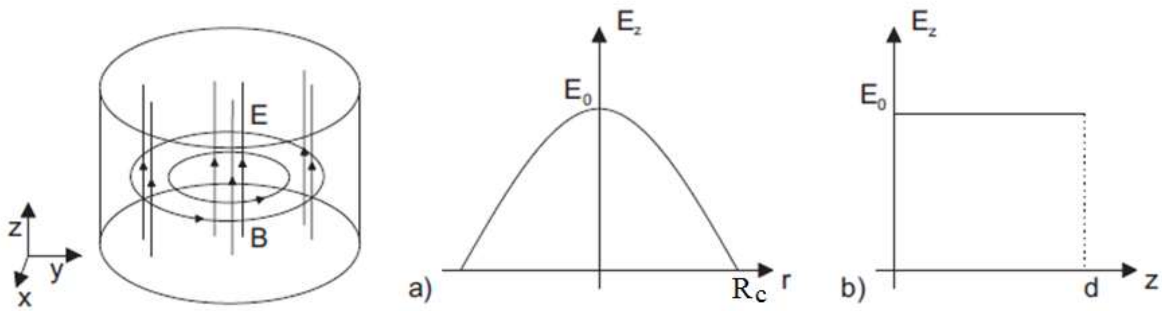

Fig. 2.1: Pillbox cavity with an electromagnetic field in the TM_{010} mode. The graphs show the amplitude of E_z as function of (a) radius and (b) length of pillbox.

To accelerate a charged particle, the pillbox cavity needs to be modified by providing ports for entry and exit of the beam. The modified geometry of the pillbox cavity with entry and exit ports is shown in Fig. 2.2. In this modified geometry E_z should be zero at the locations of ports to satisfy the boundary condition as shown in Fig. 2.2, and the modified field is given by

$$E_z(r,t) = E_0 J_0\left(\frac{\chi_{01} r}{R_c}\right) Cos\left(K_z z\right) e^{j\omega t}, \tag{2.6}$$

where constant $K_z = (2N+1)\pi / L_{eff}$ and L_{eff} is effective length of the cavity, which is the accelerating gap plus length of ports up to which the field is non-zero [34].

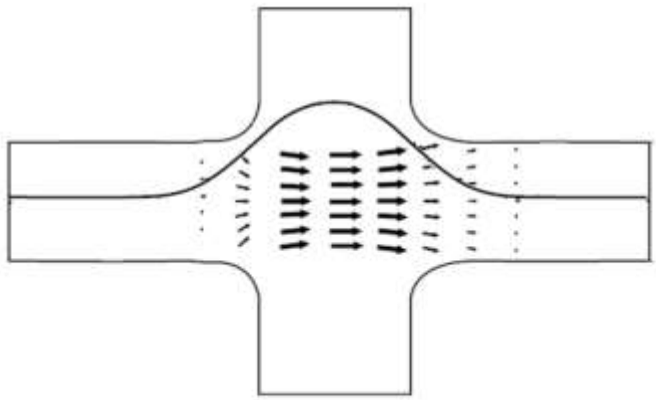

Fig. 2.2: Pill box cavity with the ports for beam entry and exit, and variation in E_z with z.

As the electromagnetic fields are oscillating with time, when a charged particle passes through the cavity it see a time-varying electric field and the energy gained by the particle, ignoring the effect of the ports, is given by [34]

$$\Delta W = qV = q \int_{-L/2}^{L/2} E_z(z,t) e^{j\omega z/c} dz \, , \tag{2.6}$$

$$\Delta W = qE_0 TL \cos(\phi_0), \tag{2.7}$$

where $0<T\leq 1$ is the *transit time factor* defined as the ratio of energy gained in the time varying field to the that gained in a DC field of the same peak value. The maximum attainable field in any resonant structure is ultimately limited by electrical breakdown [35].

2.2 COUPLED PILLBOX STRUCTURE OR COUPLED CAVITY STRUCTURE: SPACE HARMONICS

In the case of a pillbox cavity the maximum on-axis field, for pulses of few μs duration, is typically ~100 MV/m for the S-band frequency, which gives a maximum energy gain of ~3-4 MeV; therefore for higher energies more than one pillbox cavity is required. Having several independent pillbox cavities requires independent RF feeds which is expensive, and the requirement of synchronization between them further complicates the system and adds to the expense. The alternate option is to connect the multiple pillbox cavities such that the fields in individual cavities can be coupled. This type of structure gives high average field gradients and is known as a *coupled cavity* structure. In principle when RF power is fed into one cavity (normally called the coupling cell) it is transferred to the other cavities also and sets up an electromagnetic field in all of them. The coupling of RF power between two cavities (or cells) is known as inter-cell coupling. When power is coupled by making off-axis slots in the disc separating two pillbox cavities, it is mainly the magnetic field that is coupled and this is known as *B-type coupling*, while when power is coupled by on-axis apertures it is mainly the electric field that is coupled and this is known as *E-type coupling*. The presence of off-axis slots in B-type coupling breaks the rotational symmetry of the cavity which scatters the electromagnetic energy into higher-order harmonics which spoils the transverse emittance of the beam; hence magnetic coupling is not preferred where lower emittance is needed like in photocathode RF guns. On the other hand, in E-type coupling rotational symmetry is maintained, and it is therefore used exclusively in high brightness photocathode RF guns.

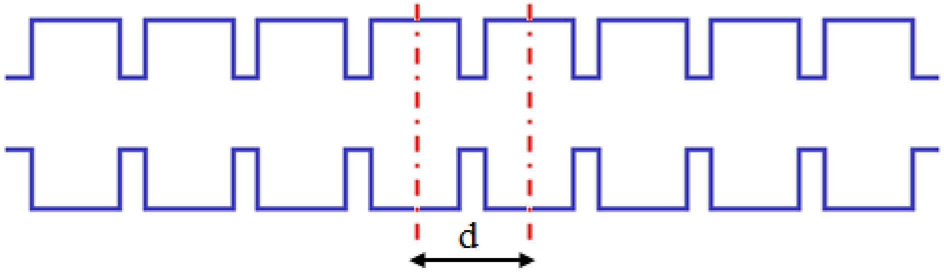

Fig. 2.3: The schematic of coupled cavity structure.

An E-coupled cavity accelerating structure is shown in Fig. 2.3. It is a periodic structure with periodicity 'd' and according to the Floquet theorem it supports an infinite number of traveling waves having the same frequency but different wave numbers called *space harmonics* [37]. The space harmonics have a constant amplitude of the electric field E_n independent of *z*. The wave number of the n^{th} space harmonic is given by

$$k_n = k_0 + \frac{2\pi n}{d}, n = -\infty...0..+\infty, \tag{2.8}$$

and the electric field (for TM_{010} like mode) can be expanded in a Fourier series of different space harmonic as

$$E_z^{\pm}(r, z, t) = \sum_{-\infty}^{+\infty} E_n^{\pm} e^{j(\omega t + k_n z)}. \tag{2.9}$$

The waves with index n ≥ 0 travel in the +*z* direction and are known as *forward waves*, denoted by E_z^+, while the waves with n < 0 travel in the –*z* direction and are known as *backward waves*, denoted by E_z^-. The phase velocity of the n^{th} space harmonics is given by

$$v_{ph}^n = \frac{\omega}{k_n} = \frac{c}{1 + \frac{2\pi n}{k_0 d}} = \frac{c}{1 + \frac{n\lambda}{d}} \ . \tag{2.10}$$

As discussed earlier for acceleration the phase velocity of the wave must be equal to the particle velocity and such a wave is known as a synchronous wave. From Eq. (2.10), it is clear that space harmonics with $n < 0$ have phase velocity > c and are hence not suitable for acceleration. The space harmonics with $n \geq 0$, have phase velocity ≤ c and can hence be used for acceleration. As different space harmonics have different phase velocities only one, usually the fundamental ($n = 0$) harmonic, is synchronous with the particle and contributes to the energy gain. The effects of the non-synchronous space harmonics on the particle average to zero (in some cells they accelerate while in some cells they decelerate and so the net energy gain is zero) and do not contribute to energy gain at the end of the structure.

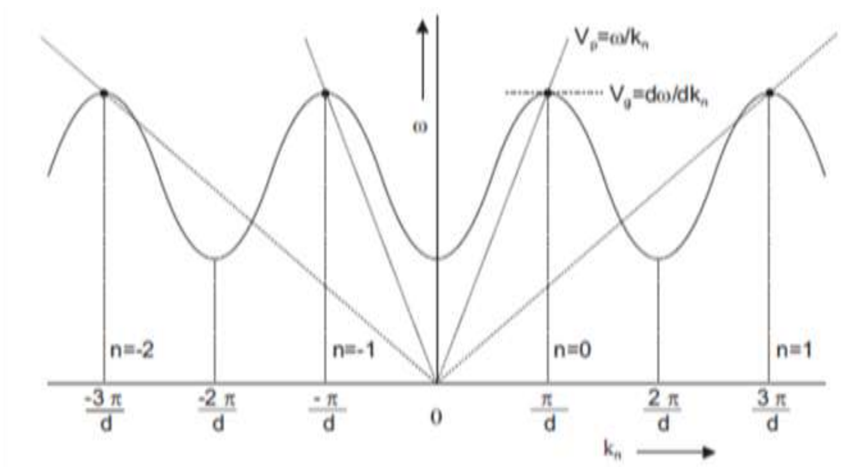

Fig.2.4: Dispersion curve of the lowest pass band of an infinite periodic structure.

2.2.1 Coupled Cavity Structure : Normal Modes

In a coupled cavity structure, for each electromagnetic mode of the individual cavity, there is a family of modes that have their own frequencies different from the resonant frequency of a single cavity, and with a characteristic phase advance from one cavity to next cavity. These are known as *normal modes*. For an infinite string of coupled cavities, each space harmonic has associated with it an infinite number of normal modes within a certain frequency band, known as the *pass-band,* and those are the only waves that can propagate in the structure. Figure 2.4 shows the lowest pass-band corresponding to the TM_{010} mode of a single cavity. For n = 0, space harmonics normal modes correspond to a phase advance per cavity $0 < k_z d < \pi$, and having frequency from f_0 to f_π. Practically, a structure is made by a coupling finite number of cavities and such a structure supports a finite number of discrete normal modes. An accelerating structure made of *N* coupled cavities, supports *N* normal modes with phase shift per cavity given by

$$\phi_q = \frac{q\pi}{N-1}, \ q = 0,1,2...N \ . \tag{2.11}$$

For an example if an accelerator is composed of two coupled cavities ($N = 2$) then it supports two normal modes with phase shifts of $\phi_q = 0$ and π with resonant frequencies f_0, f_π, and if an accelerator composed of four coupled cavities ($N = 4$) then it supports four normal modes with phase shifts of $\phi_q = 0$, $\pi/3$, $2\pi/3$ and π with resonant frequencies of f_0, $f_{\pi/3}$, $f_{2\pi/3}$, f_π. Each normal mode has a unique phase velocity which depends upon the individual cavity length (or more specifically it depends upon the separation between two cavities) and strength of inter-cell coupling. Therefore, for efficient acceleration, the structure has to be designed considering a particular normal mode as the synchronous mode. The mode-separation or frequency difference between different normal modes is also an important design parameter because if the modes are not well separated, then a small perturbation in the structure (due to RF heating or beam loading or any other reason) may switch the mode of operation, and in such a case when RF power is coupled to the structure to excite the synchronous normal mode, it may excite a non-synchronous mode, which does not accelerate the beam. Therefore while designing a coupled cavity accelerating structure mode separation should be kept sufficiently high or greater than the bandwidth of the RF source being used to excite the structure to prevent undesired mode switching.

2.3 RF ACCELERATING STRUCTURE FIGURES OF MERIT

The RF parameters of an accelerating structure play an important role in the acceleration of the beam and affect the beam parameters. Therefore it is important to define and understand the RF parameters of an accelerating structure. Description of some of the important and crucial RF parameters is given below.

2.3.1 Quality Factor

The *quality factor*, Q_0 of an accelerating structure is a measure of the energy stored in the structure for unit power dissipation and is defined as the ratio of the time averaged stored energy U in the structure to the power dissipated per radian of the RF cycle,

$$Q_0 = \omega_0 \frac{U}{P_c}, \tag{2.12}$$

where ω_0 is the angular frequency of the RF wave and P_c is the power dissipated in the structure. For a practical accelerating structure, the field decays with time due to power dissipation in the walls of the structure, and to maintain the field gradient RF power needs to be fed into the structure. In this configuration the quality factor of the cavity is different from Q_0 due to reflections at the entrance to the accelerating structure. One therefore defines the *loaded quality factor* Q_L,

$$Q_L = \frac{Q_0}{(1+\beta)}, \tag{2.13}$$

where β is the coupling coefficient of the structure to the RF transmission line, as defined later, in section 2.3.5.

2.3.2 Shunt Impedance

The *shunt impedance* of an accelerator structure is a figure of merit measuring the energy transfer efficiency from the RF field to the charged particles. For an axial electric field $E_z(z)$ over the structure length L, the shunt impedance, R_{sh} per unit length is defined as,

$$R_{sh} = \frac{\frac{1}{L}\left[\int_0^L E_z(z)dz\right]^2}{dP_c / dz}, \tag{2.14}$$

where dP_c/dz is the power dissipation per unit length of the structure. High shunt impedance is desirable since it means high accelerating field for a given power dissipation per unit length of the structure.

2.3.3 Transit Time Factor

The energy gained by a charged particle in a time varying accelerating field is less than that from a corresponding static field because the particle takes some time to cross the accelerating structure and it consequently sees an average field which is always less than the peak value. The ratio between these energies is known as the *transit time factor*, and is defined by,

$$T = \frac{\left|\int E_z(z)e^{ikz}dz\right|}{\int E_z(z)dz}, \tag{2.15}$$

where $k=\omega/c$ is the propagation constant. For a pillbox cavity with beam ports, as shown in Fig. 2.2, the transit time factor for a particle with velocity β (and assuming that this does not change during the acceleration process) is given by [34]

$$T = \frac{Sin\left(\frac{\pi L_{gap}}{\beta\lambda}\right)}{\left(\frac{\pi L_{gap}}{\beta\lambda}\right)} \ , \tag{2.16}$$

where L_{gap} is the length of accelerating gap (total length of cavity minus length of ports). Although from above equation it is clear that to maximize T the accelerating gap should be minimum, for a given accelerating gradient the total energy gain in the cavity reduces with accelerating gap as given in equation (2.7). Therefore, in-spite of the transit time factor the length should be optimized for energy gain, which is maximum for cavity length of $\beta\lambda/2$ [34].

Sometimes it is preferred to include the transit time factor in the calculation of the shunt impedance. Then, one defines an *effective shut impedance* $R = R_{sh}T^2$. For higher efficiency of the accelerator, the effective shunt impedance should be higher.

2.3.4 Characteristic Impedance

The *characteristic impedance*, R/Q_0 is a geometry dependent parameter and measures the efficiency of acceleration per unit stored energy at a given frequency. It is given by

$$R/Q_0 = \frac{\left[\int E_z(z)dz\right]^2}{\omega_0 W}. \tag{2.17}$$

2.3.5 Waveguide to Cavity Coupling Coefficient (β)

To power the accelerating structure RF power is transported from the RF source to the accelerating structure using a transmission line (for high frequencies this is usually a waveguide) and is coupled into the cavity by using a loop or through a small coupling slot located on its outer wall. The efficiency of RF power coupling to the structure is determined by the waveguide to cavity coupling coefficient (β) which is defined as

$$\beta = \frac{P_{ext}}{P_c} = \frac{Q_0}{Q_{ext}}, \tag{2.18}$$

where P_c is the power dissipated inside the cavity and P_{ext} is the power lost outside of the cavity, or, more precisely, in the matched load of the waveguide when RF source is turned off [38]. The amount of RF power coupled to the cavity is given by

$$P_c = \frac{4\beta}{(1+\beta)^2} P_+, \tag{2.19}$$

where P_+ is the input RF power. When β=1 the power transferred to the cavity is maximum.

2.3.6 Filling Time

When RF power is fed into an accelerating structure, part of the RF power dissipates in the structure and part of it goes towards setting up the electromagnetic field in the cavity. The *filling time* of a standing wave RF cavity is the time needed to build the electromagnetic field in the structure up to *(1-1/e)=0.632* times its steady-state value, and mathematically can be written as,

$$t_f = \frac{2Q_L}{\omega_0} = \frac{2Q_0}{(1+\beta)\omega_0} \quad . \tag{2.20}$$

For a traveling wave structure, the electromagnetic field travels along the length of the structure and is dumped at the end in a matched load. In this case the filling time is defined as

$$t_f = \frac{L}{v_g} \, . \tag{2.21}$$

where L is the total length of the structure and v_g is the group velocity of the traveling wave in the structure.

To achieve the maximum and uniform energy gain the beam is injected into the structure after a few filling times for a standing wave and for one filling time for a traveling wave linac. Cavities with large quality factor take longer to be filled with energy; for example, in super-conducting cavities which have Q_0 of the order of 10^{10} the fill time is of the order of *ms* to *s* while for normal conducting structures with Q_0 of the order of 10^4, the fill time is of the order of few hundreds of ns to few μs.

2.4 LOW POWER RF CHARACTERIZATION THEORY AND MEASUREMENTS

An RF accelerating structure is characterized by its RF properties, *viz.* resonant frequency, quality factor, shunt impedance, characteristic impedance, variation in on-axis accelerating field, waveguide to cavity coupling coefficient and fill time, as discussed in the earlier section. Therefore it is important to understand the methods used to measure the RF properties of an RF accelerating structure. In this section, we discuss the theory and methods to measure the RF properties of an RF accelerating structure at low power, which are also known as *cold test* measurements.

2.4.1 RF Measurement Theory

For DC applications a network can be characterized completely by measuring the voltage and current; however it is not possible to measure the voltage and current at high frequencies as they vary rapidly in time and space and such fast detectors are not typically available. Also, the measurement of voltage and current at two different times at same position or at two different positions at same time, gives different results. Therefore, at high frequencies measurement of the reflected and transmitted waves with respect to the incident wave is employed to characterize a network. When a RF signal is fed to a network a fraction of it reflected back, a fraction is transmitted and the remaining gets dissipated in the network. As the energy of the incident wave is scattered into reflected and transmitted waves the ratios of the reflected and transmitted waves to the incident wave are known as *scattering parameters* or *S-parameters* and are the basics building blocks for RF measurements. If a network has more than one port then the signal at any port is represented as a linear combination of the reflected and transmitted signals due to different ports. For example, for a two-port network, when RF power is fed at port 1 and port 2 is matched, then the ratio of the reflected wave to the input wave at port 1 is defined as $S_{11}=V^-_1/V^+_1$ where V^-_1 is the reflected wave and V^+_1 is the incident wave at port 1, and the ratio of RF signal at port 2 (V^+_2) when the input port is matched is defined as $S_{21}=V^+_2/V^+_1$. Similarly when the RF signal is fed at port 2 two more S parameters, S_{22} and S_{12} are defined. Now, the signal at port 1 is represented as $V_1^- = S_{11}V_1^+ + S_{12}V_2^+$ and the signal at port 2 is given by $V_2^- = S_{21}V_1^+ + S_{22}V_2^+$. From the above it is clear that a network can be represented completely by a matrix of S parameters which is known as the *scattering matrix* [39, 40]. For an 'n' port RF device the scattering matrix is given by

$$\begin{bmatrix} V_1^- \\ V_2^- \\ \vdots \\ V_n^- \end{bmatrix} = \begin{bmatrix} S_{11} & S_{12} & .. & S_{1n} \\ S_{21} & & & S_{2n} \\ \vdots & & & \vdots \\ S_{n1} & S_{n2} & .. & S_{nn} \end{bmatrix} \begin{bmatrix} V_1^+ \\ V_2^+ \\ \vdots \\ V_n^+ \end{bmatrix}, \tag{2.22}$$

where the ij^{th} element of the S matrix is defined as

$$S_{ij} = \left. \frac{V_i^-}{V_j^+} \right|_{V_k^+ = 0 \text{ for } k \neq j}, \tag{2.23}$$

V_j^+ is the amplitude of the incident wave at port j and V_i^- is the amplitude of the reflected wave coming out from port i. The S parameters of an RF device can be measured by using a multiport Vector Network Analyzer (VNA). [41].

An RF accelerating structure with an RF coupling port can be considered as two port device and by measuring S_{11} and/or S_{21}, RF parameters of the accelerating structure can be determined [17]. The determination of RF parameters using S_{11} measurement is known as the reflection method while measurement using S_{21} is known as the transmission method. The methods of measuring the different RF parameters are discussed below.

2.4.2 Resonant Frequency Measurement

As an RF accelerating structure acts like an oscillator, at resonance the energy stored in it is maximum and reflection is minimum [34]. Therefore, the resonant frequency of an RF accelerating structure can be determined by measuring S_{11} while varying the frequency of the input signal. As the energy stored in the structure is maximum at resonance the resonance frequency can also be measured by measuring the S_{21} which gives the strength of the field in the cavity as a function of frequency. A typical plot of S_{11} and S_{21} with frequency measured by using a VNA is shown in Fig.2.5.

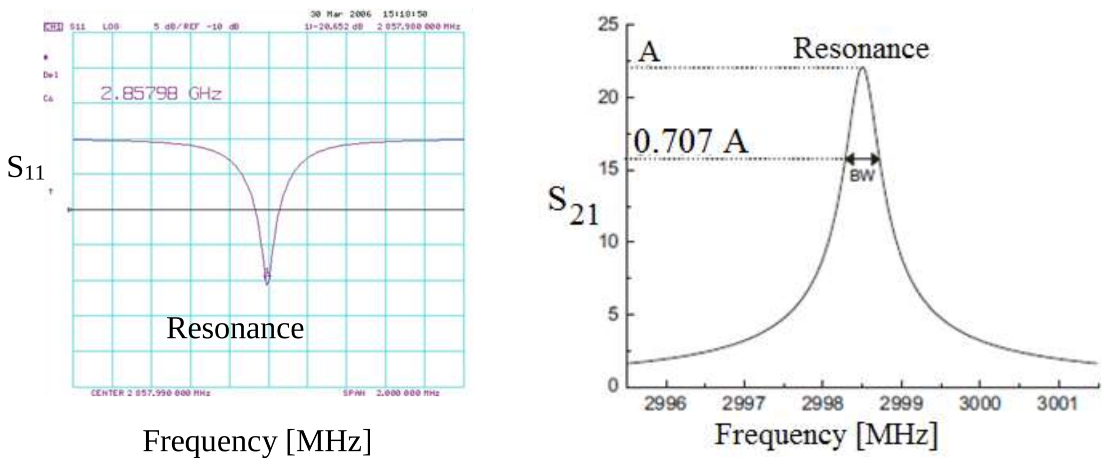

Fig.2.5: Variation of S_{11} and S_{21} of an accelerating structure, with frequency.

2.4.3 Quality Factor and Waveguide to Cavity Coupling Coefficient Measurement

2.4.3.1 Transmission and VSWR Technique

The quality factor can be calculated by measuring the -3dB down points (half power points) on the S_{21} graph and is given by,

$$Q_0 = \frac{f_r}{|f_2 - f_1|}, \tag{2.24}$$

where f_1 and f_2 are the frequencies of the -3dB down power points with respect to the resonant frequency (f_r). The measurement of Q_0 employing above the technique gives wrong results as loss in coupling port also contributes in the measurement. So, instead Q_0 it is the loaded quality factor Q_L that is actually measured [39].

The waveguide to cavity coupling coefficient is directly related to the Voltage Standing Wave Ratio (VSWR) which is directly measurably in modern VNA's [17, 39], and is given by

$$\beta = \begin{cases} VSWR, \text{ if over coupled} \\ \dfrac{1}{VSWR}, \text{ if under coupled} \end{cases} . \tag{2.25}$$

Clearly, the value of β will be wrong if we do not know whether the cavity is over coupled or under coupled.

2.4.3.2 Smith Chart Technique

Smith Chart is a representation of the normalized impedances (or admittances) on the reflection plane [42]. In a Smith Chart the reflection coefficient is converted in terms of constant resistance and reactance circles, and impedance of a device or network at a particular frequency is represented by a single point, and for a frequency band it represents the loci of the impedances.

The Smith Chart gives the direct measurement of the quality factor and waveguide to cavity coupling coefficient [39].The quality factors given by

$$Q_0 = \frac{f_r}{|f_2 - f_1|}, \tag{2.26}$$

$$Q_{ext} = \frac{f_r}{|f_4 - f_3|}, \tag{2.27}$$

$$Q_L = \frac{f_r}{|f_6 - f_5|}, \tag{2.28}$$

where f_r and $f_{1\text{-}6}$ are the frequencies determined from the intersection, on the normalized Sith Chart, of impedance $z = r + jx$ loci Chart and x lines, as described below. f_r is the resonant frequency of the RF accelerating structure and can be determined from intersection of S_{11} circle and the $x = 0$ line. Similarly f_1 and f_2 are the frequencies determined from the intersection of the S_{11} circle (or Smith Chart) and $x = \pm r$ line, f_3 and f_4 are frequencies determined from the intersection of the S_{11} and the $x = \pm 1$ line, and f_5 and f_6 are frequencies determined from the intersection of the S_{11} and the $x = \pm (r \pm 1)$ line.

A typical Smith Chart for an RF cavity and waveguide coupled system is shown in Fig 2.6.

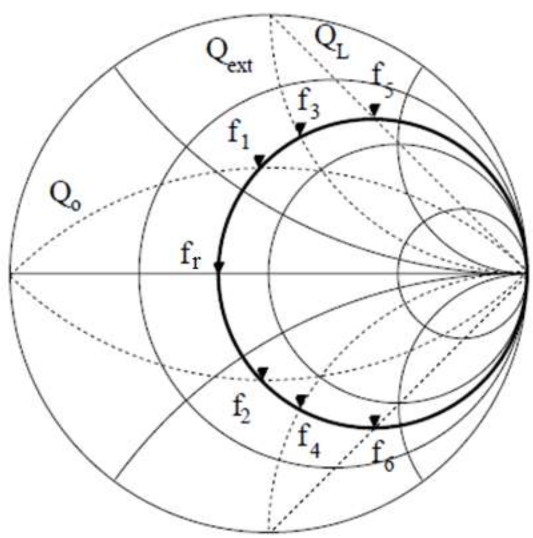

Fig. 2.6: Smith Chart of and RF cavity waveguide coupled system.

After determining the different frequencies form a Smith Chart the quality factors can be measured directly by using Eqs. (2.26-2.28) while β can be calculated using Eq. (2.18).

2.4.4 Shunt Impedance and Characteristic Impedance Measurement

From Eqs. (2.14) and (2.16) it is clear that the shunt impedance and characteristic impedance of an RF accelerating structure can be determined when the variation in the on-axis accelerating field (E_z) is known. The variation in E_z can be determined by employing the *bead pull* technique as discussed below.

2.4.4.1 Bead Pull Technique

In an RF cavity at resonance, both the magnetic and electric field energies are equal, and any perturbation in the field distribution changes the resonant frequency of the structure. This change depends upon the strength of the field at the location of the perturbation. Therefore, by measuring the variation in the resonant frequency the electromagnetic field can be determined using the Slater perturbation theory [43], according to which the frequency shift in the resonant frequency, ω_0 due to perturbation of the cavity field is given by

$$\frac{\omega^2-\omega_0^2}{\omega_0^2}=\frac{\int_{\delta\tau}\left[H_\alpha^2-E_\alpha^2\right]d\tau}{\int_{\delta v}\left[\mu_0 H^2+\varepsilon_0 E^2\right]dv}. \tag{2.29}$$

Here, μ_0 and ε_0 are the permeability and permittivity of free space, respectively. $\mathbf{H}_\alpha$ and $\mathbf{E}_\alpha$ are the perturbed magnetic and electric field vectors at the location of the perturbing object of volume $\delta\tau$. The amplitude of the perturbed fields depends on the bead's volume, shape, composition and location. **H** and **E** are the magnetic and electric field strengths in the unperturbed cavity of volume *dv*.

Therefore, by pulling a small perturbing object (know as bead) through the cavity, the distribution or profile of the electromagnetic field can be measured and this technique is known as the *bead pull technique* [44].

For the TM_{010} mode, $\mathbf{H}_{\alpha}=0$ on the axis of the structure, and the denominator of Eq. (2.29) represents the total energy stored in the structure, which is constant. Then, the electric field at each location of the bead is proportional to the frequency shift as

$$E_z(z) \propto \sqrt{\omega_0 - \omega(z)}\ , \tag{2.30}$$

where ω(z) is the resonant frequency of the RF cavity when the bead is at location *z*. Using E_z in Eq. (2.17) the characteristic impedance of the structure is given by,

$$\frac{R}{Q_0} = \frac{1}{2\pi f_0^2 \Im_z^e}\left[\int_L \left\{\sqrt{(f_0(z=0) - f(z=z)}\right\} dz\right]^2 , \tag{2.31}$$

where $\Im^e$ depends upon the shape and size of the bead and is known as the *form factor* [45]. Once R/Q_0 is known the shunt impedance of the structure can be calculated by using the measured value of Q_0 in $R = (R/Q_0) \times Q_0$.

SUMMARY

The building block of an accelerating structure is a pillbox cavity operating in the TM_{010} like mode and a complete accelerating structure is formed when many such cavities are connected together. The basics of a pillbox cavity along with coupled cavity structures and concept of electromagnetic and structure modes have been discussed. The figures of merit of an accelerating structure and techniques to measure them have also been discussed in detail.

CHAPTER 3

PHOTOCATHODE RF GUN THEORY

INTRODUCTION

Understanding the evolution of the electron beam in a photocathode RF gun is very important for the production of a high quality beam. To accomplish this we shall lay the ground work for a theoretical understanding of beam quantities: concept of emittance, beam brightness and emittance compensation techniques. This is followed by approximate scaling laws for different beam parameters based upon an analytical study of the equations for acceleration of beam in a photocathode RF gun. Experimental and technological issues play an important role in the choice of practical values for the different parameters of the gun, and hence some of these issues are also discussed in this chapter.

3.1 EMITTANCE TERMS

The emittance of the electron beam from a photo-injector is influenced by many factors *viz.* space-charge force, RF field used for acceleration, higher-order modes in the accelerating cavity, magnetic field used for emittance compensation, energy difference between drive laser and work function of the cathode material and the physical temperature of the cathode material [17]. Therefore, the total emittance of the electron beam from a photo-injector is given by

$$\varepsilon_{n,RMS} = \sqrt{\varepsilon_T^2 + \varepsilon_0^2 + \varepsilon_{sc}^2 + \varepsilon_{RF}^2 + \varepsilon_{Bz}^2 + \varepsilon_{fa}^2} \quad . \tag{3.1}$$

The physical significance and the upper and lower limits of different emittance terms are discussed in following sections.

3.1.1 Physical Temperature Emittance ε_T

The physical temperature of the cathode during operation increases the kinetic energy of the photo-electrons by $k_B T/2$, which introduces a velocity distribution in the electrons. The transverse component of the velocity increases the emittance of beam and is known as the *physical temperature emittance*, given by

$$\varepsilon_T = \frac{R_0}{2}\sqrt{\frac{k_B T}{m_0 c^2}} \ , \tag{3.2}$$

where k_B is the Boltzmann's constant and T is the temperature of the photocathode in degree Kelvin. For a typical operating temperature of 50^0 C the physical temperature emittance is ~ 0.12 π mm-mrad.

3.1.2 Thermal Emittance ε_0

In the photoelectric effect, to extract an electron from a cathode the photon energy should be more then the work function of the cathode material, and the kinetic energy of the electron is given by

$$K.E. = h\nu - \Phi_0 \quad , \tag{3.3}$$

where Φ_0 is the work function of the cathode material and *hν* is the photon energy. In a photocathode RF gun a high accelerating field gradient is applied to accelerate the photo-electrons, which lowers the work function of the cathode material due to the Schottky Effect [46]. This reduction in work function of the cathode material increases the initial kinetic energy of the photo-emitted electrons. The kinetic energy of electrons goes into transverse velocity and determines the starting emittance of the beam. This is the minimum possible emittance that can be achieved by the photo-injector and is called the *thermal emittance* of the beam. An estimate of the thermal emittance can be made by assuming emission as a thermalized distribution of electrons, with no correlation between position and momentum. With Lawson's [23] expression for RMS value of the momentum distribution, the normalized thermal emittance is given by

$$\varepsilon_0 = \frac{R_0}{2}\sqrt{\frac{2\delta E}{m_0 c^2}} = \frac{R_0}{2}\sqrt{\frac{2\left[h\nu - \left\{\Phi_0 - \sqrt{\beta_\gamma E_0 \sin(\theta_0)}\right\}\right]}{m_0 c^2}} \quad , \tag{3.4}$$

where R_0 is the transverse radius of the beam, δE is the kinetic energy of electrons, β_γ is the field enhancement factor of the photo electron emitting surface, E_0 is the peak accelerating field in the photocathode RF gun, and θ_0 is the laser injection phase with respect to RF (or phase of beam with respect to RF field). For a flat, clean copper cathode (Φ_0 =4.6 eV) and an accelerating field of 100 MV/m, the excess energy of an electron when the cathode is exited by 266 nm photon (*hv* = 4.65 eV) is 300 meV and thermal emittance is 0.6 π mm-mrad.

3.1.3 Space Charge Emittance ε_{SC}

In a photocathode RF gun electrons are born with almost zero energy and Coulomb repulsion between the electrons defocuses the beam and causes a growth in emittance, which is known as *space charge emittance* growth. Although this space-charge force reduces by a factor of $1/\gamma^2$ once the beam becomes relativistic (since the attractive magnetic force partly compensates the repulsive Coulomb force), initially, when the beam is non-relativistic, the space-charge force dominates and causes an immediate growth in emittance.

The space charge emittance in a 1.5 cell photocathode RF gun was analytically predicted by Kim [47] and is given by

$$\varepsilon_{sc} = \frac{\pi}{4}\frac{1}{\alpha k}\frac{1}{\sin(\theta_0)}\frac{I_p}{I_A}\mu_i(AR) \,, \tag{3.5}$$

where $\alpha = eE_0 / 2m_0c^2k$ is the normalized RF field parameter, E_0 is the peak accelerating field in the cavity, $k = 2\pi/\lambda_{RF}$ is the RF wave number, θ_0 is the phase difference between the electron beam and the RF field, I_p =17 kA is the Alfven current, and μ_i is the universal space-charge factor depending upon the Aspect Ratio (AR) of the electron beam which is the ratio of the transverse and longitudinal RMS beam sizes and is given by

$$\mu_i(AR) = \left\{ \frac{1}{2AR+5}, \; i = x,y \right. . \tag{3.6}$$

The typical space charge emittance for an electron beam of 1 nC charge in a 10 ps Gaussian pulse with AR of unity in a S-band photocathode RF gun operating with an accelerating gradient of 100 MV/m is 1.8π mm-mrad.

3.1.4 RF Emittance ε_{RF}

In an accelerating cavity with entry and exit ports, to satisfy the boundary conditions the accelerating field becomes radial at the entry and exit ports which apply a radial kick to electrons when they passes through the cavity. From this radial field the beam gets a focusing kick at the entrance of the cavity and a defocusing kick at the exit [34]. Due to the finite size of the beam in space and time, the magnitude of the defocusing kick at the exit is different for different particles, which causes growth in the emittance of the beam. This contribution to the emittance is known as the *RF emittance*. In a photocathode RF gun the defocusing kick at the exit of the half-cell is canceled by the focusing kick at the entrance of the full-cell, but the defocusing kick at the exit of the full-cell causes an increase in the beam emittance. The RF emittance in a 1.5 cell photocathode RF gun is predicted by Kim and given by [47]

$$\varepsilon_{RF} = \frac{\alpha k \sigma_{x,y}^2 \sigma_z^2}{\sqrt{2}} \ , \tag{3.7}$$

where $\sigma_{i=x,y,z}$ is the RMS beam size in the respective directions. In addition to this, if the amplitude of the accelerating field in two consecutive cells is not equal, then the defocusing transverse kick at the exit of the earlier cell is not canceled by the focusing kick at the entry of the next cell and there will be a growth in emittance. This emittance growth is given by a slightly modified version of equation (3.8) as

$$\Delta\varepsilon_{RF,FB} = \frac{e(E_n - E_{n+1}) k^2 \sigma_{x,y}^2 \sigma_z^2}{2 m_0 c^2 \sqrt{2}} \,, \tag{3.8}$$

where E_n and E_{n+1} are the fields in the n^{th} and the $(n+1)^{th}$ cell respectively.

3.1.5 Field Asymmetry or Structure Defect Emittance ε_{fa}

An accelerating structure has multiple ports for RF power feeding, vacuum pumping and for tuning of the resonant frequency. The presence of these ports breaks the rotational symmetry of the accelerating structure and scatters energy into the higher order TM_{m10} modes, and the total RF field becomes a linear combination of all of these modes. The lowest term, TM_{110} gives a dipole field which is most destructive to the transverse emittance of the beam. The estimates of the emittance dilution resulting from higher-order fields have been made by Chojnacki [18, 48] and Palmer [17] and scale as

$$\varepsilon_{fa} = \frac{e}{m_0 c^2} \frac{\lambda_{rf}}{2\pi} \sigma_{x,y} \sigma_z \int \frac{\partial E_{x,y}}{\partial x} dz \,. \tag{3.9}$$

3.1.6 Cathode Magnetic Field Emittance ε_{Bz}

In a photocathode RF gun electrons are born with a small kinetic energy and due to that have a radial component of velocity. This component of the radial velocity interacts with the magnetic field at the cathode caused by the emittance compensation solenoid and increases the beam emittance. This contribution is known as the *cathode magnetic field emittance* and is given by

$$\varepsilon_{Bz} = \frac{e}{8 m_0 c} R_0^2 B_z \,, \tag{3.10}$$

where R_0 is the radius of the laser spot on the cathode and B_z is the magnetic field on the cathode due to the solenoid. For an electron beam of 1 mm radius, the *cathode magnetic field emittance* scales as $\varepsilon_{Bz} = 0.01\pi$ mm - mrad/G . This term can be eliminated by using a bucking coil near the cathode plate which nullifies the magnetic field on the cathode plate.

Although the emittance of the beam from a photocathode RF gun can be predicted accurately by employing a beam dynamics code with electromagnetic field solver codes, a first-order estimate of the emittance can be predicted by employing the analytical formulations discussed above.

3.2 EMITTANCE COMPENSATION

3.2.1 Compensation of Space Charge Emittance:

Usually the electron beam produced by photoinjectors is space-charge dominated, and hence beam self-forces govern the evolution of the beam. All the electrons are emitted at very small energy (0.01-0.2 eV) and remain non-relativistic. The transverse beam size and beam emittance increase due to space-charge forces. A technique to suppress space-charge forces using a solenoid magnetic field was invented by Carlsten in 1989 and is known as *emittance compensation* [13]. Figure 3.1 shows the emittance compensation technique.

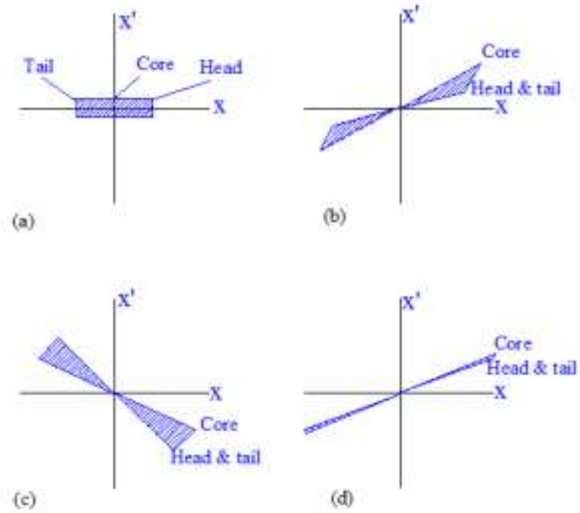

Fig. 3.1: (a) phase space diagram of initial beam with zero emittance, (b) phase space projection of beam after expansions due to self forces, (c) phase space diagram of the beam just after the solenoid magnet showing focusing, and (d) phase space projection of beam at the beam waist location, at which transverse emittance becomes minimum.

Carlsten made an assumption of independent envelope motion of the different longitudinal slices of the beam, which generate different phase space distributions of different beam slices. A solenoid magnetic field is applied to rotate the phase ellipse of all the beam slices. In due course of distance covered by the beam after the magnet, different slices of the electron bunch align in such a fashion as to minimize the total transverse normalized emittance. In the non-relativistic regime, the Coulomb repulsion in different slices of the bunch is different. The magnitude of the Coulomb repulsion at the core of the bunch is twice the value at the head and the tail. For a zero energy-spread beam, the emittance compensation magnet applies a transverse kick to individual electrons of the bunch proportional to their transverse position. The effect of unequal space-charge forces in the bunch and its counter kick due to magnetic fields rotates the projected transverse phase space of different slices. At some position, 'z_0' in the drift region all the projections of different beam slices get aligned and give minimum normalized transverse RMS emittance. A booster linac is placed at the location of minimum emittance, which further accelerates the beam to a high energy as a consequence of which the transverse space charge forces will be eliminated by the $1/\gamma^2$ effect. Hence, the beam emittance is frozen.

The Carlsten model was generalized by Serafini and Rosenzweig (SR) to the case of a beam generated and accelerated by a multi-cell structure comprising of a photocathode and accelerating cells, *i.e.* the integrated RF photoinjector. Their approach is based on the RMS beam envelope equation to describe the propagation of each slice of the electron bunch, and the model is termed as invariant envelope (IE) [49]. PARMELA simulations are used to explore the phenomenon of emittance compensation in more detail. This initiated experimental and theoretical development in the area of production, transport and preservation of space charge dominated beams. The theoretical modeling of emittance compensation developed by Serafini & Rosenzweig shows that the amplitude of oscillations of a space-charge dominated electron beam is independent of the current of the longitudinal slices of the bunch. There are effectively four parameters governing the beam trajectory: accelerating field, magnetic field, aspect ratio and current. For emittance compensation, the magnetic field forces should be equal to the space-charge forces and the beam should go through a beam waist in the drift space after the photoinjector.

3.2.2 RF Emittance Compensation

Several methods have been proposed to compensate the emittance growth due to time dependent RF fields. The techniques of lengthening of first cell, unsymmetrical extra cell and RF quadrupole cell allow the reduction of the linear, time-dependent RF field induced emittance by factor two to five [50-54]. Serafini *et al.*have shown that odd harmonic modes can be used to cancel the RF induced emittance [55]. They showed using simulations that the superimposition of the 3^{rd}, 7^{th} … harmonics to the fundamental, reduces the RF induced emittance by an order of magnitude. The major advantage of this technique is that the minima for transverse and longitudinal emittances occur for the same input phase ϕ_0. Although this method looks very promising to compensate the RF induced emittance, it is very difficult to build and power a cavity able to support several harmonics at a time.

3.2.3 Field Aasymmetry/Multipole Mode Emittance Compensation

The emittance growth due to field asymmetry or multi-poles in a photocathode RF gun is due to the presence of ports for different purposes. In principle by removing the ports asymmetry can be removed; however at least one port for RF power feeding and one port for vacuum pumping are necessary. Since it is not possible to remove the ports, Palmer has proposed to make all ports identical in shape and opposite to each other [17]. This minimizes the field asymmetry and therefore the emittance growth due to that asymmetry.

3.3 PHOTOCATHODE RF GUN DESIGN: SCALING OF DIFFERENT PARAMETERS

The design and optimization of an RF photoinjector for desired beam parameters is an iterative process due to the involvement of detailed RF and magnet design calculations along with multi-particle beam dynamics simulations. Although photocathode RF guns can be designed using electromagnetic field solver codes along with beam dynamics codes, an analytical understanding and scaling laws devised for different beam parameters considering the practical and technological limitations, are very useful and a time saving tool to make the first round choice of parameters to meet the desired specifications [47, 56, 57]. Kim derived analytical scaling laws to design a photocathode RF gun considering n+1/2 cells with a pure sinusoidal accelerating field without solenoid magnetic field focusing, and assuming that the bunch length is small compare to an RF period and the energy of electrons increases very rapidly such that there is no slippage of electrons with respect to the RF. It is also assumed that there is no radial and longitudinal expansion of the beam during acceleration. Kim has derived scaling laws by solving the dynamic equations of electron motions in longitudinal and transverse directions given by

$$\frac{d\gamma}{dz} = \alpha\left[\sin\left(k_z z - \omega t + \phi_0\right) + \sin\left(k_z z + \omega t + \phi_0\right)\right], \tag{3.11}$$

$$\frac{d\phi}{dz} = k_z\left[1 - \frac{\gamma}{\sqrt{\gamma^2 - 1}}\right], \tag{3.12}$$

where γ is the relativistic factor of the beam, ϕ is phase between electron and forward components of standing wave (accelerating), and other parameters are as defined earlier. For a short bunch of Gaussian distribution in the longitudinal and transverse directions, Kim had given analytical expressions for the following beam parameters at the gun exit: γ, RMS energy spread, RMS relative energy spread, RMS angular divergence and RF and space-change emittance. The assumptions made in Kim's model are fulfilled only when the relativistic factor γ of the beam becomes two in the middle of the first cell [56]. Due to the above constraints Kim's model work well for longer structures but gives errors for shorter structures. Travier extended Kim's model and derived empirical scaling laws that give reasonably good agreement with the beam dynamics code PARMELA [56]. The scaling laws derived by Travier are given here in practical units:

$$\alpha = 46.7 \frac{E_0[MV/m]}{f[MHz]}, \tag{3.13}$$

$$\gamma = 1 + 146.8(n + 0.5)\frac{E_0[MV/m]}{f[MH_z]}, \tag{3.14}$$

$$\sigma_{\Delta\gamma} = 2.9 \times 10^{-4} E_0[MV/m]\sigma_b[ps], \tag{3.15}$$

$$\frac{\Delta U}{U}[\%] = 2 \times 10^{-4}\ \frac{f[MHz]\sigma_b[ps]}{n + 0.5}, \tag{3.16}$$

$$\sigma_x^{'}[mrad] = \frac{E_0[MV/m]\sigma_x[mm]}{\gamma}, \tag{3.17}$$

$$\varepsilon_{RF}[mm - mrad] = 2.73 \times 10^{-11} E_0[MV/m] f^2[MHz]\sigma_x^2[mm]\sigma_b^2[ps], \tag{3.18}$$

$$I_p[A] = 399\frac{Q[nC]}{\sigma_b[ps]}, \tag{3.19}$$

$$\phi_\infty[\deg] = \phi_0[\deg] + \frac{f[MHz]}{E_0[MV/m]} \times \left(\frac{0.61}{\sin(\phi_0[\deg]) + 4.4\sqrt{\frac{f[MHz]}{E_0[MV/m]}}} + 0.26 \right), \tag{3.20}$$

$$\varepsilon_{sc}[\pi \;\; mm - mrad] = 3.76 \times 10^{3} \frac{Q[nC]}{E_0[MV/m](2\sigma_x[mm] + \sigma_b[ps])} \;, \qquad (3.21)$$

where E_0 is the peak accelerating field, f is the RF frequency, σ_x is transverse RMS beam size, σ_b is the RMS bunch length, ϕ_0 and ϕ_∞ are the phase of the central particle in the bunch at the cathode and at the gun exit respectively, other symbols have the same meaning as given earlier. Although by solving Eqs. (3.13-3.21) the required gun design parameters can be predicted, in order to obtain a realistic design practical or technological limitations concerning the frequency range, maximum accelerating field achievable in an RF cavity, the maximum beam size and bunch length, the charge density extractable from the cathode, the thermal emittance at the cathode, cathode material and laser parameters have also to be taken into account.

3.4 PHOTOCATHODE RF GUN DESIGN: SELECTION OF DIFFERENT PARAMETERS

In order to realize a working photocathode RF gun, before going ahead to finalize the design the technological limitations and practical issued related to successful operation have to be considered as discussed below.

3.4.1 Frequency

Selection of RF frequency depends upon many factors like machining ability, vacuum requirement, bunch length and laser pulse width *etc*. If the frequency is too low then the dimensions of the cavity become very large and it is difficult to achieve the desired vacuum, on the other hand if the frequency is too high then the mechanical tolerances become too stringent and difficult to achieve. For higher frequencies the RF period becomes shorter and requires a shorter laser pulse to produce an electron beam with minimum energy spread. In addition, the selection of the RF frequency is also dictated by the ready availability of an RF power source at that frequency. The scaling of different parameters of the photocathode RF gun with RF frequency is given in Table 3.1.

Table 3.1: Scaling of RF parameters of photocathode RF gun with frequency.

Transverse dimensions	f_0^{-1}
Power dissipation	$1/\sqrt{f_0}$
Shunt impedance	$\sqrt{f_0}$
Volume	f_0^{-2}
Stored energy	f_0^{-2}

3.4.2 Maximum Electric Field

It is clear from Eq. (3.5) that the space-charge emittance is inversely proportional to the electric field, and hence to minimize it the electric field should be as high as possible. In an RF cavity the maximum achievable electric field increases with the frequency and is limited by dark current. In 1895 Kilpatrik [58] has given an analytical formulation of the break-down limit as a function of frequency, based on experimental results, which is known as the *Kilpactrik limit* and is given by

$$0.64 E_0[MV/m] e^{-(9.5/E_0[MV/m]} \leq \sqrt{f[MH_z]}. \tag{3.22}$$

The breakdown limit increases with surface finish, and hence nowadays electric field gradients up to five to six times the Kilpatrik limit can be achieved. The simplified expression for the maximum achievable electric field with frequency is

$$E_{0.\max}[MV/m] = 8.47 + 15.7\sqrt{f[MHz]}. \tag{3.23}$$

3.4.3 Maximum Beam Size and Beam Exit Aperture

The electric field near the beam exit aperture is non-linear and if the beam size is more than a certain value then it sees a non-linear electric field and the beam size increases significantly. As a thumb rule to minimize the beam growth, the beam size should be a third of the cavity aperture radius, which reduces with frequency. For the BNL/SLAC/UCLA design the maximum beam size is given by

$$\sigma_x[mm] \leq \min imum\left(10, \frac{10^4}{f[MHz]}\right). \tag{3.24}$$

To accommodate a larger beam size, one can design the cavity with a larger aperture but the resultant increase in the RF field leakage reduces the shunt impedance of the cavity and to achieve same energy gain more RF power is required.

3.4.4 Photocathode

Ideally a photocathode for photo-injector operation should have a high quantum efficiency (>1%) at low energy (infra-red or visible wavelength), very fast response time (<ps), very long life time (several months or years), high damage threshold, accept high electric field, be capable of working under moderate vacuum conditions, be easy to prepare and install in the gun cavity. Unfortunately, no known cathode material has all these qualities. Metallic cathodes have attractive features like they are easy to prepare, can operate under moderate vacuum conditions and have long life time, but their Quantum Efficiency (QE) is very poor, of the order of 10^{-4}-10^{-5}, and they require UV lasers with high energy. On the other hand the alkali semiconductor photocathodes have high QE of the order of 1-4%, but these are difficult to prepare, have short

life time, cannot sustain very high field gradients and require very good vacuum, of the order of 10^{-9} mbar. The compounds of the alkali-antimonide family (Cs_3Sb, K_3CsSb, $Na_2K(Cs)Sb$, etc.) work in the visible with a QE approaching 40% but are unable to sustain high electric fields and have a very short life. Another family, alkai-telluride photocathodes (Cs_2Te, Rb_2Te, K_2 Te *etc*.), have high QE (more than 20%), are able to sustain high electric field and also have reasonably long life (few week to months) but are sensitive to oxidization and hence require Ultra-High Vacuum (UHV) and also require a UV laser for photoemission. Although III-V semiconductors with negative electron affinity (NEA) given by co-adsorption of Cs and oxygen, are efficient photo-emitters in the visible and infra-red region with QE up to 40-60%, these are very sensitive to chemical contamination and ion back-bombardment and to avoid that require UHV in the range of 10^{-12} mbar, are unable to sustain high electric field, have a slow response (~100s of ps to few ns) and are thus not suitable for bunch train operation [59, 60]. Dispenser photocathodes (LaB_6, WcaOBaO, *etc*.) have QE slightly more than metallic cathodes, can sustain high electric field and also have long life but require to be heated prior to operation. A summary of commonly used photocathode materials with their advantages and limitations is given in Table 3.2.

There is no unique way to select the photocathode material and it depends upon the application. Typical cases are as follows:

- If a single pulse of charge between 1-5 nC is required then a Cu or Mg photocathode is probably the best choice.
- If a train of pulses with charge around few nC are required, then Cs_2Te is the best choice.
- For very high repetition rate or high duty cycle and high charge per pulse, CsK_2Sb is the best choice.

Table 3.2: Commonly used photocathode material, their advantage and drawbacks.

Photocathode	Advantage	Limitations/ drawback
Metallic Cu, Mg, Ag etc.	Easy to prepare and installed Long life fast response time moderate vacuum	Low quantum efficiency Need UV laser Pulse train and high average operation is not possible Electron beam follow the fluctuation in drive laser
Alkai Semiconductors (Gs_2Te, K_2Te, GaN *etc.*	High QE (5-30%) Long life (few weeks to months) Sustain high electric field	Difficult to prepare and install Need good vacuum Need UV laser
Alkali-antimonide Cs_3Sb,K_3CsSb, $Na_2K(Cs)Sb$, etc.	High QE (30-40 %) Work at visible laser	Difficult to prepare and install Short life Cannot sustain high electric field Need UHV
NEA semiconductor GaAs, InGaAs-AlGaAs	High QE (40-60%) Work at IR and visible laser Polarized electron source	Difficult to prepare and install Sensitive to chemical contamination and ion back-bombardment Require vacuum in the range of 10^{-12} mbar Unable to sustain high electric field, Long response (~100's of ps to few ns) Not suitable for bunch train operation.
Dispenser photocathode LaB_6, WcaOBaO	Medium QE Long life	Need to be heated prior to operation

3.4.5 Drive Laser

The temporal and transverse profile of the electron beam in a photo-injector is governed by the laser parameters. The intensity, phase and position stability of the electron beam are directly related to the laser stability and reliability. The wavelength of the laser must be short enough for photo-emission (below the threshold wavelength of the cathode being used). To produce a mono-energetic electron beam the pulse-width of the laser should be less than a few tenths of the RF period. The power of the laser depends upon the peak charge and quantum efficiency of the cathode being used and is given by

$$\mathrm{Q} = \frac{\eta e W \lambda_L}{hc}, \tag{3.25}$$

where λ_L is the wavelength and W is the energy of the laser pulse, Q is the total charge of the electron beam and η is the quantum efficiency of the photocathode. In practical units the above relation may be written as

$$\mathrm{Q}[\mathrm{nC}] = 8.07\times10^{-3}\eta[\%]W[\mu]\lambda_L[nm]. \tag{3.26}$$

To minimize the variation in bunch to bunch charge and energy stability, the pulse to pulse energy spread in the laser should be minimum. To maintain the bunch to bunch energy spread in electron beam the laser must be synchronized with the RF, which means that the laser oscillator frequency must be sub-harmonic of the RF with a typical jitter of $\leq$1ps RMS.

SUMMARY

Theory of photocathode RF guns was discussed. Different terms contributing in the emittance and methods to compensate them were detailed. The scaling laws for selection of photocathode

RF gun parameters were discussed, especially those that are useful to select initial parameters for a design study through simulations.

CHAPTER 4

RF DESIGN AND BEAM DYNAMICS SIMULATIONS

INTRODUCTION

Although the design of an actual RF accelerating structure is simplified if scaling laws or a comprehensive theory can give precise physical dimensions corresponding to the specified field requirements or vice versa, in practice none of the accelerating structures lend themselves to a straightforward field analysis. All the analytic techniques have to make use of simplifying models or assumptions, which may not be valid for complex accelerating structures. Therefore one has to take recourse to numerical simulations, and the validity of the simulations can be verified through a few cold-test models of the structure. Therefore, most realistic way to accelerating structure designs is using various computer codes [61, 62]. However, the initial design parameters derived from analytical considerations may be a useful starting point for the numerical simulations, in order to reduce the time for optimization. Hence in this chapter we describe the initial RF design parameters predicted from scaling laws. Then numerical codes are used to design the structure and the electromagnetic fields predicted by simulations are then used for beam dynamics simulations.

4.1 INITIAL DESIGN PARAMETERS

The photocathode RF guns used for FEL applications are required to generate electron bunches of 1-5 nC charge in ~10 ps duration with transverse emittance of < 2π mm-mrad and energy of 3-4 MeV. Since we have an RF source operating at 2856 ± 5 MHz we chose to build a 1.6 cell BNL/SLAC/UCLA type S-band photocathode RF gun capable of sustaining an on-axis accelerating field gradient of ~75 MV/m.

Using the scaling law for maximum field, Eq. (3.23), at 2856 MHz the peak achievable accelerating field is 92 MV/m (actually it could be 2-3 times more depending upon machining quality); hence an accelerating field gradient of 75 MV/m is well within the safe limit. As the charge required per bunch is between 1-5 nC, copper is the most suitable cathode material. According to the scaling law the beam exit aperture radius should be more than three times to the beam size (σ_x), which is ~ 3 mm in our case; to be on safer side we take a further margin of 30%, and hence the aperture radius should be greater than 12 mm. A comparison of the initial design parameters with the limiting parameters is given in Table 4.1.

Table 4.1: Comparison of maximum limitation as per scaling law and initial design parameters for photocathode RF gun.

Parameter	Maximum limitation as per scaling law	Initial design parameters
Frequency	114 MHz $\leq f \leq$ 17000 MHz	2856 MHz
Maximum field (MV/m)	92	75
Maximum beam size (σ) mm	3.5	3
Maximum bunch length σ_b (ps)	17.5	5.2
Peak charge (nC)	11.25	1-5
Beam exit aperture (diameter) (mm)	>18	25

4.2 RF DESIGN OF PHOTOCATHODE RF GUN

4.2.1 Simulation Codes

The electromagnetic field solver codes solve Maxwell's equations by applying the boundary conditions at the surface of the geometry of the structure. Many such codes are commercially available [61]. We used the 2-D code SUPERFISH and 3-D code CST Microwave Studio (CSTMWS) for RF design of the photocathode RF gun. Brief descriptions of these codes are given below.

4.2.1.1 SUPERFISH/POISSON

SUPERFISH/POISSON is a 2-D electromagnetic field solver code developed by LANL, USA and is used for azimuthally symmetric structures [63]. The code SUPERFISH is a combination of many modules to define the geometry, to generate the mesh, solve for the electromagnetic field, post-processor and plot the electromagnetic field parameters and data for beam dynamics simulations. In SUPERFISH the geometry of the structure is defined in the 2-D plane x-y, where x denotes the longitudinal direction while y denotes the radial direction. All the dimensions are given in cm. The AUTOMESH model generates a mesh of the structure and applies boundary conditions. Field solver module FISH solves for the resonant frequency of the structure and generates a binary file with an extension of T35, which is used by other post-processors. Subroutine SFO calculates the electromagnetic field parameters of the eigenmode supported by the structure and WSFPLOT is used to plot field contours and has options for plotting the magnetic field circles and electric field arrows. SUPERFISH starts calculations with the approximate frequency given in the input file and changes the wave parameters to find the convergence for resonant frequency at which all the boundary conditions are well satisfied. Post-processor SF7 is used to generate the field data along any line in the structure and is used to generate the accelerating field map written in TAPE7 file to be used in the beam dynamics code PARMELA as inputs for beam dynamics studies. Another module POISSON/PANDIRA used to design magnets. The magnetic field mapping from the POISSON output can be directly fed into PARMELA input file using output of POISSON with extension PO7.

4.2.1.2 CST Microwave Studio

Most RF accelerating structures are not axi-symmetric due to the presence of different ports for RF power feeding, vacuum pumping and tuning *etc*. Therefore they cannot be designed accurately by using a 2-D code like SUPERFISH and need 3-D codes. We used CST Microwave Studio (Computer Science Technology, Microwave Studio-CSTMWS) which is available commercially [64]. CSTMWS uses the finite integration technique to solve Maxwell's equations for a defined structure geometry. It has an eigen-solver module to calculate the resonant frequency and electromagnetic field distributions for possible modes in a given frequency range, assuming the structure is made of PEC (Perfect Electrical Conductor) and ignoring losses in the material. To design the actual structure made of metals with finite conductivity, the code provides the 'time domain' and 'frequency domain' solvers. The quality factor, shunt impedance, transit time factor and variation in field components along any direction can be calculated using post-processors provided in the code. The RF power coupler can also be designed using the either 'time domain' solver or 'frequency domain' solver. The code has many options for meshing the structure geometries like uniform meshing (AUTOMESH), Perfect Boundary Approximation (PBA) and Fast Perfect Boundary Approximation (FPBA). AUTOMESH generates a uniform mesh in all directions, while PBA generates variable meshes in the structure to match the boundaries. FPBA is a refined version of PBA and used for structures having sharp boundaries. The accuracy of the simulations increases with decreasing mesh spacing, which is defined as the number of mesh points per wavelength of the highest frequency of interest, but the simulation time and memory requirement also increases rapidly with the total number of mesh points. The simulations need to be optimized for convergence of RF parameters for a simple pillbox type structure with mesh points such that RF parameters do not vary further with an increase in the number of mesh points. Therefore the actual structure needs to be designed with optimized mesh points per wavelength to obtain accurate results.

4.3 RF DESIGN SIMULATIONS

The first step in evolving a physics design of the photocathode RF gun is to determine its geometrical dimensions using analytical formulations, for the initial RF parameters derived from simple scaling laws as discussed in Section 4.1. The next step is to model the structure and optimize its geometry to achieve the desired RF parameters and to optimize the shunt impedance, bandwidth, inter-cell coupling, and transit time factor using SUPERFISH. Then determine the variation in RF parameters with different dimensions of the structure to find out the tolerances for fabrication. After obtaining the preliminary dimensions using SUPERFISH, the next step is to introduce the port openings for the RF, vacuum and laser, and then further optimize the geometry using the 3-D code CSTMWS.

4.3.1 Geometry Description

The 2D schematic of the BNL/SLAC/UCLA type photocathode RF gun is shown in Fig. 4.1. The RF power is coupled through a single port in the full-cell and to avoid exciting the dipole mode the vacuum port is placed diametrically opposite the RF port in the full-cell. Two ports orthogonal to RF and vacuum ports are also provided in the full-cell for frequency tuning. The cell-to-cell power coupling takes place through the central aperture meant for beam transport. Two ports for entry and exit of the laser are provided in the half-cell.

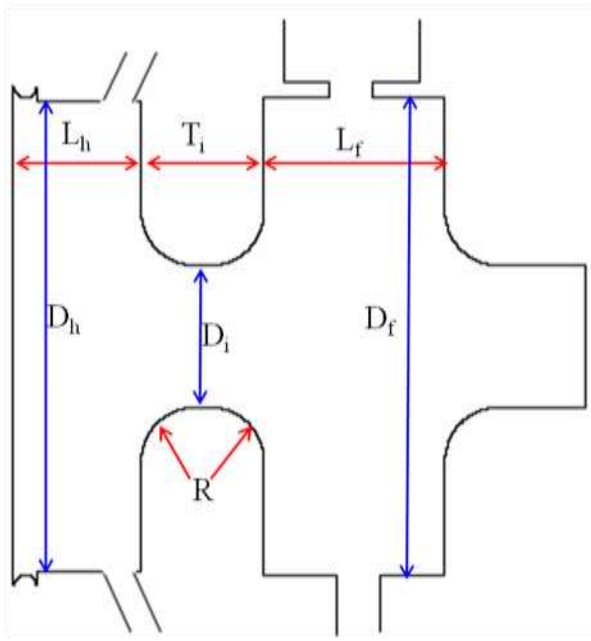

Fig. 4.1: 2D schematic of the 1.6 cell BNL/SLAC/UCLA type S-band photocathode RF gun.

4.3.2 SUPERFISH Simulations

The gun is modeled without ports in SUPERFISH. As the gun contains two cells it supports two normal modes, the '0' and 'π' modes. The latter is used for acceleration due to higher shunt impedance. The geometrical dimensions are optimized to obtain the π-mode at 2856 MHz with field balance or electrical balance (e_b = ratio of on-axis field in half-cell to that in full-cell) of unity and maximizing the quality factor and shunt impedance. The electromagnetic field contour and arrow plot for the π-mode is shown in Fig. 4.2, while the variation in on-axis accelerating field along the structure length is shown in Fig. 4.3. The electrical properties of the π-mode and geometrical dimensions are given in Table 4.2.

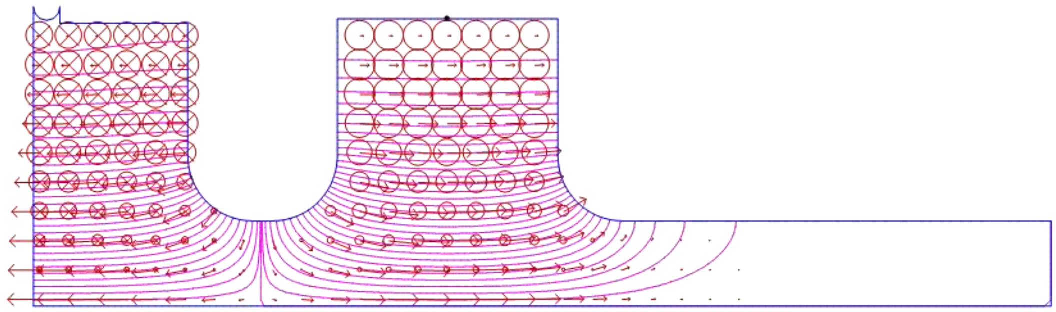

Fig.4.2: Field contour and field arrow plot of the π-mode in the photocathode RF gun.

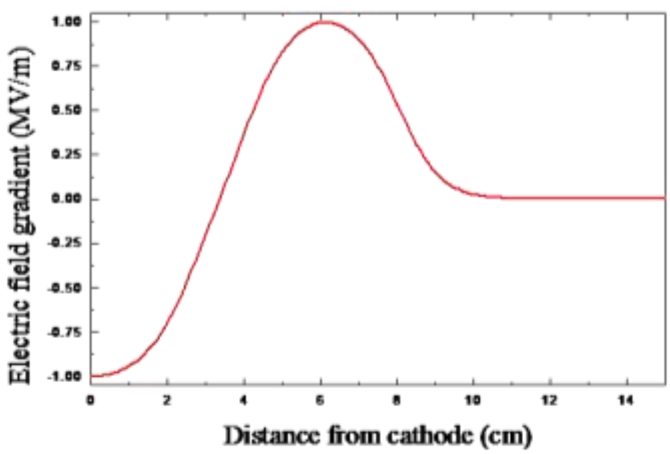

Fig. 4.3: On-axis electric field variation along the length of the photocathode RF gun.

4.3.3 CST Microwave Studio Simulations

With the dimensions predicted from SUPERFISH, the gun was again simulated in CSTMWS with ports for RF, vacuum, tuning and laser. The dimensions of the RF port were optimized for β_π and

$e_b \approx 1$, and the vacuum port dimensions were also made the same as the RF port to avoid exciting the dipole mode. The tuning port dimensions were chosen to minimize the perturbation in the on-axis accelerating field while still maintaining a wide frequency tuning range, hence it was made circular with a 9.5 mm diameter. The laser ports were made elliptical in shape with minor axis of 6 mm (to allow the laser to pass through) and major axis of 22 mm (to provide alignment of laser on cathode). The presence of these ports changes the π-mode frequency which was again tuned to 2856 MHz by varying the inner diameters of both the cells. The electrical properties of the π-mode and geometrical dimensions of photocathode RF gun predicted by simulations are given in Table 4.2.

Table 4.2: Electric properties of the photocathode RF gun predicted by simulations.

	SUPERFISH	CSTMWS		
Parameters		Without ports	With ports	
			Eigen-solver module	Time domain solver module
Φ_h (mm)	82.98	83.220	83.106	83.256
Φ_f (mm)	84.40	83.720	83.310	83.381
L_{RF} (mm)			21	21
f_π (MHz)	2856	2855.72	2855.94	2856.09
Q_0	15348	14893.35	14747.45	15438.37
Q_{ext}			14458.28	14646.66
β_π			1.02	1.05
R_{sh}/Q_0 (Ω)	265	265	268	
$(\lvert E_h/E_f \rvert)$	1	0.98	1.01	1.05

The arrow plot of the accelerating field in tuned photocathode RF gun predicted by CSTMWS is shown in Fig. 4.4 while the variation in on-axis accelerating field in shown in Fig. 4.5. The variation in $|S_{11}|$ with frequency is shown in Fig. 4.6 while Smith chart is shown in Fig. 4.7.

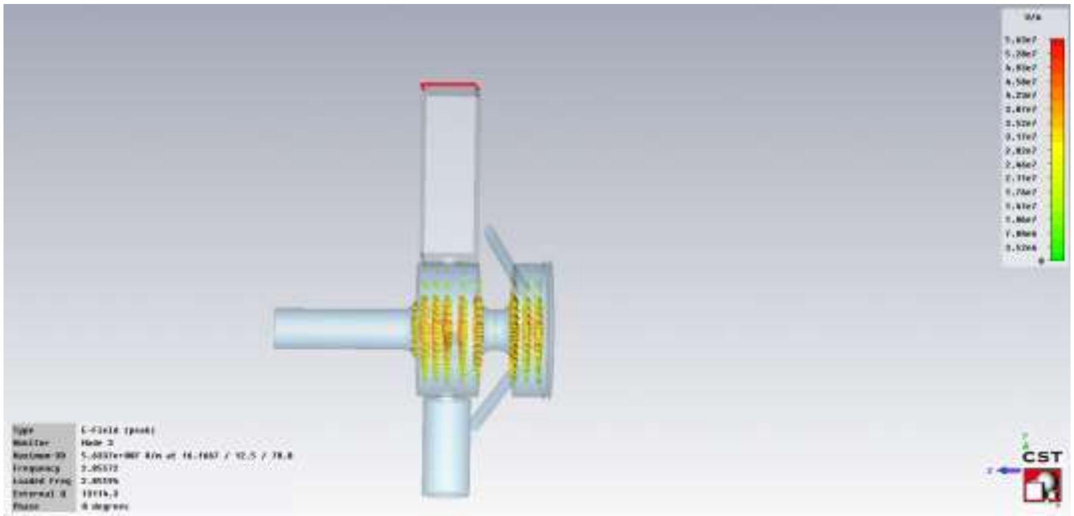

Fig. 4.4: Arrow plot of accelerating field in photocathode RF gun, predicted by CSTMWS.

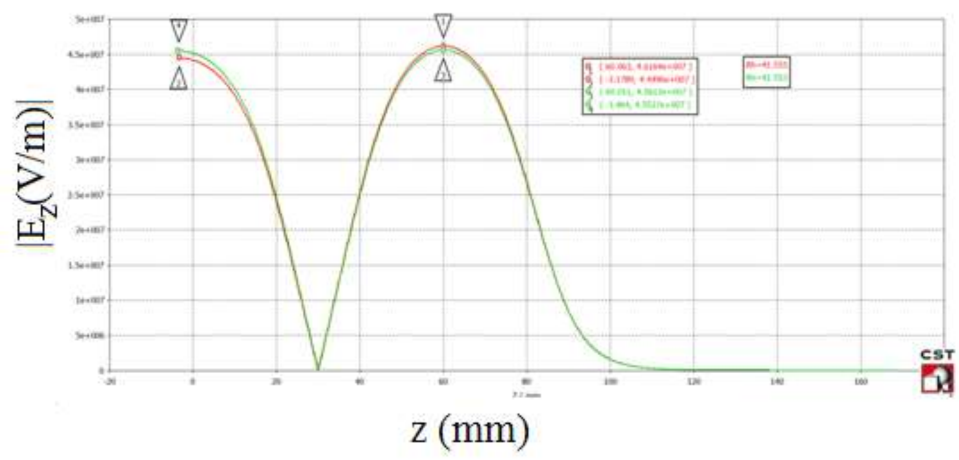

Fig. 4.5: Variation in on-axis accelerating field along the length of photocathode RF gun.

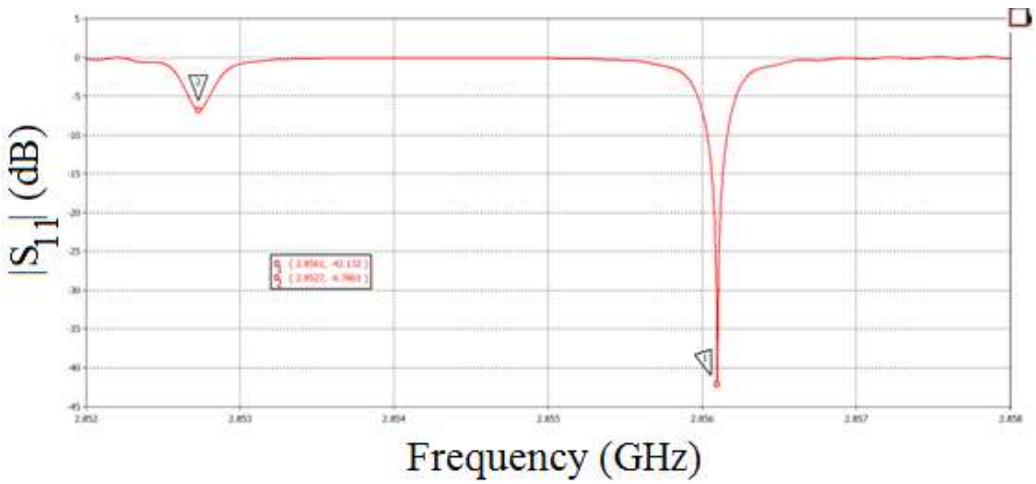

Fig. 4.6: Variation in $|S_{11}|$ with frequency of photocathode RF gun.

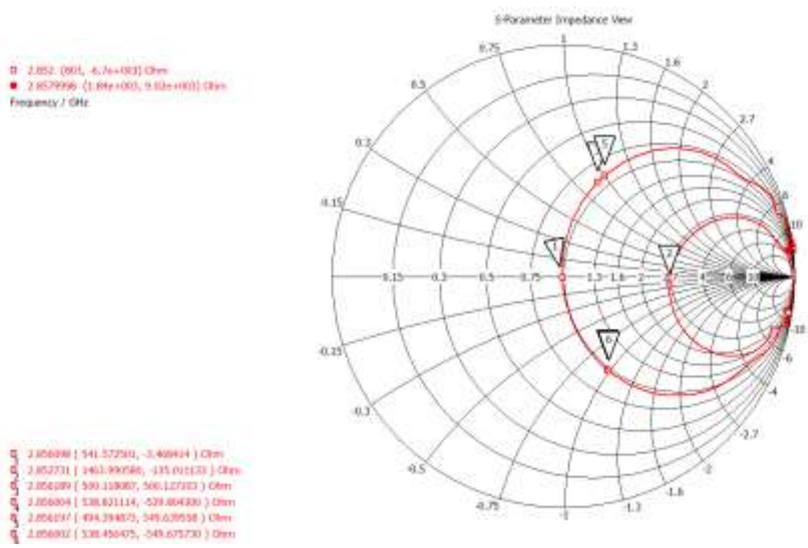

Fig. 4.7: Smith chart of tuned photocathode RF gun.

4.4 PREDICTION OF GEOMETRICAL TOLERANCES

Simulations can give the exact gun geometry needed to achieve the desired RF parameters; however, during fabrication it is not possible to achieve the exact dimensions due to machining errors and the achieved dimensions are within a finite tolerance band, depending upon the machining procedure employed. This variation in dimensions causes a deviation in the RF parameters from the design values, and therefore the tolerance band should be kept as small as possible; however it increases the machining cost rapidly. The variation in a particular RF parameter is very sensitive to a particular dimension; for example, the resonant frequency is very sensitive to the ID of the cavity while it is negligibly affected by the length of cavity. Similarly, the waveguide to cavity coupling coefficient depends critically upon the length of the RF coupling slot while its dependence upon ID of the cavity is not significant. Therefore, it is important to know the sensitivity of different RF parameters on different geometrical dimensions in order to prescribe the tolerances on them. A detailed simulation study was performed to predict the tolerances required on the various geometrical dimensions for fabricating the gun. The geometrical tolerances are obtained by deliberately introducing errors in the relevant dimensions and noting their effects on the RF properties of the gun. As discussed later in Section 4.5 the resonant frequency of the photocathode RF gun can be varied by cooling water temperature by ~-50 kHz/°C [65]. Hence, assuming an available operating temperature variation range of 10°C (30° ± 10°C) the frequency of the photocathode RF gun can be tuned by ± 0.5 MHz by varying the cooling water temperature. Therefore the simulations were re-done by varying the gun dimensions for π-mode frequency range of ± 0.5 MHz to study the variation in

e_b. The variation in the π-mode frequency and e_b with the half-cell and full-cell radius (R_{ch} and R_{cf} respectively) are shown in Figs. 4.8 and 4.9 respectively. The variation in shunt impedance and quality factor due to radius of half- and full-cells are negligible. The variation in π-mode frequency and e_b with inter-cell coupling iris radius is shown in Fig. 4.10.

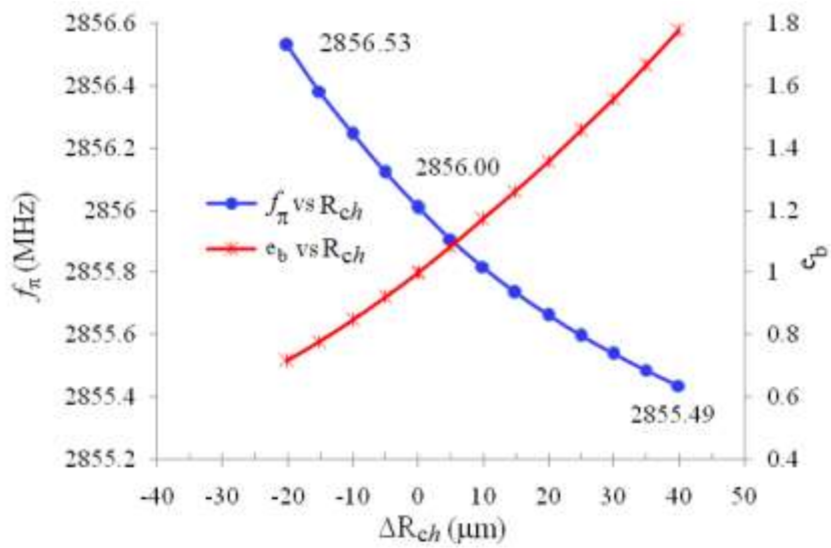

Fig. 4.8: Variation in frequency and e_b of π mode with half-cell radius while full-cell radius is fixed for e_b =1, f_π =2856 when ΔR_{ch}=0.

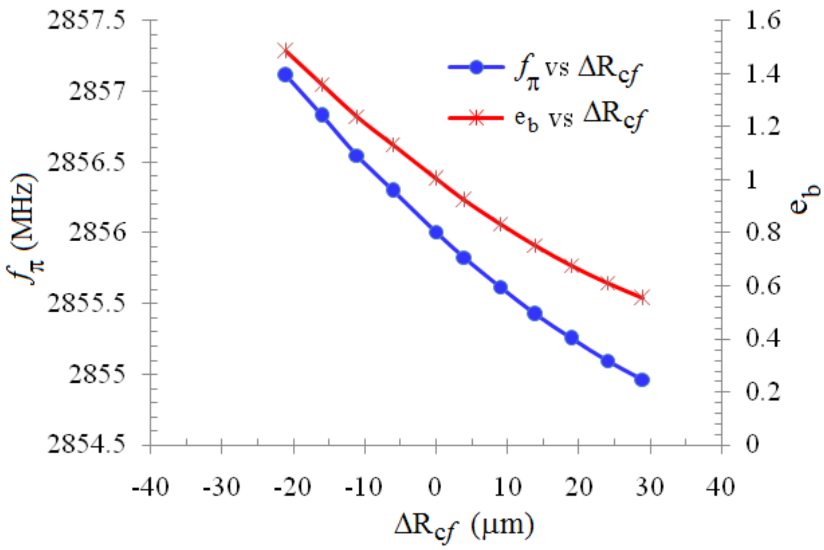

Fig. 4.9: Variation in frequency and e_b of π mode with full-cell radius while half-cell radius is fixed for e_b =1, f_π =2856 when ΔR_{cf} = 0.

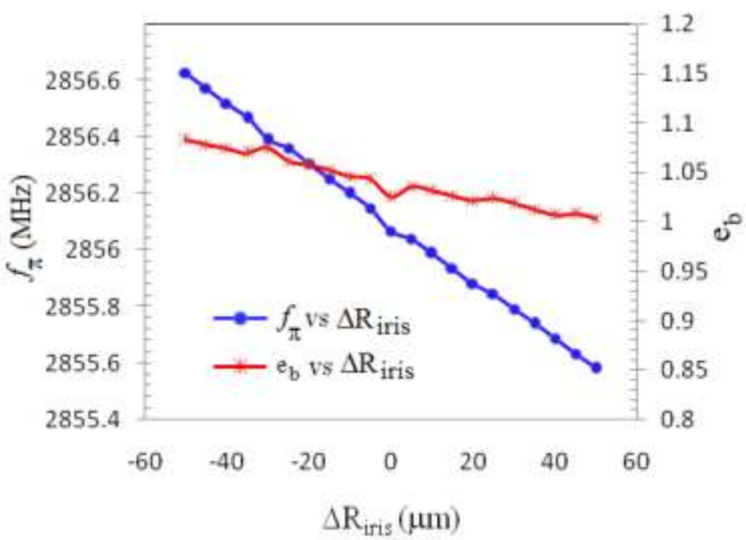

Fig. 4.10: Variation in π-mode frequency and e_b with variation in inter-cell coupling iris radius.

Simulations predicted a change of 11.25 MHz/mm in f_π due to perturbations in the full-cell diameter and 10.5 MHz/mm with the half-cell diameter. Besides f_π, e_b also varies with any change in the full- as well as half-cell diameters, while the quality factor and shunt impedance are almost unchanged. The variation in f_π with profile radius of the inter-cell coupling iris and beam exit port is -10 MHz/mm while variation in e_b, quality factor and shunt impedance are negligible. Resonant frequency perturbation due to change in the full- and the half-cell length is predicted to be about 12.5 MHz/mm and 10 MHz/mm respectively. Simulations show that the photocathode RF gun is very sensitive to geometrical perturbations; hence fabrication is constrained by strict machining tolerances, typically of the order of 10-20 μm to achieve the f_π within ± 0.5 MHz with e_b within 1±0.2. Different dimensions and tolerances predicted by simulations are summarized in Table 4.3.

Table 4.3: Geometrical dimensions and their effect on RF parameters of a photocathode RF gun.

Geometry	**Dimension (mm)**	**δf (MHz/mm)**
Half-cell diameter	83.256	-10.5
Full-cell diameter	83.381	-11.25
Inter-cell coupling iris	25.00	-10.0
Half-cell length	22.758	12.5
Full-cell length	32.513	10.0
Sealing width	3.910	4.0
Inter-cell coupling iris thickness	19.050	10.0

4.5 THERMAL SIMULATIONS

The cooling circuit to remove the heat dissipated in the gun structure to RF power dissipation was designed using the Finite Element Analysis (FEA) code ANSYS [66] as shown in Fig. 4.11. Temperature variation in the gun structure for a peak accelerating gradient of 147 MV/m with cooling is shown in Fig. 4.12. With the cooling water temperature of 30^0 C at a flow rate of 1.8 m/s, f_π reduces by 200 kHz to 2855.8 MHz while e_b varies from 1.042 to 1.044 which is negligible as the heating of the gun is uniform as shown in Fig. 4.13. The predicted variation in f_π with temperature is -46 kHz/^{0}C, therefore by reducing the cooling water temperature by 4^0C f_π can be tuned to 2856 MHz [65].

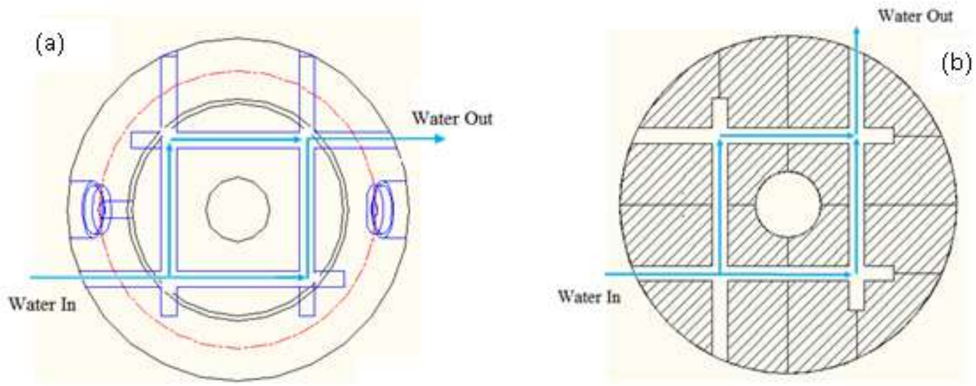

Fig. 4.11: Cooling channels for (a) half and (b) full-cells.

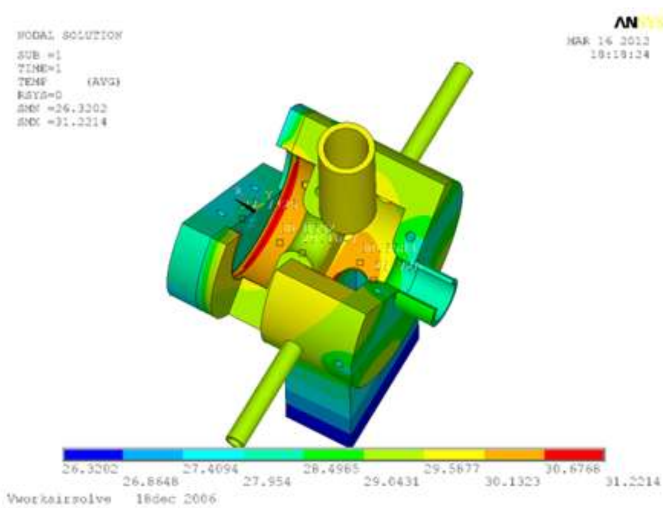

Fig. 4.12: Temperature variation in gun structure with cooling.

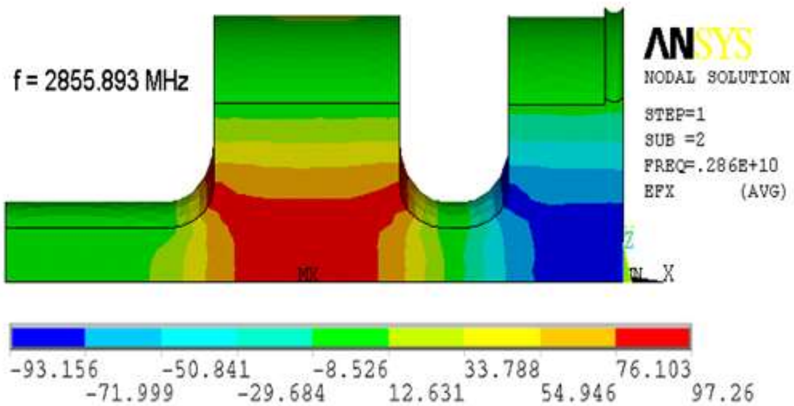

Fig. 4.13: The axial electric field (not to scale) in photocathode RF gun and detuned frequency for 2 Hz RF duty cycle.

4.6 BEAM DYNAMICS SIMULATIONS

The photocathode RF gun was designed to provide an electron beam of 1-5 nC charge with energy of ~3-5 MeV and normalized transverse emittance of < 2π mm-mrad. For optimization of the electron beam parameters for desirable performance of the photocathode RF gun, beam dynamics studies were performed using the beam dynamics code PARMELA.

4.6.1 PARMELA

PARMELA is a widely used program to simulate electron beam dynamics in linear accelerator and in photocathode RF gun. PARMELA is an acronym of **P**hase **A**nd **R**adial **M**otion in **E**lectron **L**inear **A**ccelerators. PARMELA was originally developed in 1980 by Kenneth Crandall at Los Alamos National Laboratory (LANL) and later was modified by Lloyd Young to include the use of photocathode RF gun and it continues to be developed and maintained by the Los Alamos Accelerator Code Group (LAACG) [67]. PARMELA tracks the beam represented by a collection of macro-particles, through a user-defined beam line. The beam line can be constructed from a wide variety of elements including standing and traveling wave RF accelerating structures, solenoid, dipole, and quadrupole magnets, drift space and many more type of elements. It computes the space-charge forces on the beam via either a two dimensional routine which calculates the forces on a grid, or a three-dimensional point-to-point calculation. The code uses time as the independent variable, which allows it to correctly model the effects of space charge and external forces, especially at the region near photocathode, where the beam is accelerated from non-relativistic to relativistic energy very quickly. In keeping with this concern to accurately model the dynamics of the beam, PARMELA also stores the values of the electromagnetic fields on a grid, and allows the user to input these field values computed by the codes SUPERFISH and POISSON.

PARMELA optionally uses Green's functions to calculate the space charge effects in the beam. This code keeps track of the good particles in the space charge calculations. There are options to adjust the bunch meshing for the space charge calculations and this meshing can be redefined for a given energy gain. Hence, in spite of an increase in bunch length and transverse size, the mesh fully covers the bunch over the full transport of the beam pulse. For our studies we used 20 radial grids and 400 longitudinal grids for pulse meshing and this meshing was redefined for every 10% increase in the relativistic factor γ. PARMELA also has a post-processor called PARGRAF, which gives a graphical representation of different beam parameters along the defined portion of the beam line and is used to calculate the emittance of the beam at the end of each element of the beam line. PARGRAF also calculates the 90% normalized RMS transverse emittance by considering 90% of the beam.

4.6.2 Variation in Beam Energy and Normalized Emittance with Laser Injection Phase

Electron beam energy ($\gamma\ m_0c^2$) from the photocathode RF gun is an important beam parameter as the space charge forces dominate in the non-relativistic regime near the photocathode and cause increase in the normalized emittance of the beam. To compensate the emittance growth due to space charge the design of the emittance compensation solenoid depends upon γ of the beam. As the beam is non-relativistic the synchronization of electrons with RF is crucial and affects the beam parameters. The variation in the beam energy and normalized RMS emittance with the laser injection phase with respect to RF field, for an average accelerating gradient of 60 MV/m (peak field of 150 MV/m), is shown in Fig. 4.14. The emittance is minimum for a laser injection phase of 59° with respect to the zero crossing of the RF field, while energy gain is maximum for 58°. However, since the differences in the beam energy and emittance for laser injection phase of 59° and 58° are very small, either phase could be chosen for operation.

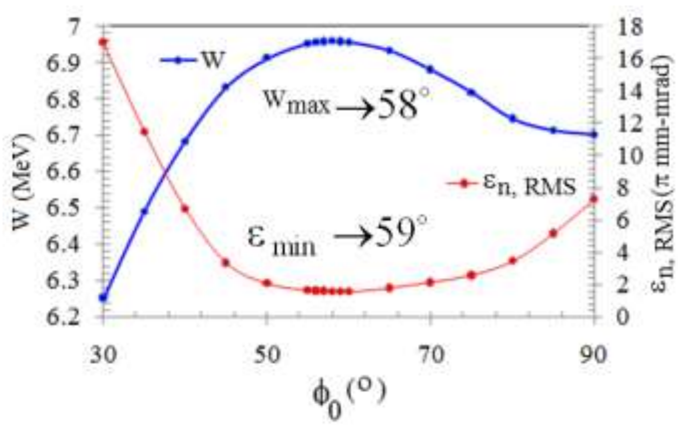

Fig. 4.14: Variation in normalized RMS emittance and beam energy with laser injection with respect to RF.

4.6.3 Normalized Emittance verses E_0 and B_z

As discussed in Chapter 3 the space charge emittance (ε_{SC}) varies as 1/E_0, where E_0 is the peak accelerating field gradient, and therefore it reduces with the increasing accelerating field gradient. But RF emittance (ε_{RF}) increases with accelerating field gradient. The space charge emittance is compensated using a solenoid magnetic field (as discussed earlier) and it becomes minimum at a particular magnetic field strength for a particular beam energy. If the solenoid field is less, then it is not capable of compensating the space-charge force and if it is more then it over-focuses the beam which further increases the emittance. Therefore to achieve the minimum emittance at an operating field gradient, a unique strength of solenoid field need to be applied. We performed PARMELA simulations by varying the peak solenoid field for different electric field gradients to achieve minimum transverse emittance as shown in Fig. 4.15. The minimum emittance for each accelerating gradient is achieved for $B_z[kG] = 0.11 E_0[MV/m]$.

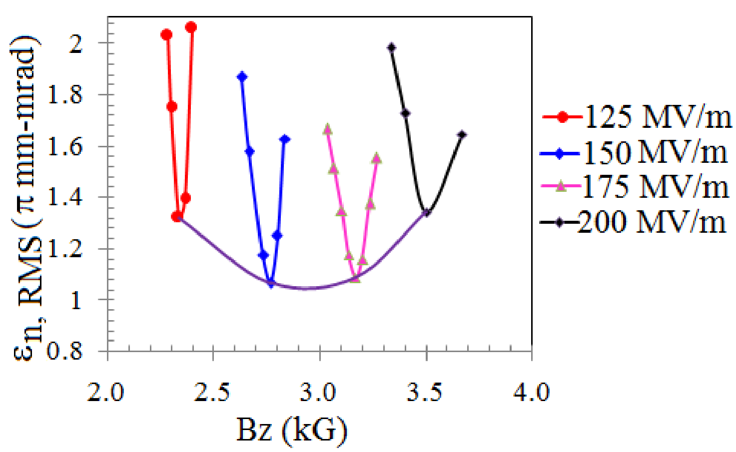

Fig. 4.15: Variation in normalized transverse emittance with solenoid magnetic field for different accelerating gradients.

4.6.4 Normalized Emittance with Field Bbalance

The ratio of peak on-axis accelerating field gradient in the half-cell to that in the full-cell, defined as the field balance (e_b), affects both the energy gain as well as the emittance of the electron beam from the photocathode RF gun. If e_b =1, which means equal field amplitude in both the cells, then emittance is minimum as the transverse defocusing kick at the exit of the half-cell gets canceled by the focusing kick at the entrance of the full-cell. When the field in the half-cell is greater than in the full-cell (e_b >1) then the defocusing kick at the exit of half-cell is greater than the focusing kick at the entrance of the full-cell, which causes an increase in the beam emittance. When the field in the full-cell is greater than in the half-cell (e_b <1), then although the focusing at the full-cell entrance is greater than the defocusing at the half-cell exit, the energy gain in the half-cell is less, which leads to growth of emittance due to space-charge. The variation in emittance with e_b is shown in Fig. 4.16

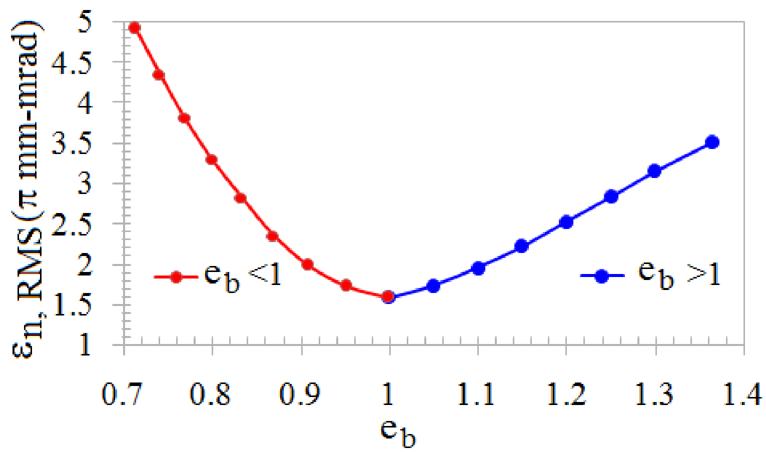

Fig. 4.16: Variation in emittance with FB for average accelerating gradient of 60 MV/m with laser injection phase ϕ=59° and solenoid magnetic field of 2.7 kG.

SUMMARY

The initial RF parameters of the gun are taken from existing scaling laws and the gun geometry is predicted using electromagnetic field solvers codes like SUPERFISH and CSTMWS. Variations in RF parameters with different geometrical dimensions are studied to determine the mechanical tolerances for fabrication. Thermal issues are studied and cooling channels are designed using ANSYS to maintain the RF parameters within desired values during high power RF operation. Beam dynamics studies are carried out using beam dynamics code PARMELA to determine the operating parameters of the gun, *viz.* peak accelerating field, field balance (e_b), solenoid field and laser injection phase. To minimize the emittance with maximum energy gain the laser should be injected at 58^0 -59^0 of accelerating field and e_b should be ~1. The solenoid field needs to be adjusted with the accelerating field gradient to minimize the emittance.

CHAPTER 5

PHOTOCATHODE RF GUN DEVELOPMENT

PROTOTYPING AND TUNING

INTRODUCTION

As discussed in previous chapters, for efficient operation and to achieve the desired beam quality from the photocathode RF gun, it should be built to resonate at 2856 MHz with field balance (e_b) and waveguide to gun coupling coefficient (β) close to unity for the π-mode. To achieve these RF parameters the structure is designed using electromagnetic field solver codes as discussed in the previous chapter. Although in RF design structure dimensions can be fine tuned to any extent to achieve the desired set of RF parameters, in reality, a structure can only be fabricated within certain geometrical tolerances that depend upon the machining capabilities, and therefore the dimensions of the final structure can have any value within the prescribed tolerance limits. These deviations in structure dimensions from the design values, due to finite tolerances, result in a deviation in the RF parameters of the photocathode RF gun from their design values. As the variation in geometrical dimensions due to fabrication tolerances are random in nature they cannot be predicted in advance, therefore the variation in RF parameters is also random which need to be corrected after machining. Along with the machining errors, the accuracy of electromagnetic codes with available computational resources may also cause deviation in RF parameters. Therefore, before proceeding for fabrication of the final structure, it is essential to develop multiple prototypes to study the agreement between simulations and experimental results, and to establish a tuning procedure to achieve the desired set of RF parameters.

In order to allow for tuning, the gun cells are fabricated with dimensions smaller than those predicted by electromagnetic simulations and the RF parameters are tuned to the desired values by employing an iterative cut and measure technique, where machining cuts are taken on the Inner Diameter (ID) of the cells and on the RF coupling slot. After each machining cut, RF parameters of the gun are measured using a Vector Network Analyzer (VNA) and depending on the convergence of the particular RF parameter towards the desired value, the next cut is taken either on the cell ID, or on the RF coupling slot, or on both, and this procedure is continued till the desired RF parameters are achieved.

In principle, the photocathode RF gun can be tuned by employing this cut and measure technique; however it is difficult and time consuming as multiple cuts of very small steps have to be taken and the RF parameters need to be measured every time. On the other hand, if cuts are taken in bigger steps then there is a chance of taking too large a cut, rendering the cell useless. The strong inter-dependence of f_π, β_π, and e_b makes it further difficult to tune the structures by this method. An understanding of this inter-dependence of f_π, β_π, and e_b, and their dependence on independent cell RF parameters can simplify the tuning procedure by enabling one to predict the values to which the RF parameters of independent cells should be tuned, in order to achieve the desired RF parameters for the coupled structure.

The dependence of the π-mode RF parameters on independent-cell RF parameters of a coupled cavity structure and of a photocathode RF gun have been studied by Schriber and

Palmer respectively [17, 68]. Schriber has analyzed a coupled cavity structure operating in the π mode, including the effect of errors in independent cell frequencies and inter-cell coupling constants, to determine f_π and e_b for the coupled structure [68] while Palmer has studied the dependence of coupled mode frequencies of a 1.6 cell photocathode gun on the frequency of the independent cells, and the dependence of field balance on the coupled mode separation (f_π-f_0) of the gun, using an equivalent LC-circuit model to represent the gun [17]. These analyses help in tuning RF accelerating structures to the desired operational mode frequency with a desired field balance. However, both of these analyses do not address the dependence of β_π on these parameters, making it difficult to simultaneously tune the structures for the desired β_π.

Gao has given a scaling law that predicts the dimensions of the RF coupling slot needed to obtain the desired β_π for a single RF cavity coupled to a waveguide [38]. However, this analysis fails when employed for a coupled cavity system where power is fed into one cell through a waveguide, while fields are set up in other cells on account of the inter-cell coupling as the case of the photocathode RF gun.

An analysis to predict the independent-cell RF parameters required to achieve the desired RF parameters for the coupled-mode of a coupled cavity RF structure has been developed using an equivalent LCR circuit analogy that includes both the inter-cell coupling as well as the waveguide-to-cavity coupling. This analysis is able to predict the inter-dependence of the coupled mode parameters of the photocathode RF gun, *viz.* f_π, e_b, β_π, and their dependence upon the independent-cell RF parameters, *viz.* f_h, f_f and β_f. Using this analysis a two-step tuning procedure has been established by predicting the required independent-cell RF parameters to obtain the desired set of π-mode parameters of the photocathode RF gun.

For completeness, a general LCR equivalent of an RF cavity and of a coupled cavity system is described in Section 5.1. As a specific case, a 1.6 cell photocathode RF gun is analyzed in Section 5.2, where circuit equations are solved to obtain the inter-dependence of the coupled-mode parameters and their dependence on the independent-cell RF parameters. In Section 5.3 a two-step tuning procedure is developed based on the LCR circuit analysis and experimental results validating the procedure are presented.

5.1 LCR EQUIVALENT CIRCUIT MODEL OF A RF CAVITY AND FOR COUPLED CAVITY SYSTEM

An RF cavity is an oscillator with loss due to finite resistivity of the cavity material. It can be represented by an LCR resonant circuit [35], where L and C are the equivalent inductance and capacitance of the cavity and R is its shunt impedance as shown in Fig. 5.1. The amplitude of current in the equivalent circuit gives the amplitude of the on-axis electric field in the cavity [68]. The values of L, C and R can be derived from experimentally measurable parameters, *viz.* resonant frequency (*f*), quality factor (Q), and characteristic impedance (R/Q), using the expressions $f = \omega/2\pi = 1/2\pi\sqrt{LC}$ and $Q = \omega L/R$. The coupling of a cavity to a generator (power source), or to another cavity, is represented by a transformer with the coupling strength determined by its turns ratio or mutual inductance.

Using this analogy, the LCR equivalent circuit representation of a system of N coupled cells (or cavities), including the coupling of the RF source to the first cell through a waveguide, is shown in Fig. 5.2, where the first circuit on the left, labeled ‘G’, refers to the generator (in this case the waveguide and the RF source), and circuits 1 to N refer to the N coupled cells.

Quantities with subscript ‘g’ refer to the generator circuit while those with subscripts n (= 1 - N) refer to the n^th cavity, and M_{ij} refers to the mutual inductance between the i^{th} and j^{th} circuits.

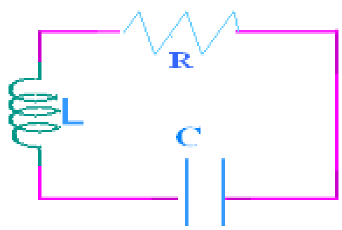

Fig.5.1: LCR equivalent circuit of a RF cavity.

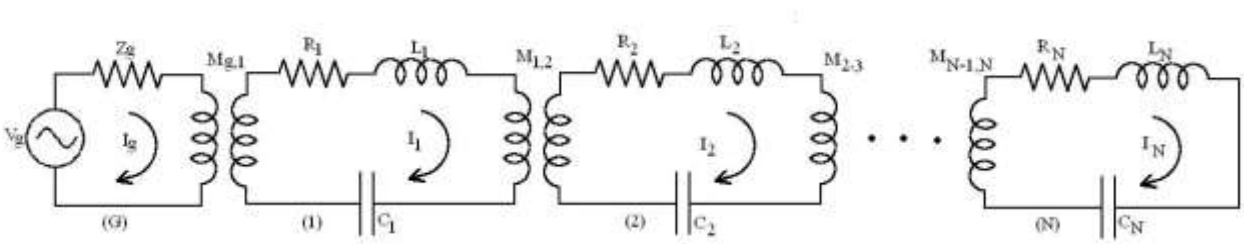

Fig.5.2: LCR equivalent of N coupled cavities with RF source.

Applying Kirchoff’s law to the n^th cell, we get

$$I_{n-1}Z^M_{n-1,n} + I_n Z_n + I_{n+1}Z^M_{n,n+1} = 0. \tag{5.1}$$

Here, I_n is the current in the n^th circuit,

$$Z_n = R_n + j(\omega L_n - \frac{1}{\omega C_n}) = R_n[1 + j\frac{Q_n}{\omega\omega_n}(\omega^2 - \omega_n^2)],$$

$$Z^M_{i,j} = j\omega M_{ij} = j\omega k_{ij}\sqrt{L_i L_j} = j\omega k_{ij}\sqrt{\frac{Q_i R_i}{\omega_i}}\sqrt{\frac{Q_j R_j}{\omega_j}}, i = n, j = i \pm 1.$$

Q_n and R_n are the quality factor and shunt impedance respectively, $\omega_n = 2\pi f_n$ where f_n is the resonant frequency of the *independent* n^{th} cell, and $k_{ij} = M_{ij} / \sqrt{L_i L_j}$ is the inter-cell coupling coefficient between the i^{th} and j^{th} cells. Note that ω is the frequency of the coupled mode and is different from ω_n.

Similarly, by applying Kirchoff's Law to the other cells, we get a set of N equations

$$
\begin{aligned}
& I_g Z_g + I_1 Z_{g,1}^M = V_g, \\
& I_g Z_{g,1}^M + I_1 Z_1 + I_2 Z_{g,2}^M = 0, \\
& \vdots \\
& I_{n-1} Z_{n-1,n}^M + I_n Z_n + I_{n+1} Z_{n,n+1}^M = 0, \\
& \vdots \\
& I_{N-2} Z_{N-2,N-1}^M + I_{N-1} Z_{N-1} + I_N Z_{N-1,N}^M = 0, \\
& I_{N-1} Z_{N-1,N}^M + I_N Z_N = 0.
\end{aligned}
\tag{5.2}
$$

These equations can be used to study an accelerating structure with any number of cells.

5.2 LCR EQUIVALENT CIRCUIT ANALYSIS OF 1.6 CELL PHOTOCATHODE RF GUN

The cross section and LCR equivalent circuit of a 1.6 cell photocathode RF gun are shown in Fig. 5.3. For this gun, N =2 and we obtain a set of three equations which can be solved analytically to study the dependence of operating mode frequency, e_b and β on the independent cell properties,

$$I_h Z_h + I_f Z_{f,h}^M = 0, \tag{5.3a}$$

$$I_g Z_{g,f}^M + I_f Z_f + I_h Z_{f,h}^M = 0, \tag{5.3b}$$

$$I_g Z_g + I_f Z_{g,f}^M = V_g, \tag{5.3c}$$

where subscripts *f* and *h* refer to the full- and half-cells respectively. Solving Eqs. (5.3a) and (5.3b), assuming each cell is loss-less with very high Q [17], and neglecting the contribution of the generator circuit to determine the coupled-mode frequencies, we get

$$\left(\omega^2 - \omega_f^2\right)\left(\omega^2 - \omega_h^2\right) = \omega^4 k_{fh}^2. \tag{5.4}$$

The positive roots of Eq. (5.4) give the coupled mode frequencies ω_0 and ω_π as

$$\omega_0 = \left[\frac{(\omega_f^2 + \omega_h^2)}{2(1-k_{fh}^2)} - \frac{\sqrt{(\omega_f^2 + \omega_h^2)^2 - 4\omega_f^2\omega_h^2(1-k_{fh}^2)}}{2(1-k_{fh}^2)}\right]^{1/2}, \tag{5.5a}$$

$$\omega_\pi = \left[\frac{(\omega_f^2 + \omega_h^2)}{2(1-k_{fh}^2)} + \frac{\sqrt{(\omega_f^2 + \omega_h^2)^2 - 4\omega_f^2\omega_h^2(1-k_{fh}^2)}}{2(1-k_{fh}^2)}\right]^{1/2}. \tag{5.5b}$$

The field balance, e_b, is given by

$$e_b = \frac{|I_f|}{|I_h|} = \left| -\frac{Z_h}{Z_{f,h}^M} \right| = \frac{R_h\left[1 + \frac{Q_h^2}{\omega^2 \times \omega_h^2}(\omega^2 - \omega_h^2)^2\right]^{1/2}}{\omega k_{fh}\sqrt{\frac{Q_h R_h}{\omega_h}}\sqrt{\frac{Q_f R_f}{\omega_f}}}. \tag{5.6}$$

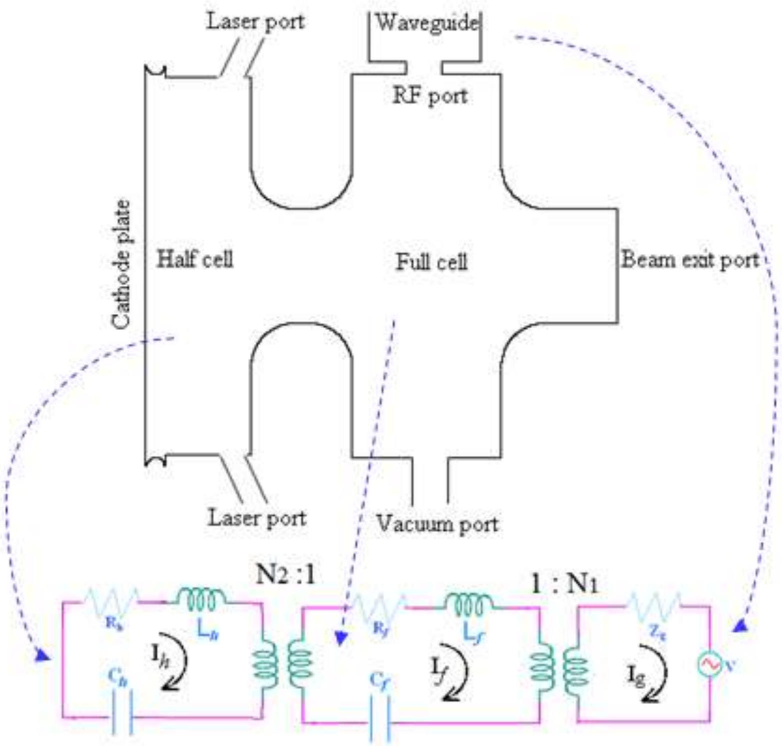

Fig. 5.3: Cross-section and LCR equivalent circuit of 1.6 cell BNL/SLAC/UCLA type photocathode RF gun.

The dependence of the mode frequencies and field balance on the independent cell parameters is evident from Eqs. (5.5) and (5.6). These equations can be used to predict the frequencies to which the independent cells should be tuned, in order to simultaneously obtain the desired coupled-mode frequency f_{π}, as well as a field-balance e_b close to unity.

To study the dependence of β on e_b, we solve the set of Eqs. (5.3) simultaneously to get

$$I_g Z_g + I_g Z_{eff} = V_g, \tag{5.7}$$

where $Z_{eff} = -(Z^M_{g,f})^2 \big/ [Z_f - (Z^M_{f,h})^2 \big/ Z_h]$.

Equation (5.7) represents Kirchoff's Law for the circuit shown in Fig. 5.4, which is the equivalent circuit of a photocathode RF gun coupled to a generator with the impedance of the gun transferred towards the generator side. Here Z_g is the characteristic impedance of the waveguide and Z_{eff} is the effective impedance of the half- and full-cells coupled together, as seen by the generator.

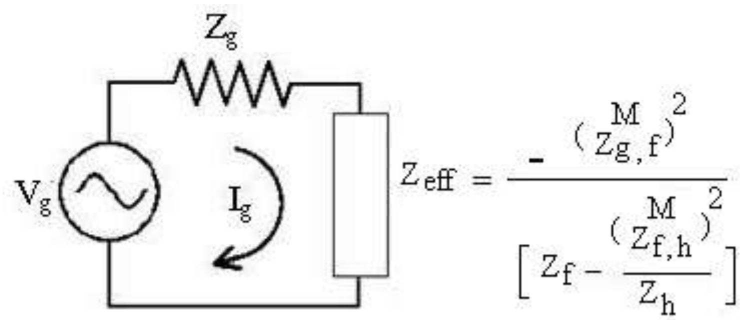

Fig.5.4: Equivalent circuit model of a photocathode gun for calculation of β.

The waveguide-to-gun coupling coefficient β is defined as

$$\beta = \frac{P_{ext}}{P_c} = \frac{\mathrm{Re}(Z_{eff})}{Z_g}, \tag{5.8}$$

where P_c is the power dissipated in the gun and P_{ext} is the power dissipated in the external load (waveguide) [39, 69]. Using Eq. (5.7), we get

$$\beta = \mathrm{Re}\left[(Z_{g,f}^{M})^2 \Big/ \left(Z_f - \frac{(Z_{f,h}^{M})^2}{Z_h} \right) Z_g \right]. \tag{5.9}$$

The second term in the denominator of Eq. (5.9) shows the dependence of β on e_b.

Using Eq. (5.6) and the expression for $Z_{g,f}^{M}$ in Eq. (5.9), we get

$$\beta = \frac{\omega^2 M_{gf}^2}{\mathrm{Re}[Z_f + \frac{\overline{Z}_h}{e_b^2}] Z_g}, \tag{5.10}$$

where $\overline{Z}_h$ is the complex conjugate of Z_h. Equation (5.10) relates β to the experimentally measurable quantities ω, Z_f, e_b, Z_h and Z_g, for the desired mode of operation. The value of M_{gf}, which is not directly measurable, can be determined using Eq. (5.10) for the independent full-cell by detuning the half-cell, resulting in zero coupling between the half- and full-cells. In this case, $Z_f = R_f$ at $\omega = \omega_f$, and $Z_{f,h}^{M} = 0$. Equation (5.10) now reduces to $\beta_f = \omega^2 M_{gf}^2 \big/ R_f Z_g$, which is the waveguide to independent full-cell coupling coefficient (β_f). Using this in Eq. (5.10) we get

$$\beta = \frac{(\omega/\omega_f)^2 \beta_f R_f}{\mathrm{Re}[Z_f + \frac{\overline{Z}_h}{e_b^2}]}. \tag{5.11}$$

Substituting the expressions for $\omega_{\pi,0}$ from Eq. (5.5) into Eq. (5.11) gives the dependence of β on e_b for the desired mode.

Equations (5.5b), (5.6) and (5.11) give the dependence of the coupled response of the gun, *i.e.* the dependence of frequency, e_b and β for the π-mode, on parameters of the independent full-and half-cells which are easily measurable. While the resonant frequency of the independent half- and full-cells can be fine-tuned by taking small machining cuts on the cell IDs, this causes a very small change in their Q and R, as is evident from standard analytical expressions for the dependence of Q and R on the radius of pillbox cavities. The coupled-mode properties can therefore essentially be fine-tuned by tuning the resonant frequencies of the independent cells.

It must be noted here that the Q and R of the half-cell are not the same as that of the full-cell because of their different lengths and port openings. Ignoring the port openings and considering ideal pillbox type structures, Q and R are given by [69],

$$Q = \frac{2.405\mu_0 c}{2\rho_s[1+(R_c/L)]}, \tag{5.12}$$

$$R = \frac{Z_0^2}{\pi\rho_s J_1^2(2.405)} \frac{L}{R_c} \frac{T^2}{[1+(R_c/L)]}, \tag{5.13}$$

here T is the transit time factor, $R_c = 2.405c/2\pi f$ is the radius and L is the length of the pillbox. For a 1.6 cell gun, $L_f = \lambda/2$ and $L_h = 0.6(\lambda/2)$, and Eqs. (5.12) and (5.13) give $Q_h/Q_f \sim 0.8$ and $R_h/R_f \sim 0.9$. Therefore, to a first approximation, we can assume that both the half- and full-cells have the same value of Q and R. Then Eqs. (5.5) and (5.6) show that f_π = 2856 MHz with e_b unity when $f_f = f_h = f_{00}$ = 2854.54 MHz. In this case, Eqs. (5.5b), (5.6) and (5.11) reduce to

$$f_\pi = \frac{f_{00}}{\sqrt{1-k_{fh}}}, \; e_b = 1, \; \beta_\pi = \frac{\beta_f}{2}. \tag{5.14}$$

Equation 5.14 gives a simple way of obtaining the right f_π, e_b and β for the coupled structure, and is therefore very useful while tuning the gun. Of course, Eq. (5.14) assumes that Q & R are equal for the two cells – an approximation that is good only to within 10-20%. A more accurate method is to actually measure the values of Q and R for the independent half- and full-cells and to use these values in Eq.(5.5b), (5.6), and (5.11) to predict the values of the independent cell frequencies and β_f that are needed in order to obtain f_π = 2856 MHz with e_b and β_π both equal to 1. In the discussion of the experimental results below, we compare those results with both the analytical models.

5.3 TUNING AND RF MEASUREMENTS ON PROTOTYPES: TWO STEP TUNING

Based upon LCR circuit analysis of the photocathode RF gun it is clear that tuning the photocathode RF gun involves fixing three parameters: (i) the π-mode frequency f_π to 2856 MHz; (ii) the field balance e_b to unity; and (iii) the coupling factor β_π also to unity (though occasionally a higher value may be preferred in order to reduce the fill-time). The earlier analysis shows that once the value of the coupling k_{fh} is determined experimentally, Eqs. (5.5) and (5.6) can be used to relate the desired RF parameters of the complete gun, to those of the individual cells.

The first task is therefore to determine the values of the independent cell parameters required to tune the gun to the desired values of f_π, β_π, and e_b. This can be done as follows:

(1) Measure the resonant frequency (f) and quality factor (Q) of the independent half- and full-cells, and the waveguide to independent full-cell coupling coefficient β_f.

(2) Assemble the half- and full-cells together and measure the π-mode frequency and field balance. Using these values in Eq. (5.6), the value of k_{fh} can be determined. Since no machining cut is

taken on the inter-cell coupling iris during the tuning process, k_{fh} is unchanged during the tuning process.

(3) Assuming a constant f_h, Eqs. (5.5b) and (5.6) are used to scan the variation of resonant frequency and e_b respectively for the π mode with f_f. The value of e_b is noted at the desired value of f_π. This can be done by writing a small programme; we have done this in MATLAB.

(4) If e_b at the desired f_π differs from the target value, the value of f_h is changed and step 3 is repeated until the desired value of e_b is obtained.

(5) Knowing the required values of f_f and f_h for the desired f_π and e_b, Eq. (5.11) is used to determine the value of β_π/β_f, using which the required values of β_f can be determined for any target value of β_π.

With all required independent cell parameters predicted, a two-step procedure can now be followed for actual tuning of the gun:

Step 1: Tune the half-cell frequency to the target value.

Step 2: Tune the full-cell frequency to the target value while simultaneously obtaining the required β_f.

When the independent cells are now coupled, the analysis of the earlier section predicts that the coupled gun will have the desired RF properties: f_π = 2856 MHz, e_b = 1 and β_π = 1.

5.3.1 Measurement on the Independent Cells

To confirm the predictions of the LCR circuit analysis for the photocathode RF gun, two true-to-scale prototypes were developed, one made of aluminum (AGUN) and the other of ETP copper (ETPGUN). Both prototypes were fabricated with inner diameters (ID) of the half- and full-cells slightly undersized, as compared to dimensions predicted by simulations [19, 70], for flexibility in tuning individual cell frequencies. The length of the waveguide to cavity coupling slot was also initially smaller than the size required for critical coupling. These prototypes were fabricated with relaxed geometric and dimensional tolerances to reduce machining costs.

Since tuning of the gun has to be done prior to joining of the half- and full-cells by brazing, a fixture was designed to hold the gun assembly, including the helicoflex seal that is proposed to be used for vacuum sealing at that cathode plate – half-cell joint of the gun. Figure 5.5 shows a picture of the experimental setup used to measure the independent-cell parameters. As is well known, the two cells of a photocathode RF gun exhibit independent behaviour when their independent resonant frequencies are wide apart such that their 'Q' curves do not overlap. This has been exploited to measure the independent cell parameters. A plunger was inserted into the half-cell through one of the laser ports to move its independent cell frequency away from that of the full-cell, and the independent full-cell RF parameters Q_f and R_f were measured in this condition. Similarly, RF parameters Q_h and R_h of the independent half-cell were measured by inserting a plunger through one of the tuner ports to detune the full-cell. The detuning of one of the cells is ensured by measuring the variation in the on-axis electric field by performing a bead-pull measurement. Variation in the on-axis electric field in the half-cell while the full-cell is detuned is shown in Fig. 5.6; similarly variation in the on-axis electric field in the full-cell while the half-cell is detuned is shown in Fig. 5.7.

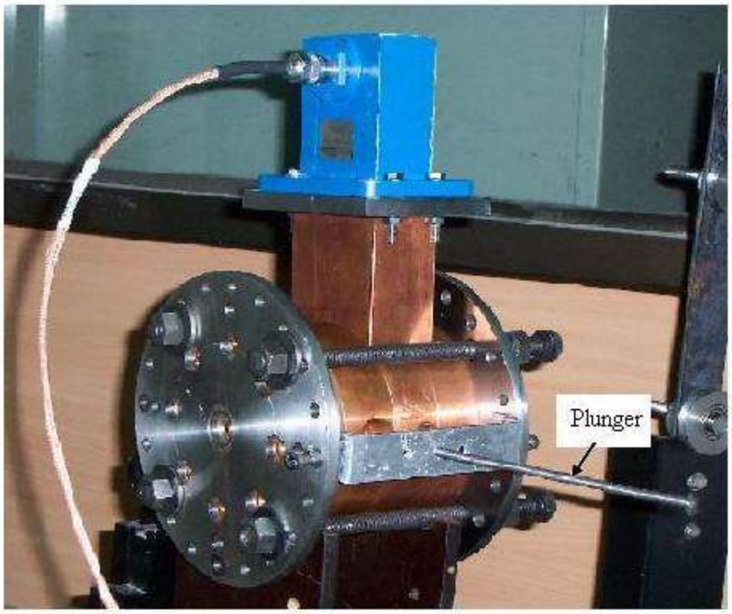

Fig.5.5: Experimental setup for measurement of RF parameters of independent full-cell. A plunger is inserted through the laser port to detune the half-cell.

Table 5.1: Quality factor and shunt impedance of independent full- and half-cells for AGUN and ETPGUN.

Parameters	Q_h	Q_f	R_h ((MΩ)	R_f(MΩ)
AGUN	4618	4186	0.76	1.06
ETPGUN	9500	7544	1.79	2.17

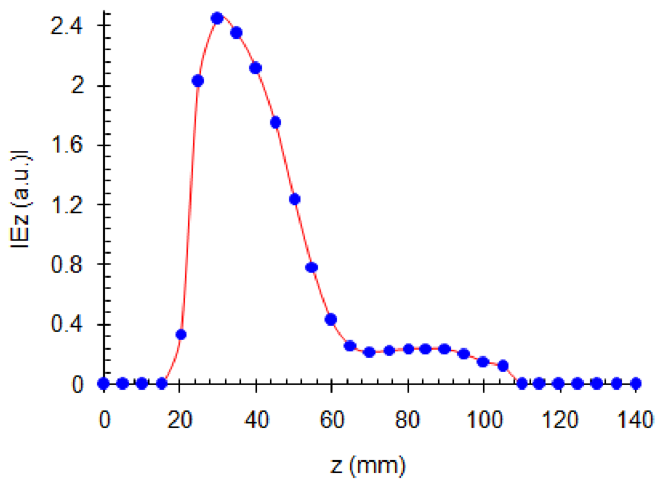

Fig.5.6: Variation in the on-axis electric field in the half-cell while the full-cell is detuned.

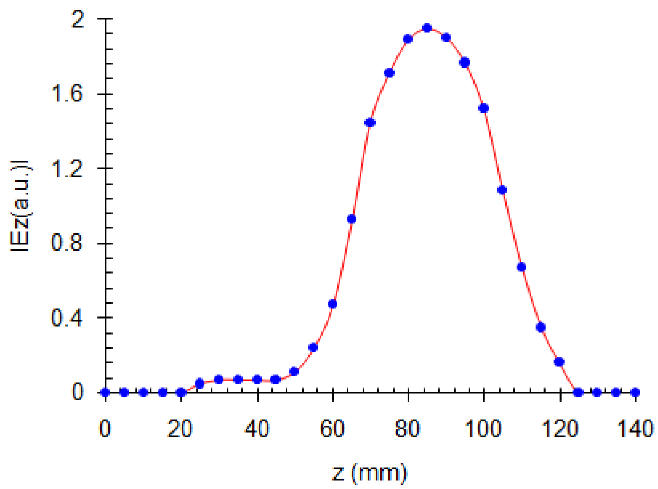

Fig.5.7: Variation in the on-axis electric field in the full-cell while the half-cell is detuned.

The measured values of Q and R of the independent cells for both prototypes are shown in Table 5.1. For these measured values Q_h/Q_f = 1.1 for AGUN and 1.25 for ETPGUN, and R_h/R_f =

0.71 for AGUN and 0.82 for ETPGUN. Thus, for both guns, the measured Qs and Rs of the two cells vary by 10–30%, which compares well with the analytical values of 10–20% calculated earlier using Eqs. (5.12) and (5.13). The machined full-cell has five ports while the machined half-cell has two ports. The larger number of ports in the full-cell causes a greater reduction in its Q value as compared to that of the half-cell. Hence, the measured Q_h/Q_f is greater than unity while the value obtained from analytical calculations is less than unity.

5.3.2 Simulated Tuning of AGUN

For AGUN, the analysis of the previous section predicts that for a π-mode frequency of 2856 MHz with e_b and β equal to unity, the required values of the independent cell parameters are: f_f = 2854.8 MHz, f_h = 2854.5 MHz and β_f = 1.69.

Before taking machining cuts on the independent cells to change their frequencies, the tuning procedure was simulated by employing plungers to modify the independent cell frequencies. As is well known, the full- and half-cells are uncoupled when their resonant frequencies are wide apart. Since power is fed only into the full-cell, the field in the full-cell is high while the field in the half-cell is almost zero, resulting in a very high value of e_b. The value of β at this point is just β_f. As the independent cell frequencies come closer, the two cells start showing coupled behaviour and the measured values of e_b and β at this stage are those of the coupled mode.

To simulate Step 1 of the two-step tuning procedure, a plunger (plunger #1) was inserted into the full-cell through one of the tuning ports to shift its frequency far from that of the independent half-cell. Using another plunger (plunger #2) inserted into the half-cell through a laser port, the half-cell frequency was adjusted to the predicted value of 2854.5 MHz.

For simulating Step 2, the half-cell was now detuned using another plunger (plunger #3) inserted through the other laser port without disturbing plunger #2. The full-cell frequency was now tuned to the required value of 2854.8 MHz by inserting another plunger (plunger #4) through another tuning port and adjusting the position of plungers #1 and #4 in the full-cell.

Since no machining cut was taken on the RF coupling slot, β_f could not simultaneously be modified from its small initial value of 0.04 to the targeted valued of 1.69. However, from Eq. (5.11) we can see that β/β_f is independent of the RF slot dimensions. Therefore, it is adequate to compare the measured values of β/β_f with the prediction in order to validate our theory.

At this stage, when plunger #3 was removed from the half-cell, the desired frequency for the π-mode was obtained with e_b = 1.02 and β/β_f = 0.60, which agrees well with predictions. The small deviations may be due to the perturbations in Q and R caused by the plungers. A comparison of results obtained experimentally with those predicted by our circuit analysis is given in Table 5.2. Columns 2 and 4 show the analytically calculated values of f_f, f_h and β/β_f required to obtain f_π = 2856 MHz, e_b = 1 and β = 1 for AGUN for the two cases: (i) assuming equal values of Q and R for the two cells, and (ii) using measured values of Q and R of the half- and full-cells, respectively. Columns 3 & 5 show the measured values on AGUN, where the plungers were adjusted to tune f_f and f_h to the values predicted by the LCR analysis, and the cells were then coupled together by removing plunger #3 and the values of f_π, e_b and β/β_f measured. While there is good agreement between the measured and predicted values of f_π and e_b for both cases, the agreement in β/β_f is good only in Case 2. Eq. (5.11) shows that β/β_f varies as $1/(Z_f + \overline{Z}_h / e_b^2)$, and since e_b = 0.8 in Case 1, it leads to a rather large deviation in the value of β/β_f.

Table 5.2: A comparison of experimental results for AGUN, with predictions of LCR circuit analysis.

Parameters	Predicted by LCR circuit analysis with $Q_h = Q_f$ and $R_h = R_f$	Measured	Predicted by LCR circuit analysis, using measured Q_h, Q_f & R_h, R_f.	Measured
f_π (MHz)	2856	2855.79	2856	2856.35
e_b	1.00	0.8	1.00	1.02
β / β_f	0.5	0.28	0.59	0.60
f_f (MHz)	2854.54	2854.54	2854.8	2854.8
f_h (MHz)	2854.54	2854.54	2854.5	2854.5
$(f_\pi - f_0)$ (MHz)	2.94	2.7	2.96	3.1

This simulation was further extended to study the evolution of frequency, e_b and β for the coupled modes as a function of change in the independent-cell frequencies. The variation in the '0' and 'π' mode frequencies with the resonant frequency of the independent full-cell, for a fixed resonant frequency of the independent half-cell, agrees well with results predicted by our circuit analysis using the measured values of Q and R for the independent full- and half-cells, as shown in Fig. 5.8 The variation of e_b with the separation between independent full- and half-cell frequencies is shown in Fig. 5.9 where a value of e_b =1 is obtained for $f_f - f_h$ = 300 kHz, which is also in very good agreement with predictions from the circuit analysis.

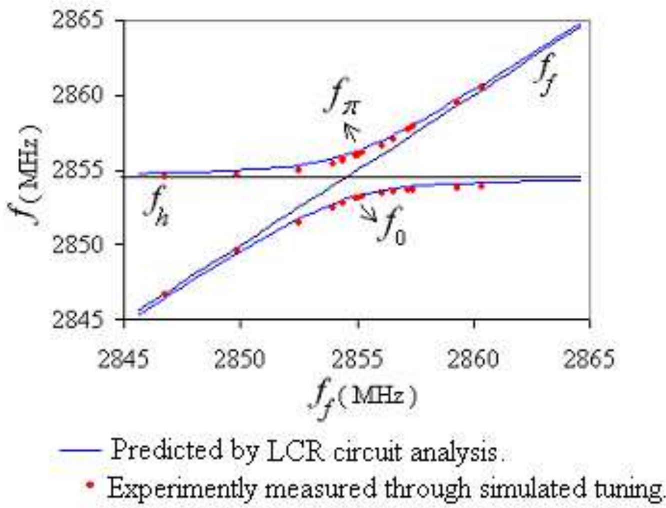

Fig. 5.8 : Variation in f_0 and f_π with independent full-cell frequency (f_f) for a constant half-cell frequency (f_h) for AGUN.

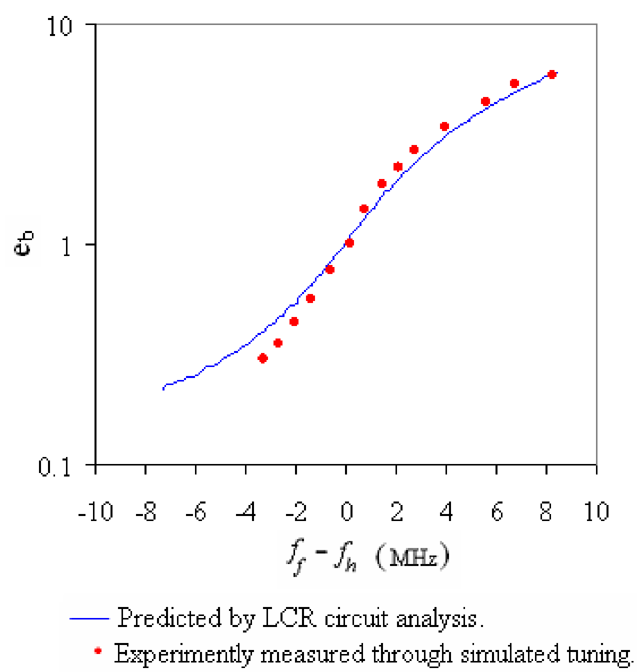

Fig. 5.9: Variation in e_b with (f_f-f_h) in AGUN.

Similar results have been reported earlier by Palmer [17]. However, since he has not considered the coupling of the full-cell to the waveguide, he does not study the dependence of β on e_b for the π-mode, which is an important aspect in the tuning of a photocathode gun. We have predicted this dependence using our analysis and obtained good agreement with results obtained during simulated tuning of AGUN, as shown in Fig. 5.10.

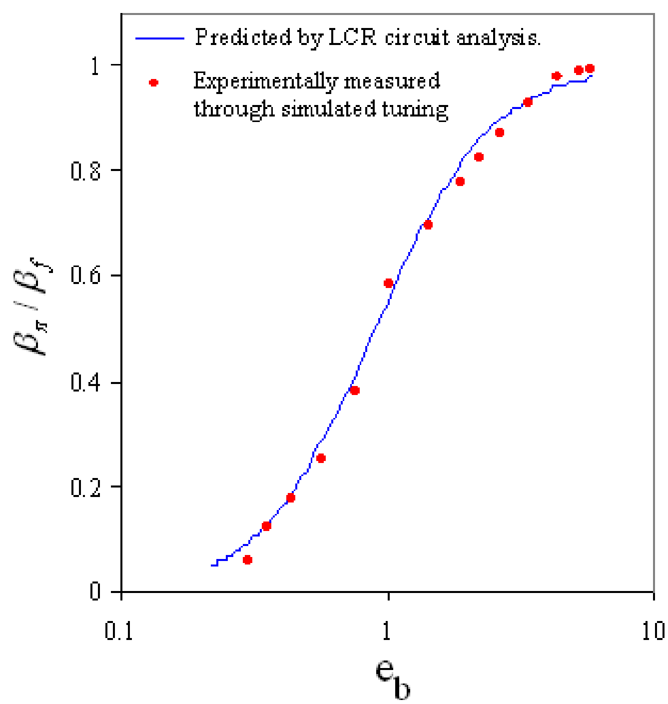

Fig. 5.10: Variation in β_π/β_f with e_b in AGUN.

5.3.3 Two-Step Tuning

With the confidence gained from simulated tuning, we proceeded to the actual tuning of AGUN. Employing the two-step procedure, AGUN was tuned by taking machining cuts on the full- and half-cells to obtain the required values for independent-cell parameters: f_f =2855.22 MHz, f_h =2854.76 MHz, β_f =1.76. When the two cells were coupled together, we obtained f_π = 2856.28 MHz with β =1.06, and e_b = 1.04.

The two-step tuning procedure was subsequently employed successfully on ETPGUN to study the repeatability of the tuning procedure. Since the Q and R for the independent cells of ETPGUN are different from those of AGUN, [c.f. Table 5.1] while the inter-cell coupling coefficient k_{fh} is the same, our analysis predicts that for a π-mode frequency of 2856 MHz with a field balance and β equal to unity, the required values of the independent-cell parameters are: f_f = 2854.6 MHz, f_h = 2854.5 MHz and β_f = 1.72.

A comparison of these experimental results with the predictions of our circuit analysis is given in Table 5.3. For both prototypes, AGUN and ETPGUN, the agreement between the circuit analysis and the measured values of the various RF parameters is excellent. The 'Predicted by LCR analysis' columns show the values of f_f, f_h and β_f that the individual cells need to be tuned to, in order to obtain f_π = 2856 MHz, e_b = 1, and β_π = 1. The 'Measured' columns are the experimental results: the cells were first tuned (by taking machining cuts on the IDs of the full-cell and half-cell, and filing the coupling slot) to the predicted values of f_f, f_h and β_f, and then coupled, and the resulting f_π, e_b and β_π were noted – these differ from the targeted values by only a few percent. From Table 5.3 it can be seen that the actual values of f_f, f_h and β_f we achieved differ slightly from the values predicted by our LCR analysis. This could contribute to the observed deviation of the coupled-cell parameters from the targeted values. To confirm this we used the *measured* values of the independent-cell parameters in our LCR circuit model to predict the coupled-cell parameters (f_π, β_π and e_b), shown in the columns marked 'Verified by LCR analysis'. It can be seen that these are now closer to the measured values.

Table 5.3: A comparison of experimental measurements with predictions of LCR circuit analysis.

Parameter	AGUN			ETPGUN		
	Predicted by LCR analysis	Measured	Verified by LCR analysis	Predicted by LCR analysis	Measured	Verified by LCR analysis
f_π (MHz)	2856	2856.28	2856.48	2856	2856.29	2856.34
e_b	1.00	1.04	1.06	1.00	1.06	1.09
β_π	1.00	1.06	1.02	1.00	1.02	1.00
β_f	1.69	1.67	1.67	1.72	1.69	1.69
f_f (MHz)	2854.8	2855.22	2855.22	2854.6	2854.97	2854.97
f_h (MHz)	2854.5	2854.75	2854.75	2854.5	2854.76	2854.76
(f_π - f_0) (MHz)	2.96	2.92	2.98	2.94	2.93	2.95
Coupling-slot length (mm)	--	25.2	--	--	23.5	--
R (MΩ)	--	1.13	--	--	2.30	--
Q_0	--	4,465	--	--	7,777	--

Figure 5.11 shows the spectrum of modes supported by ETPGUN with the π-mode at 2856.294 MHz and a mode separation of 2.93 MHz. Figure 5.12 shows the on-axis accelerating field profile in ETPGUN before and after tuning. Before tuning, the field in the full-cell is much

higher than that in the half-cell with e_b ~ 3. After tuning, the fields in the two cells are almost equal, and e_b ~ 1. Figure 5.13 shows the Smith Chart for the tuned ETPGUN structure with β_π slightly greater than unity.

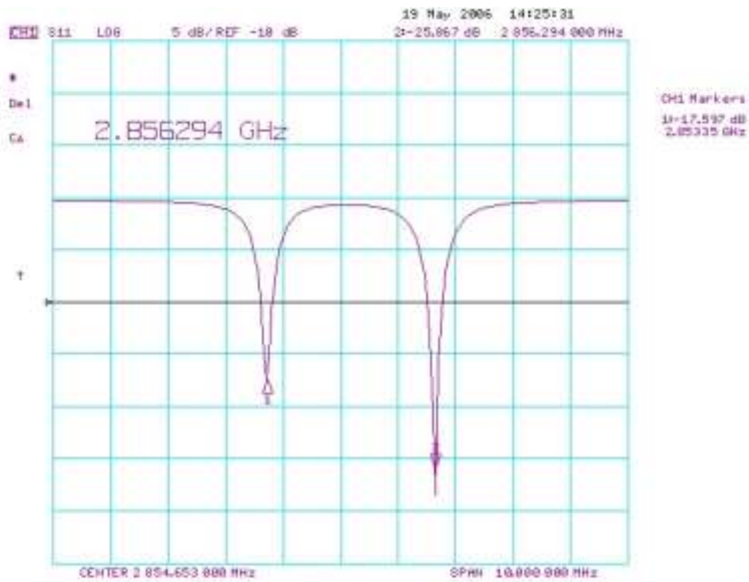

Fig. 5.11: Frequency spectrum of tuned ETPGUN.

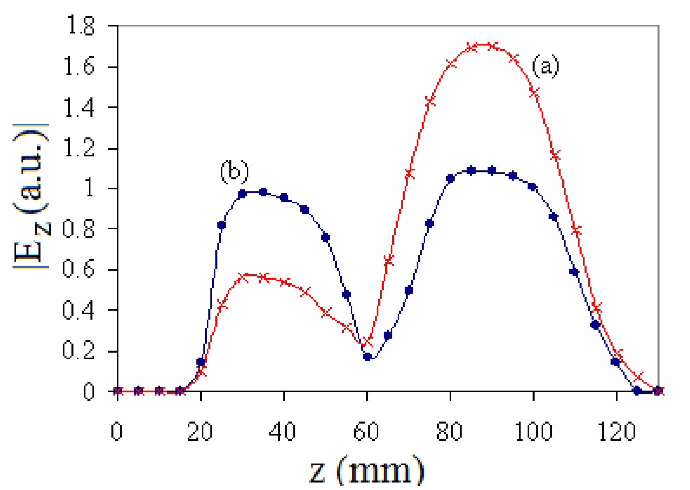

Fig. 5.12: On-axis accelerating field profile of the π-mode along the structure length in ETPGUN, (a) before tuning, (b) after tuning.

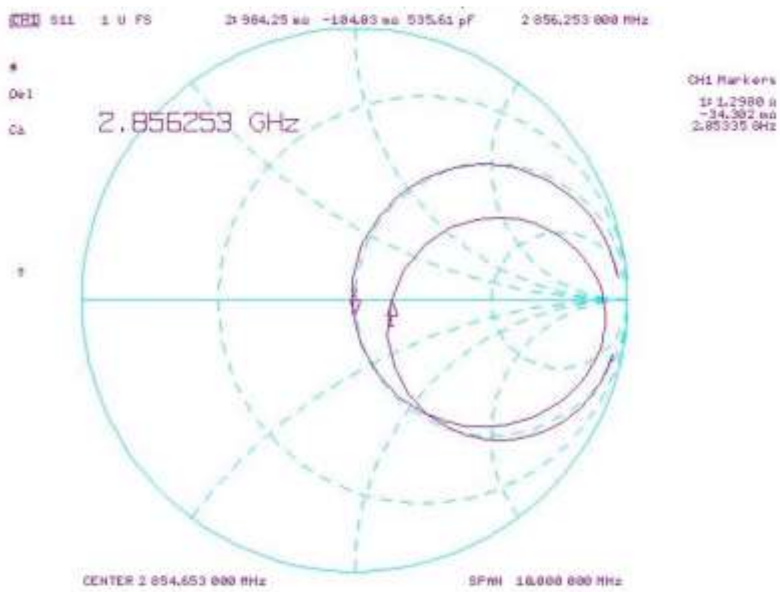

Fig. 5.13: Smith Chart for the tuned ETPGUN structure.

5.3.4 A Graphical Method of Tuning

In principle, for any gun for which $Q_{f,h}$ and $R_{f,h}$, are known, Fig. 5.9 can be used to predict the required value of f_f - f_h for any desired value of e_b, and Fig. 5.10 can be used to predict the value of β/β_f for the chosen value of e_b. With this value of β/β_f, the required value of β_f for the desired value of β can be predicted. In addition to these two parameters, tuning of a gun involves tuning f_π to the desired value. While the value of e_b depends only on the difference (f_f – f_h), f_π depends on the individual values of f_f and f_h, which cannot be extracted from Figs. 5.9 and 5.10. The three-dimensional plot shown in Fig. 5.14, which has been generated by numerically solving Eqs. (5.5a) and (5.5b), gives the required value of f_f, and therefore the value of f_h, to obtain the desired value of f_π for any given value of f_f -f_h. Thus, Figs. 5.9, 5.10 & 5.14, can together be used to tune the photocathode gun to any desired value of f_π with any desired value of e_b and β. For example, if it is desired to tune the gun for f_π = 2856 MHz with e_b = 1.2 and β = 1.5, Fig. 5.9 shows that the required f_f - f_h = 0.86 MHz, while Fig. 5.10 gives the required value of β_f = 2.25. From Fig. 5.14, f_f = 2854.9 MHz giving f_h = 2854.04 MHz.

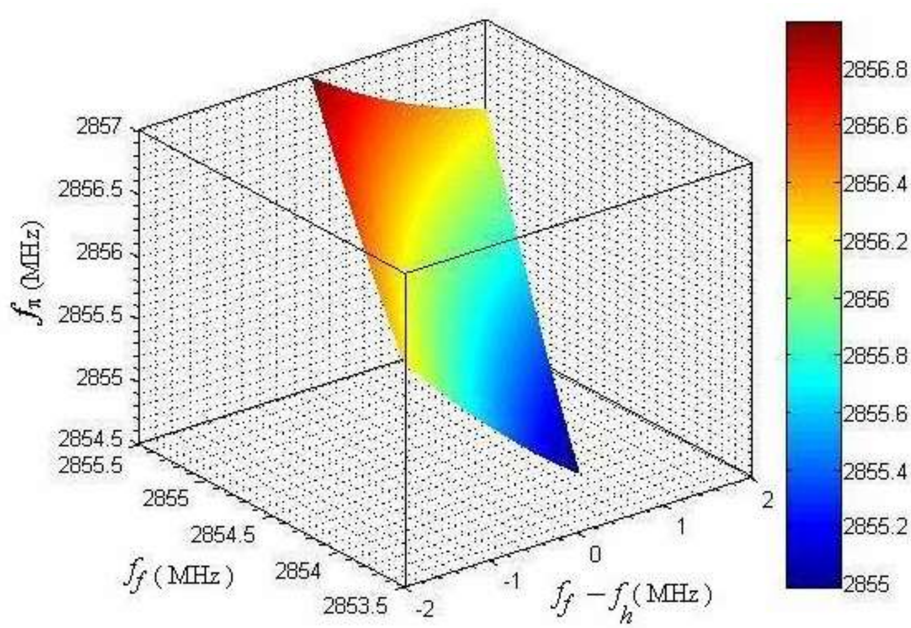

Fig. 5.14:Three-dimensional plot between f_f, f_f –f_h and f_π.

5.4 PREDICTION OF GEOMETRICAL DIMENSIONS OF PHOTOCATHODE RF GUN: ANALYTICAL METHOD

Although the two step tuning procedure discussed in the previous section simplifies the tuning of the photocathode RF gun by predicting the required independent-cell RF parameters for the desired RF parameters of the π-mode, the independent-cell RF parameters still need to be tuned by employing conventional cut-and-measure techniques for coarse tuning [71-77] and new techniques involving mechanical deformation of cavity walls for fine tuning [78-87], both of which are iterative in nature. For the half-cell only one parameter f_h needs to be tuned while for the full-cell two parameters f_f and β_f need to be tuned. Primarily, the resonant frequency of an RF cavity depends upon its radius, and the waveguide-to-cavity coupling β depends upon the length of the RF coupling slot [34, 38]. However, resonant frequency also varies with the dimensions of the RF coupling slot because the fields get modified at the location of slot. Similarly, β is also affected by the radius of the cavity because the thickness of the slot changes with radius of the cavity. Thus, the frequency and β are interdependent. For the half-cell, only its resonant frequency needs to be tuned, and this can be done by employing an iterative cut-and-measure technique as discussed in the previous section. But for the full-cell two parameters, f_f and β_f, need to be tuned together, and since they are interdependent tuning them by an iterative cut-and-measure technique is more difficult. If the variation in the independent-cell RF parameters (f_h, f_f and β_f) with the geometrical dimensions of the cells, and interdependence of f_f and β_f were known, then the requirement of tuning the independent cells could be eliminated.

In general the tuning of the gun is done before brazing when it is in air, while it is used after brazing and under vacuum. This difference in the medium and in the physical conditions, leads to a deviation in the independent-cell RF parameters, and hence in the coupled-mode RF parameters. Therefore, the effect of vacuum and brazing on the independent-cell RF parameters needs to be incorporated while tuning the gun such that after brazing and under vacuum the desired RF parameters can be achieved.

Hence, to eliminate the requirement of tuning of photocathode RF gun, the LCR circuit analysis was further extended to predict the geometrical dimensions of independent cells, *viz.* inner radius (ID) and length of RF coupling slot (L_{RF}) taking into account the effect of vacuum and brazing, to achieve the desired RF parameters of the gun under operational conditions. A scaling law that accounts for the inter-dependence between frequency of independent cells and waveguide-to-cavity coupling coefficient, as well as the effect of brazing and vacuum, has been developed to predict the geometrical dimensions of the gun. For completeness results of a parametric simulation study to understand the difficulties in tuning the independent-cell RF properties by iterative cut-and-measure technique are discussed in next section. This is followed by a discussion of the methodology for deriving a scaling law for predicting independent-cell dimensions for desired RF properties. It is effectively shown in this section that a photocathode RF gun can be tuned using a 2-D code like SUPERFISH. A comparison of results obtained from tuning of multiple copper photocathode guns with those predicted by this scaling law, and by simulations, are discussed in this Section.

5.4.1 Parametric Study: Inter-dependence of RF Parameters

In order to develop a better, more quantitative, understand the inter-dependence of f_f and β_f discussed above, and their effect on the coupled-mode parameters, a parametric study was performed using CSTMWS [64]. For example, if f_π and e_b are tuned first by tuning f_h and f_f (by choosing the appropriate values of half-cell radius R_{ch} and full-cell radius R_{cf}), and β_f is tuned later by increasing L_{RF}, it results in an increase in β_π only up to a certain value after which it starts reducing, as shown in Fig. 5.15. This counter-intuitive reduction in β_π is on account of the frequency of the full-cell (f_f) being affected by L_{RF}, which consequently affects f_π and e_b quite significantly as shown in Figs. 5.16 and 5.17, where f_π can be seen to decrease to 2854 MHz from its initial value of 2856 MHz, and e_b reduces to 0.2 from its initial value of 1.

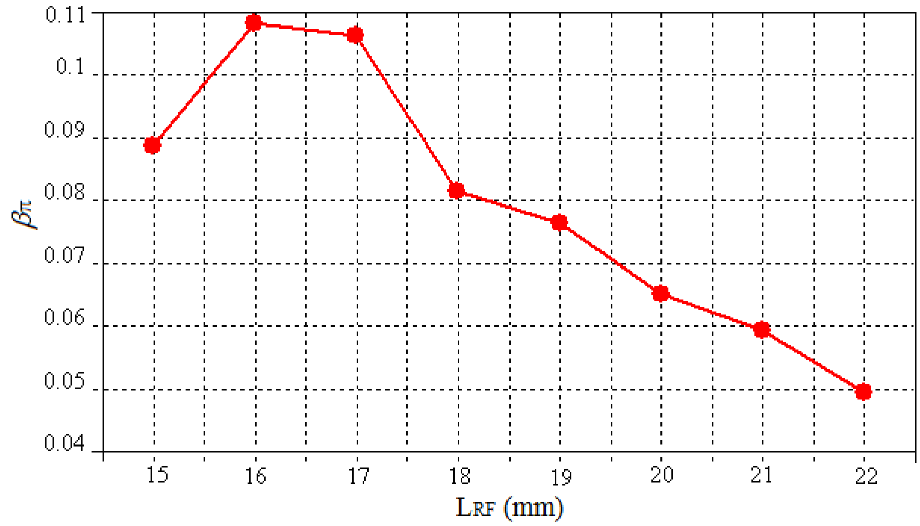

Fig 5.15: Variation in β_π with length of RF coupling slot (L_{RF}), for a constant radius of full- and half-cells.

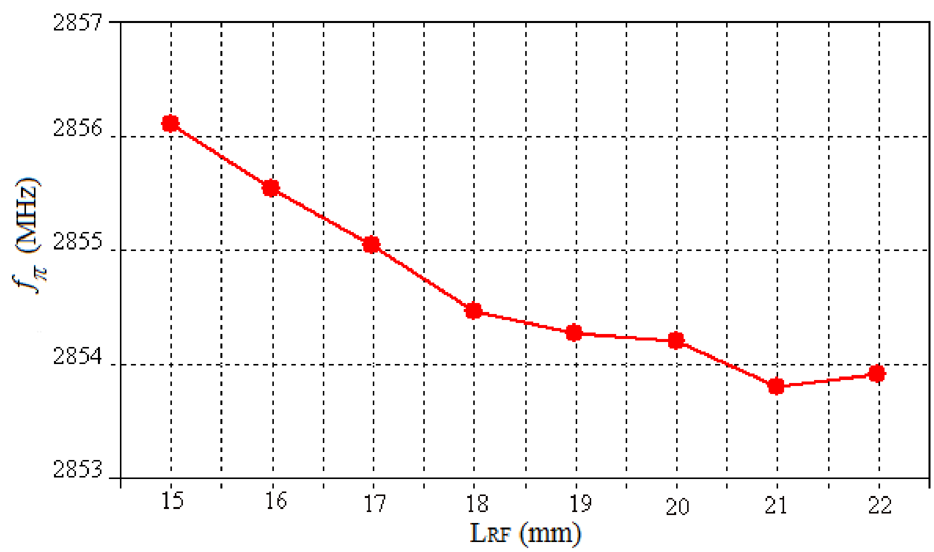

Fig. 5.16: Variation in f_π with length of RF coupling slot (L_{RF}) for constant radius of full- and half-cell tuned for f_π of 2856 MHz for very small values of β_π, and with e_b ~1.

On other hand, if β_π and e_b are first tuned to the targeted values by an appropriate choice of L_{RF} and R_{ch}, and f_π is tuned next by taking machining cuts on R_{cf} then an increase in R_{cf} reduces f_f, which in turn reduces e_b, as the full-cell frequency f_f becomes less than the half-cell frequency f_h. Therefore, this method also cannot be employed. Similarly, if β_π is first tuned to the targeted value of unity, and e_b is kept high compared to the desired value (unity), and f_π is then tuned by varying R_{cf} then f_π decreases monotonically with increasing R_{cf}, and becomes 2856 MHz at R_{cf} = 41.525 mm as shown in Fig. 5.18. The field balance e_b also decreases monotonically with R_{cf} as shown in Fig. 5.19, and becomes unity at R_{cf} = 41.525 from its initial value of ~ 4. But in this case β_π also decreases with R_{cf} as shown in Fig. 5.20, and reduces to 0.55 at R_{cf} = 41.525 mm, where f_π and e_b are tuned to desired values. For the full-cell, it is therefore necessary to simultaneously obtain the appropriate values of R_{cf} and L_{RF} that will give the desired values of f_π and β_π.

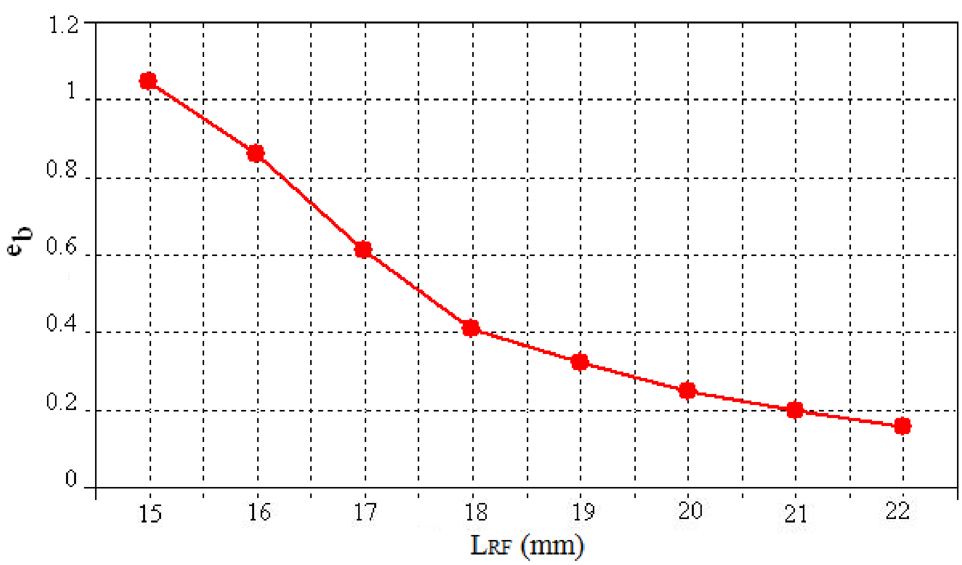

Fig. 5.17: Variation in e_b of π-mode with length of RF coupling slot (L_{RF}).

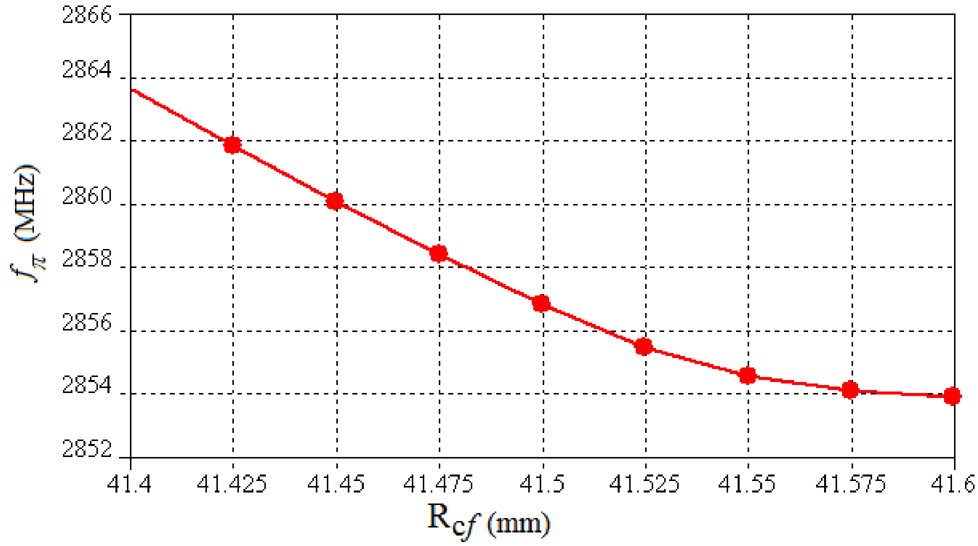

Fig. 5.18: Variation of f_π with radius of the full-cell for a constant length of RF coupling slot (L_{RF}) for which β_π =1.

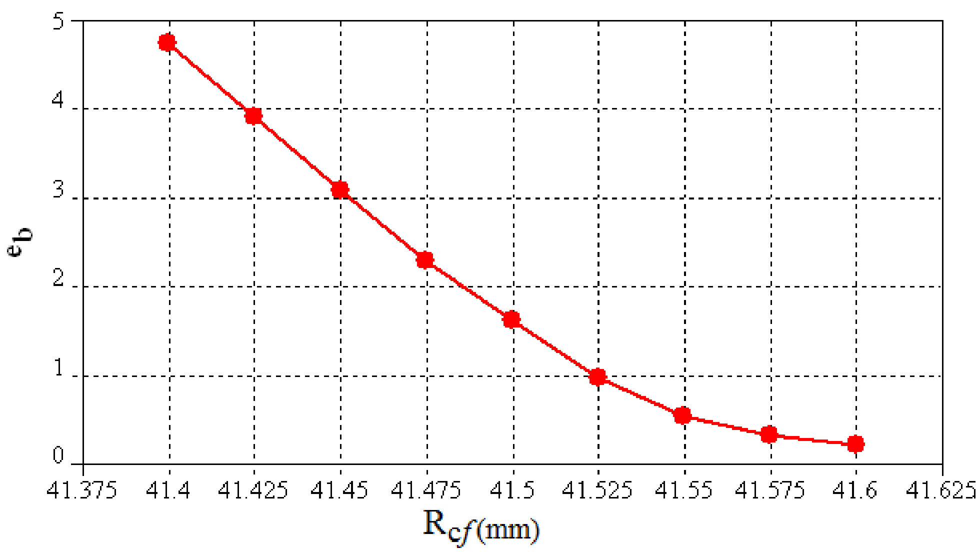

Fig. 5.19: Variation in e_b of the π-mode with radius of full-cell, for a constant length of the RF coupling slot (L_{RF}) for which β_π =1.

From above parametric study it is clear that the RF parameters of the gun cannot be tuned one by one and have to be tuned simultaneously. To do this one should be able to predict the interdependence of the RF parameters and predict the required geometrical dimensions to achieve the desired RF parameters. A scaling law developed for this is discussed in the next section.

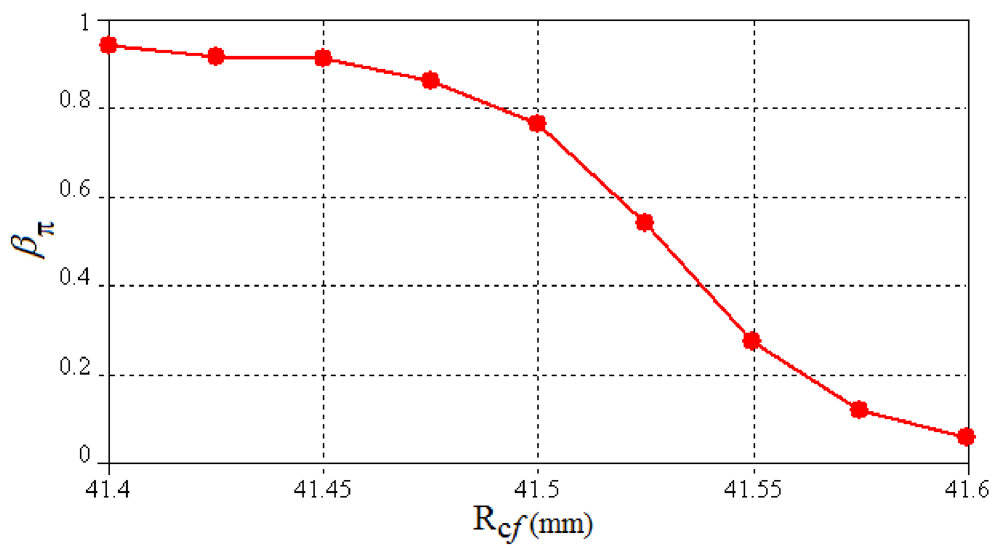

Fig. 5.20: Variation in β_π with the radius of full-cell.

5.4.2 Determination of Radius of Independent Cells and Length of RF Coupling Slot for Desired Independent cell RF Parameters

To predict the ID of the independent cells of a photocathode RF gun, the variation of independent-cell frequency with its radius has to be known. For an ideal pillbox cavity, the resonant frequency of the TM_{010} mode varies with radius as $f = 2.405c/2\pi R_c$, where c is the velocity of light and 'R_c' is the radius of the pillbox cavity. The geometry of the gun cells is like a pillbox but due to the presence of beam entry and exit ports, along with other openings for tuners, vacuum pumping, RF power coupling, and coupling of the laser, the variation in the frequency of the independent cells will be different from the '$1/R_c$' dependence of the pillbox.

Considering a scaling law of the form

$$f_i = a_i R_{ci}^{-bi} \ , \tag{5.15}$$

where a_i and b_i are constants that depend upon the cell geometry, and subscripts $i = h, f$ refer to the half- and full-cell respectively. The values of the constants for the half-cell can be determined by performing SUPERFISH simulations of a photocathode gun with a detuned full-cell – *i.e.* where R_{cf} has been deliberately increased to reduce f_f to such an extent that the two cells oscillate independently [88, 89]. Similarly, the values of the constants for the full-cell can be determined by performing simulations with a detuned half-cell. Figures 5.21 show the field plots obtained from SUPERFISH for the two cases discussed above. In Fig. 5.21(a), the fields are concentrated in the full-cell with negligible field in the half-cell, indicating no coupling between the two. Similarly, Fig. 5.21(b) shows the field concentrated in the half-cell with negligible field in full-cell. Using this procedure of detuning the half- and full-cells, the values of the constants a_i and b_i have been derived to be: a_h = 1.89343 x10^8 and b_h= 0.85245 for the half-cell, and a_f = 9.522112x10^7 and b_f = 1.0743, for the full-cell.

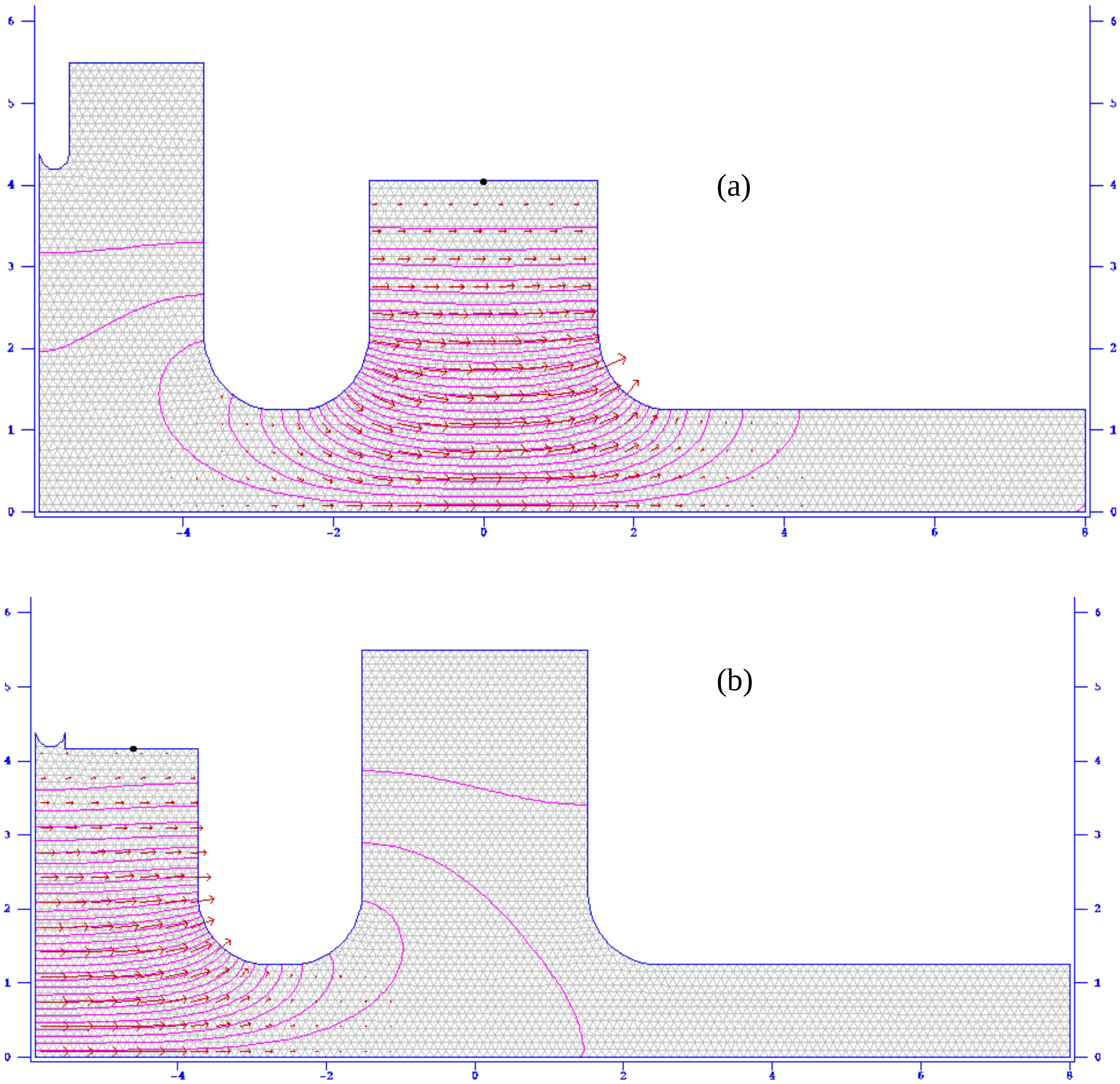

Fig.5.21: Scheme for detuning one cell to predict the variation of independent cell frequency with its radius, (a) for the full-cell and (b) for the half-cell.

To verify the validity of the scaling law, small machining cuts were taken on the IDs of machined half- and full-cells, and values of the resonant frequencies f_h and f_f were measured and compared with those predicted by the scaling law. Figures 5.22 and 5.23(a) show a comparison of f_h and f_f predicted by the scaling law with those from actual experimental measurements for the half and full-cell respectively. For the half-cell, the measured variation in f_h with R_{ch} agrees very well with the scaling law, while the situation is more complicated for the full-cell where experimentally measured values show a constant deviation from values predicted by the scaling law. This is because while the perturbation in the half-cell frequency due to the laser ports is negligible on account of their small size, the perturbation in f_f due to presence of the RF and vacuum ports is not negligible. This can be seen in Fig. 5.23(a), where the experimental results have a constant deviation from the predicted values. To explain this we include the effect of the ports on the frequency of cells.

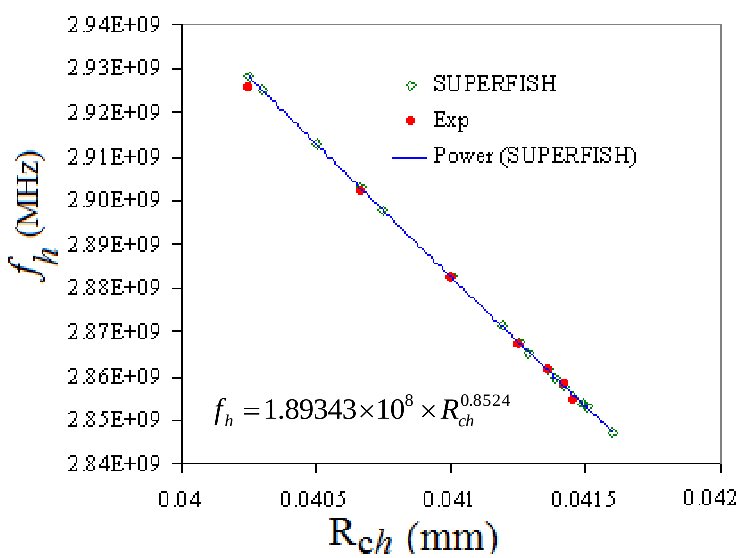

Fig.5.22: Variation in half-cell frequency with its radius predicted by SUPERFISH and measured experimentally.

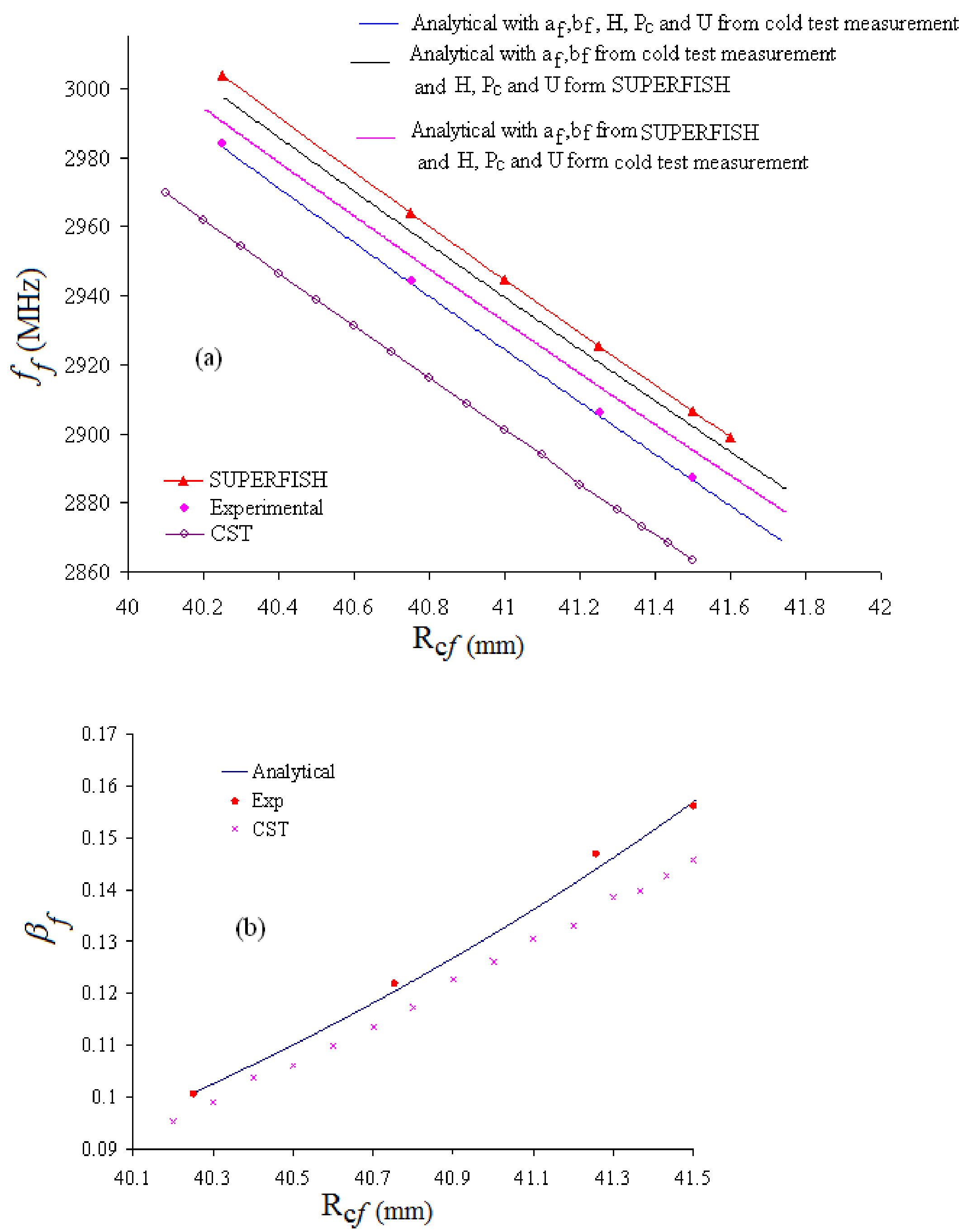

Fig. 5.23: (a) Variation in f_f and (b) β_f with the full-cell radius for L_{RF} =15 mm.

According to Slater's perturbation theorem[90] the change in resonant frequency due to the presence of port openings on a cavity wall is given by

$$f^{2} = f_0^{2}\left(1-\sum_i \Delta f_i\right) , \tag{5.16}$$

where f_0 is the resonant frequency of the cavity without port openings, and Δf_i is the change in resonant frequency due to the ith port opening, which depends upon the geometry of the port opening and the strength of the magnetic field at the location of the hole.

The full-cell normally has four port openings – two circular tuner ports located diametrically opposite to each other, and oblong RF coupling and vacuum pumping ports located diametrically opposite to each other and orthogonal to the tuner ports. Due to the presence of these port openings, Eq. (5.16) for the full-cell frequency gets modified to,

$$f_f^{\,2} = \left(\frac{a_f}{R_{cf}^{b_f}}\right)^2 \{1-\Delta f_{RF} - \Delta f_{vacuum} - \Delta f_{tuner1} - \Delta f_{tuner2}\} , \tag{5.17}$$

where Δf_i, i=RF, vacuum, tuner1, tuner2, is the change in frequency due to the presence of port openings for RF coupling, vacuum pumping, and tuner ports 1 and 2 respectively. The change in resonant frequency due to ports can be determined by employing Gao's scaling law [91]. To avoid the excitation of dipole modes, the length of diametrically opposite ports is kept equal. Therefore change in resonant frequency due to opposite ports is also equal. The RF and vacuum ports are oblong in shape and can be treated as elliptical apertures as discussed in Ref. 92, and the change in frequency due to these ports is then given by,

$$\Delta f = \frac{2\pi\mu_0 L_{eq1}^3 e_0^2}{12[K(e_0) - E(e_0)]} \frac{H_1^2}{U} \left(1 - e^{-2\alpha d}\right), \tag{5.18}$$

where L_{eq1} is the semi-major axis of the ellipse, which is related to the actual length of RF coupling slot 'L_{RF}' in the following straightforward way : $L_{eq1} = \left(\pi R_w^2 + 2R_w D_w\right) / \pi R_w$, where R_w is the radius of the two semi circles and D_w is the distance between the centers of the two semi circles, with $L_{RF} = D_w + 2R_w$ as shown in Fig. 5.24 [91]. H_1 is the strength of the magnetic field at the location of the aperture and in the absence of the aperture, U is the energy stored in the cavity, α is the attenuation constant, 'd' is the thickness of slot and $e_0 = \left[1 - \left(L_{eq2} / L_{eq1}\right)^2\right]^{1/2}$ where L_{eq2} is the semi-minor axis of the ellipse (equal to the width of the RF coupling slot) and is given by $L_{eq2} = R_w$. $K(e_0)$ and $E(e_0)$ are complete elliptic integrals of the first and second kind [91].

The variation due to each tuner port is given by

$$\Delta f_{tuner} = \frac{4a^3\mu_0}{3} \frac{H_1^2}{U} \left(1 - e^{-2\alpha_t d_t}\right), \tag{5.19}$$

where a is the radius, α_t is the attenuation constant and d_t is the thickness of the tuner port. The thickness of the tuner port is given by $d_t = \Phi_f / 2 - R_{cf}$, where Φ_f =133.4 mm is the outer diameter (OD) of the full-cell. Substituting Eqs. (5.18) and (5.19) in Eq. (5.17), with the values of constants for the full-cell, the value of R_{cf} required for a desired value of f_f can be determined.

For the half-cell, the value of Δf for the laser ports, obtained from Eq. (5.18), is of the order of 85 kHz, which is very small, and can be neglected. Then, the scaling law for the half-cell given by Eq. (5.15) is valid, as shown in Fig. 5.22, and can be used to determine the value of R_{ch} required for a desired value of f_h.

The length L_{eq1}, for any desired value of β_f can be predicted by employing Gao's scaling law [38] given by,

$$\beta_f = \frac{\pi^2 Z_0 k_0 \Gamma_{10} e_0^2 L_{eq1}^2 e^{-2\alpha d}}{9ab[K(e_0) - E(e_0)]^2} \frac{H_1^2}{P_c}. \tag{5.20}$$

Knowing L_{eq1}, length of RF coupling slot 'L_{RF}' can be derived using the expression given earlier. Here H_1 is the magnetic field strength on the wall of the same cavity without the coupling slot, P_c is the total power loss in the cavity and 'd' is the thickness of the RF coupling slot given by $d = D - R_{cf}$, as shown in Fig. 5.24.

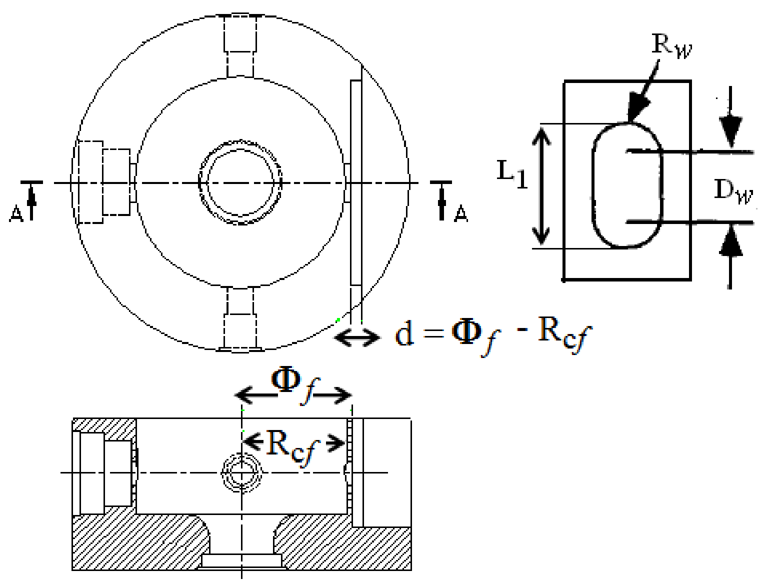

Fig.5.24: Cross-section of full-cell showing thickness of RF coupling slot.

Equation (5.17) for the dependence of f_f on R_{cf} shows that f_f also depends upon L_{RF} through Δf, while Eq. (5.20) for the dependence of β_f on Leq_1 (and hence L_{RF}) also shows its dependence on R_{cf} through d. From Eqs. (5.17) and (5.20), the values of R_{cf} and L_{RF} for any desired value of f_f and β_f can be obtained self-consistently. This simplifies the tuning procedure for the independent full-cell of the photocathode gun by incorporating the interdependence of f_f and β_f. Tuning the independent half-cell is straight-forward, as discussed earlier. Hence, tuning of a photocathode gun structure for desired f_π, β_π and e_b is significantly simplified by using the two-step tuning procedure, with the new scaling law given by Eq. (5.17). This formulation effectively eliminates the need for 3-D electromagnetic simulations, and minimizes the steps in tuning the gun by the cut-and-measure technique.

5.4.2.1 Correction for Air

Since the targeted RF parameters f_π, β_π and e_b are for final operation of the photocathode RF gun after brazing and under vacuum, while tuning is usually done before brazing and in air, the effect of change in dielectric constant from air to vacuum, as also the effect of change in physical condition before and after brazing, need to be incorporated in the targeted values of the RF parameters of the independent cells during tuning. The change in frequency due to vacuum can be calculated from an LC-circuit analysis of the cavity, and is given by $\Delta f = f_0\left(1-\sqrt{\varepsilon_r}\right)/\sqrt{\varepsilon_r}$, where ε_r =1.00059 [92] for dry air at normal temperature and pressure (NTP). For f_0 = 2856 MHz in vacuum, the corresponding Δf due to air is -0.842 MHz, which agrees very well with the frequency change of 0.9 MHz reported in the literature [93]. Hence, if the desired f_π under vacuum is 2856 MHz, one has to target 2856 - 0.842 = 2855.158 MHz during tuning in air.

5.4.2.2 Study of Brazing Effect

The effect of brazing on f_f and β_f was studied through SUPERFISH simulations of a photocathode gun without ports. From brazing considerations, a clearance of ~ 25-50 μm is usually maintained at the location of the joint between the full- and half-cells of a photocathode gun as shown in Fig. 5.25. This clearance is present during tuning, but gets filled up with the brazing filler after brazing, which causes a change in f_f before and after brazing. SUPERFISH simulations show that f_f decreases linearly with brazing clearance with a gradient of -0.127 MHz/10 μm. Using the value of H_1^2/P_c derived from these simulations in Eq. (5.20), β_f after brazing becomes 1.17 times its value before brazing. This change is like a step function and is independent of variations in the value of the brazing clearance. The variation of f_f and β_f with brazing clearance is shown in Figs. 5.26(a) and 5.26(b) respectively for a fixed length of joint.

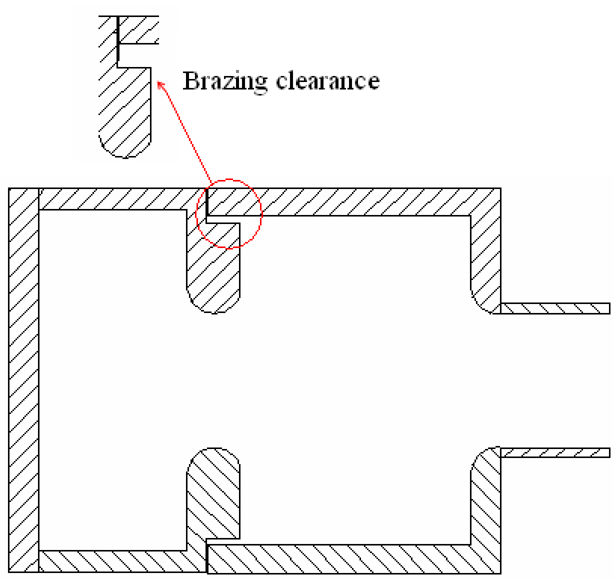

Fig. 5.25: Brazing clearance between the full-cell and half-cell.

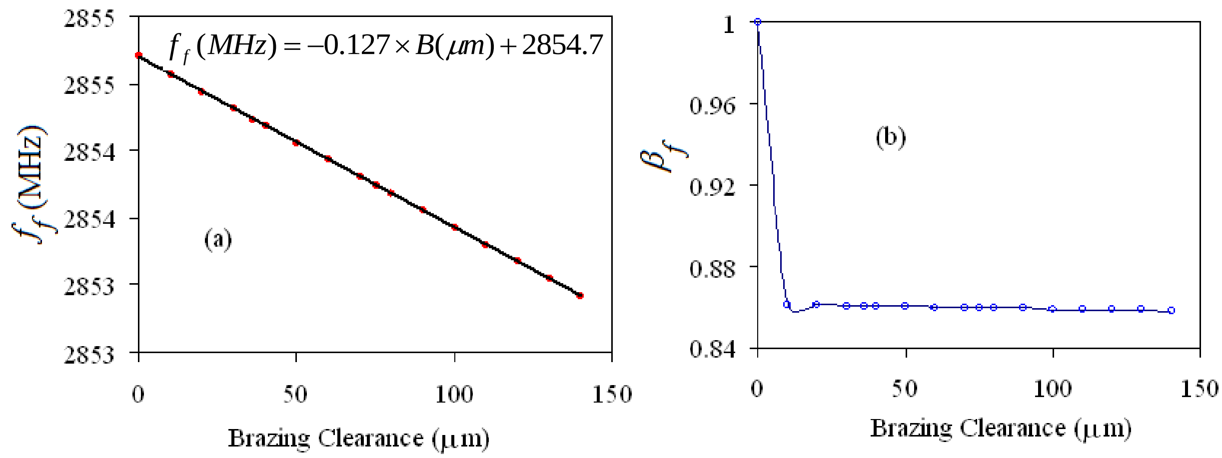

Fig. 5.26: (a) Variation in f_f and (b) variation in β_f with brazing clearance predicted by SUPERFISH.

5.4.3 Method for Tuning a Photocathode RF gun for Desired RF Properties

Using the scaling law discussed in the previous section along with the predictions of the LCR circuit analysis, a photocathode RF gun can be tuned for any desired set of RF properties by the following procedure:

Step 1: Decide the π-mode parameters (f_π, e_b, β_π) under vacuum.

Step 2: Correct for the dielectric constant of air, and get the π-mode parameters to be tuned in air.

Step 3: Using the LCR-circuit analysis, obtain the required independent cell RF parameters (f_h, f_f, β_f) after incorporating the effect of brazing.

Step 4: Determine the value of R_{ch} using Eq. (5.15) and the values of R_{cf} and L_{RF} using Eqs. (5.17) and (5.20) simultaneously.

With the independent cell dimensions obtained above, the photocathode RF gun will demonstrate the desired RF properties after brazing and under vacuum.

5.4.4 Experimental Verification of the Tuning Procedure

Two 1.6 cell photocathode RF guns were successfully tuned using the procedure discussed above in conjunction with the two-step tuning procedure. Initially, the two independent cells of both the structures were machined with dimensions smaller than those of the standard BNL/SLAC/UCLA design. The RF coupling slot in particular was of very small size with β_f = 0.1, in order to simulate a full-cell without RF coupling slot.

The scaling law discussed above involves the determination of values of H_1^2/P_c, H_1^2/U, Q and 'R' for the full-cell and the values of Q and 'R' for the half-cell. Ideally, these values can be obtained from SUPERFISH simulations. However, due to the presence of different port openings which cannot be simulated using SUPERFISH and due to machining errors, values predicted by SUPERFISH could deviate significantly from actual values. A more accurate method would be to employ measured values of RF properties of actually machined cells to determine the above constants.

The value of Q for each independent cell can be measured by detuning the other cell, such that the inter-cell coupling between the cells is negligible (as discussed in section 5.3). Similarly, the value of 'R' for each independent cell can also be determined by doing bead-pull measurements with the other cell detuned. The value of H_1^2/P_c for the full-cell can be determined from Eq. (5.20) using a measured value of β_f for a very small length of the RF coupling slot such that β_f <<1. This initial value of H_1^2/P_c can be put back into Eq. (5.20) to determine the required size of L_{RF} for any desired value of β_f. The value of H_1^2/U can be calculated by using the measured values of H_1^2/P_c and quality factor (Q_f) of the full-cell by using the following relation:

$$\frac{H_1^2}{U} = \left(\frac{H_1^2}{P_c}\right)\left(\frac{P_c}{U}\right) = \frac{H_1^2}{P_c}\frac{\omega_f}{Q_f}, \tag{5.21}$$

where $\omega_f = 2\pi f_f$. The comparison of measured values of Q, R, H_1^2/P_c and H_1^2/U with results of SUPERFISH simulations are given in Table 5.4.

Table 5.4: Comparison of measured values of different parameters of photocathode RF gun cells those with SUPERFISH results.

Parameters	Q_h	R_h (MΩ)	Q_f	R_f (MΩ)	H_1^2/P_c	H_1^2/U (x10^{10})
SUPERFISH	15788	1.08	14509	1.45	7280.52	1.11
Experimental	9765	1.14	11148	1.2	7510.32	1.26315

The values of constants a_i and b_i used in the scaling law for f_f and f_h can also be determined experimentally by measuring the independent-cell frequencies for two different radii. For the full-cell, the measurements have to be made with very small and constant length of RF and vacuum slots. Using Eq. (5.17) with these measured values of f_f and f_h, we get

$$b_f = \frac{\ln\left[\dfrac{f_{f1}}{f_{f2}}\dfrac{y_2}{y_1}\right]}{\ln\left[\dfrac{R_{cf1}}{R_{cf2}}\right]}, \tag{5.22}$$

and

$$a_f = \frac{f_{f1}}{y_1} R_{cf1}^{b_f}, \quad (5.23)$$

where f_{f1} and f_{f2} are the full-cell frequencies for radius R_{cf1} and R_{cf2}, and

$$y_1 = sqrt[1 - \Delta f_{RF} - \Delta f_{vac} - \Delta f_{tuner1} - \Delta f_{tuner2}]_{R_{cf} = R_{cf1}},$$

$$y_2 = sqrt[1 - \Delta f_{RF} - \Delta f_{vac} - \Delta f_{tuner1} - \Delta f_{tuner2}]_{R_{cf} = R_{cf2}}.$$

Similar expressions can be obtained for the half-cell. The comparison of different constants predicted from experimental measurements and from SUPERFISH is given in Table 5.5.

Table 5.5: Constants of different cells predicted by scaling law and from SUPERFISH simulations.

	a_i			b_i		
	SUPERFISH (no brazing clearance, vacuum)	SUPERFISH, (brazing clearance 36 μm, air)	Experimental (brazing clearance, air)	SUPERFISH (no brazing clearance, vacuum)	SUPERFISH (brazing clearance 36 μm, air)	Experimental (brazing clearance, air)
Full-cell	9.522112 e7	9.5046e7	9.2964e7	1.0743	1.0748	1.0810
Half-cell	1.89343e8		2.22292e8	0.85245		0.82024

To check the validity of the scaling law, we predict the variation of f_f with R_{cf} using Eq. (5.17), with the constants a_f, b_f, H_1^2/P_c, H_1^2/U calculated from SUPERFISH and experimental measurements as discussed above. The prediction of the scaling law with constants taken from experimental measurements agrees very well with the experimental results as shown in Fig. 5.23. Figure 5.23(a) shows the agreement between measured and predicted values of variation of f_f with R_{cf}, while Fig. 5.23(b) shows agreement of variation in β_f with R_{cf} for a fixed slot-size. Since the prediction of the scaling law agrees very well with experimental results, the scaling law can be used to predict the geometrical dimensions for desired RF parameters of the full-cell too.

5.4.5 Experimental Results with Complete Photocathode RF guns

Using the procedure discussed above two photocathode RF guns have been tuned to the desired RF parameters [94, 95]. The results are summarized in Table 5.6. The experimental results agree very well with the predictions within 50 μm in ID of cells and 0.5 mm in length of RF coupling slot. The deviations observed can be attributed to the difference in machined dimensions from the predicted dimensions which are ~50 μm.

SUMMARY

The photocathode RF gun has been analyzed using an LCR circuit analogy and a two-step tuning method has been established. The analysis was further extended and a method to predict the geometrical dimensions of a photocathode RF for the desired set of RF parameters has been developed. The tuning methods were verified by tuning multiple prototypes of the gun made of aluminum, ETP copper and OFE copper.

Table 5.6: Comparison of experimental results with predictions.

Parameters	Predicted by SUPERFISH		Predicted by the scaling law using inputs from SUPERFISH and including effect of brazing and air		Predicted by scaling law using inputs from RF measurements and including effect of brazing and vacuum		Cold test before brazing in air		Cold test after brazing in vacuum	
	Gun 1	Gun 2	Gun1	Gun 2	Gun 1	Gun 2	Gun1	Gun 2	Gun1	Gun 2
Φ_h (mm)	82.98	82.98	82.98	82.98	82.99	82.87	82.91	82.91	82.91	82.91
Φ_f (mm)	84.40	84.40	83.98	83.97	83.69	83.64	83.67	83.65	83.67	83.65
L_{RF}(mm)	19.50	21.30	21.70	22.91	21.81	23.00	21.84	22.70	21.84	22.70
β_f	1.64	1.90	1.40	1.62	1.38	1.56	1.42	1.66	1.80	2.1
f_f (MHz)	2854.94	2854.94	2852.19	2852.19	2852.19	2853.76	2852.36	2853.82	2852.90	2854.26
f_h (MHz)	2853.99	2853.99	2853.15	2853.15	2853.00	2853.50	2853.67	2853.67	2853.67	2853.67
f_π (MHz)	2856.04	2856.04	2855.18	2855.18	2856.00	2856.00			2856.02	2856.35
β_π	1.00	1.20	1.00	1.20	1.00	1.20			1.06	1.27

CHAPTER 6

DEVELOPMENT OF PHOTOCATHODE RF GUN

AND OTHER SUB- SYSTEMS

INTRODUCTION

The performance of an accelerator is determined by a number of factors. Apart from a good design, the conformance of the actual cavity to its design values, the peak accelerating field gradient and the achievable vacuum level play an important role. These factors depend on the materials, quality and methods used during its construction. To support a high accelerating gradient the surface-finish plays an important role, while for achieving ultra-high vacuum the process of fabrication, and cleaning of surface and brazing joints are equally crucial.

Apart from the accelerating cavity, many more subsystems are needed for operation of a photocathode RF gun like (1) laser system, (2) RF system, (3) vacuum beam line, (4) magnets and (5) diagnostics for generation, acceleration, focusing, characterizing and transportation of the electron beam up to experimental station. The development of all required sub-systems is a cumbersome task and requires a team of experts. In our case also different sub-systems are developed by different experts and on behalf of them a brief description and status of different sub-systems is also presented for completeness.

6.1 STATUS OF REQUIRED SUB-SYSTEMS

6.1.1 Laser System

The wavelength, energy per pulse, pulse width, timing jitter and amplitude jitter are the key parameters of the laser systems for a photocathode RF gun. The wavelength and energy per pulse depend on the cathode material while other parameters depend on the frequency of the accelerating field in the cavity. These parameters, for a particular design, can be determined analytically, as discussed in Chapter 2. We use copper as photocathode hence require a laser wavelength less than 295 nm; the nearest available wavelength is 266 nm which the fourth harmonic of Nd:YAG / Nd:Glass / Nd:VAN lasers. Since the photocathode is operating at 2856 MHz the laser pulse width should be ~ 10 ps (phase-stable region of 2856 MHz) and the timing jitter should be less than a few ps. Considering the stability and pulse width requirements, the drive laser system is designed in two parts: (1) highly stable oscillator capable of producing laser pulses of ~10 ps repeating at 102 MHz (28^{th} sub-harmonic of 2856 MHz, which is required for synchronization of laser with RF), (2) Pulse selector to bring down the laser pulse repetition rate to 1-10 Hz (photocathode RF is operating at 1-10 Hz), (3) amplifier to boost the laser pulse energy and (4) fourth harmonic generator.

A mode-locked Nd:VAN oscillator system has been procured from M/s Time-Bandwidth (GE-100 VAN). This oscillator produces laser pulses of 1064 nm wavelength with a pulse width of 7 ps, energy of 2 nJ per pulse and repetition rate of 102 MHz (28^{th} sub-harmonics of 2856 MHz). The oscillator came with a stabilization unit (GLX-1000) which enables the oscillator to produce laser pulses with timing jitter ≤ 3 ps and amplitude jitter ≤ 1%. An amplifier system with pulse selector and fourth harmonic generator was procured from M/s Ekspla, Lithuania (model

APL2101). The repetition rate of the laser pulses from the oscillator is first down converted to 1-10 Hz (selectable in steps of 1) using a Pockels-cell based pulse selector, and then the energy of the laser pulses is amplified to 5-10 mJ by using a multi-pass Nd:YAG based amplifier. After that the laser pulses are passed through a BBO crystal based fourth harmonic generator to convert the laser wavelength from 1064nm to 266 nm. The efficiency of fourth harmonic generator is ~10% and hence the laser energy per pulse is 0.5-1 mJ, which can generate a peak charge of 1-5 nC. For synchronization between the laser and RF, the laser oscillator has a provision to accept a 102 MHz reference signal from the RF, as well as to produce a 10 MHz reference signal that can be used by the RF system. Either signal can be used for synchronization. A brief description on synchronization is given in Section 6.2.3.

6.1.2 RF System

To generate an electron beam of energy 3-4 MeV, an average accelerating field gradient of 35-40 MV/m (peak accelerating field of 87-100 MV/m) needs to be setup in the photocathode RF gun for which RF power of 2.5 to 4.5 MW is required. Since this electric field needs to be present only when electron bunches have to be accelerated, a pulsed RF power source is sufficient and klystrons are the most suitable sources as they have high gain, efficiency and long life. The klystron is an amplifier, and needs an input RF signal of few 100s of watts and a pulsed-modulated high DC voltage.

A klystron comprises four major components: a thermionic electron source with a DC-acceleration stage, an input RF cavity (which is also known as the buncher cavity), a drift space, and an output RF cavity (which is also known as the catcher cavity). The amplification of RF power in the klystron happens as follows: a pulse modulated high voltage is applied to the DC-acceleration stage where electrons from the thermionic electron gun are accelerated. These electrons then enter the buncher cavity which is fed by an input RF signal. The input RF signal in the buncher cavity introduces velocity modulation in electron beam as a consequence of which the electrons get bunched at the frequency of the input RF signal. The spacing between the buncher and the catcher cavity is kept such that electrons get bunched when they reach to the catcher cavity. These bunched electrons lose their energy while passing through the catcher cavity and setup an RF field inside it (or, in other words, fill the catcher cavity with RF power). The RF power is then extracted from the catcher cavity by a loop or a waveguide port. The efficiency of modern klystron amplifiers is ~ 50% with a gain of around 40-45 dB. A schematic of a typical RF system is shown in Fig. 6.1.

For the present application, a 25 MW peak power klystron (TH2171) has been procured from Thales Electron Devices, France. With a gain of 53 dB, the klystron requires an input RF power of 200 W for which a Solid State Pulsed Amplifier (SSPA) has been procured from Ruseltronics, Russia. The SSPA requires 10 mW of RF power for which a Rohde & Schwartz make signal generator (SML03) is used. The efficiency of the klystron is 40%. Therefore a 65 MW pulse modulator is required to generate the rated 25 MW RF power from the klystron. The modulator is presently in an advanced stage of development and is undergoing high power testing. High power RF testing of the gun will be performed after qualification of the modulator and the high power microwave system for which all required components like high power circulator, splitter, waveguide sections and Dual Direction Couplers (DDC) *etc*. have all been procured. A test microwave line from the klystron terminating into a matched load has been built for testing the klystron.

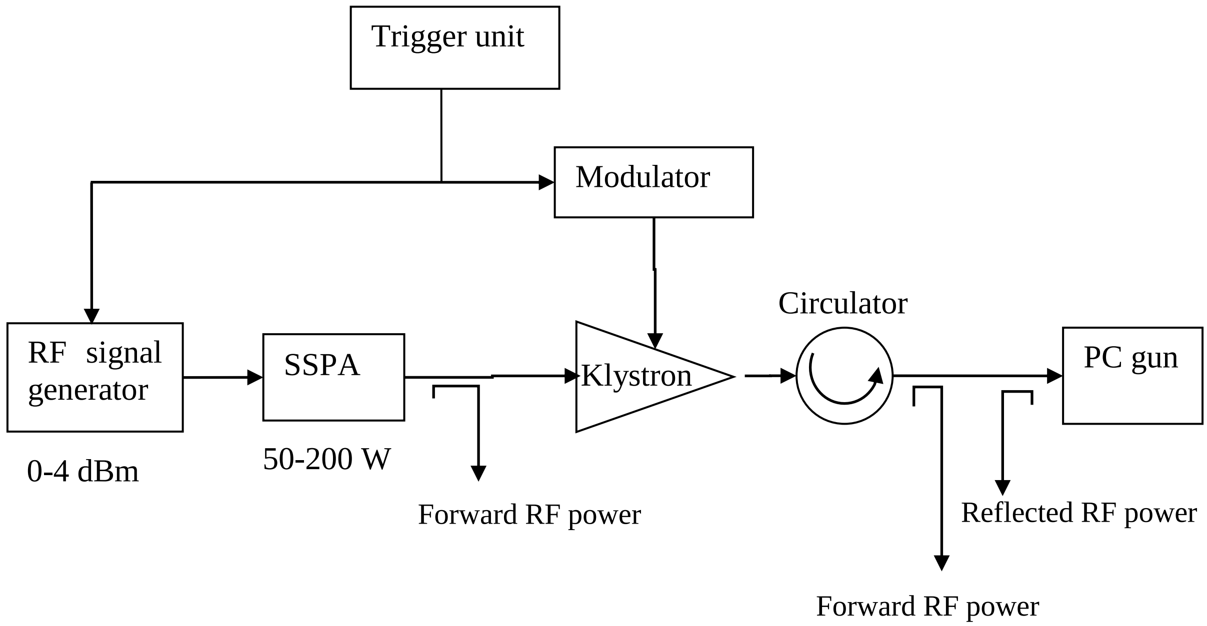

Fig. 6.1: Schematic layout of RF system for photocathode RF gun.

6.1.3 Laser and RF Synchronization

For efficient acceleration of electron bunches in the photocathode RF gun, electrons have to be created at a specific phase of the RF field as discussed in Chapter 3, *i.e.* synchronization is required between the laser pulse and the RF field. Both, the RF system as well as the laser system, consist of an oscillator and an amplifier. As a standard technique, two oscillators can be synchronized by using the same seed signal. In our case both the RF oscillator as well as the laser oscillator have provision to provide or take a reference signal as a seed, therefore either can be chosen as the master oscillator. However, it is found that by making the laser as master oscillator phase jitter can be reduced significantly [96]. With this consideration, a synchronization scheme was planned as shown in Fig. 6.2. The 10 MHz reference signal from the timing stabilization unit of the laser oscillator is fed to the RF signal generator as seed. The

RF signal generator then generates a 2856 MHz RF signal by using a multiplying circuit taking the 10 MHz signal as reference. To adjust the phase between the laser and RF, the output of the RF signal generator is fed to a low power phase-shifter. This signal is then fed to the SSPA which amplifies it to 200 W, which is then fed to the klystron. The RF signal generator gives a CW signal which is pulse modulated by using a Transistor-Transistor Logic (TTL) signal from a master trigger unit.

Since the photocathode RF gun is a standing wave structure, the amplitude of the accelerating field within the structure grows with time and reaches close to 95% of the peak amplitude in three fill-times. In our case one fill time is 0.66 μs, and so the laser pulse must shine on the photocathode after 2 μs (3 fill times). For this, the gating TTL signal for the RF system has to lead the gating TTL signal applied to the laser pulse selector unit by the same amount. To achieve this, both the TTL signals are derived from same master timing unit for synchronization.

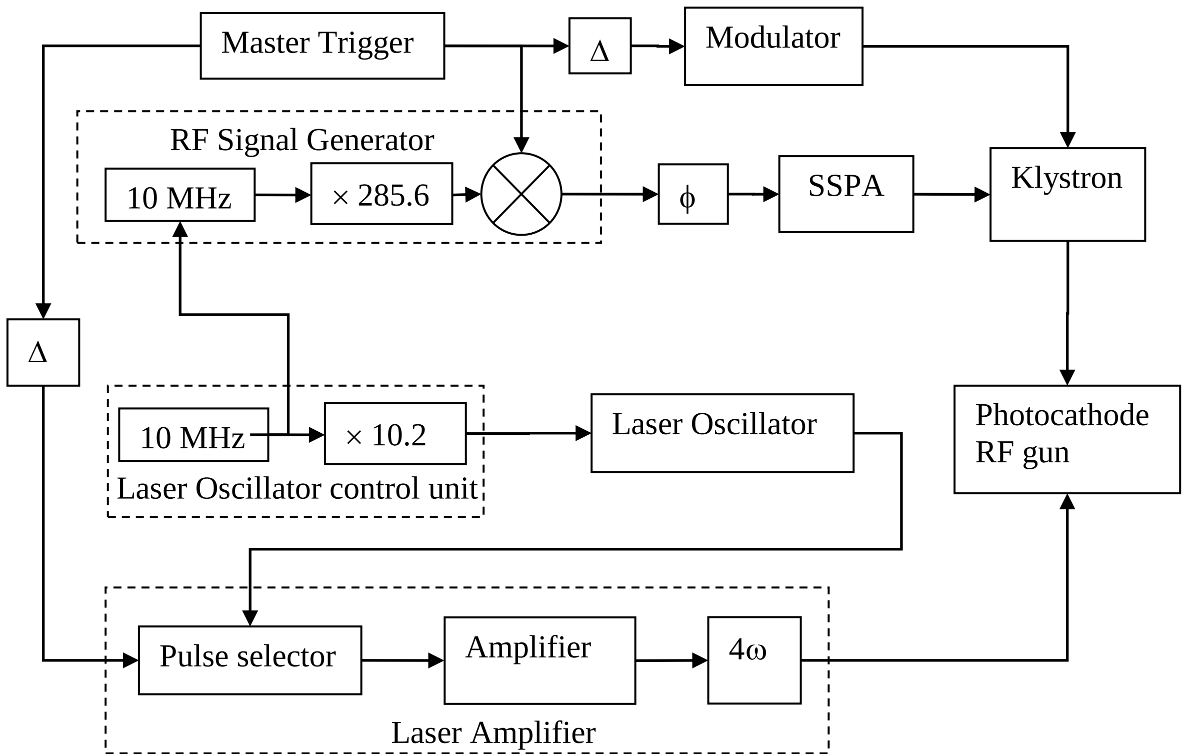

Fig. 6.2: Schematic of synchronization between laser and RF for photocathode RF gun.

Δ ≡Adjustable time delay   ϕ ≡ Adjustable phase delay

6.1.4 Solenoid

A solenoid magnet is used to apply a transverse focusing force to the electrons while they are accelerated. This transverse focusing is needed for three reasons: (1) to balance the radial de-focusing space charge forces inside the electron bunch, (2) to counter the exit-kick when the electrons leave the full-cell, and (3) for emittance compensation. For a photocathode RF gun these three functions can be achieved by using a single solenoid just after the full-cell. As discussed in Chapter 3, in order to minimize the beam size and emittance after the gun, the solenoid should produce an on-axis magnetic field of 2.7-3.2 kG. In order to meet these requirements a solenoid was designed using POISSON, the static magnetic field solver of the POISSON/SUPERFISH group of codes, and the ANSYS/EMAG codes, and was built in-house [19, 97]. The magnet consists of a coil with a total of 256 windings, surrounded by a low-carbon steel jacket to enhance and guide the magnetic field. The bore of the magnet is 72 mm. The outer diameter of the solenoid is 431 mm. The coil consists of eight double pancake sections. These sections have been connected in series for the electrical current and in parallel for cooling water. Each section consists of 32 turns made of square copper rod of 7×7 mm^2. These copper rods have 5 mm diameter hollow channel in the center for flow of cooling water. The nominal current is 133 A, which capable of producing an on-axis magnetic field of 3.230 kG. At this current the heat dissipation is 1.72 kW, which can be removed by cooling water with a flow of 9.42 l/min. Figure 6.3(a) shows a schematic of the coil arrangement in the solenoid while Fig. 6.3(b) shows a picture of the assembled solenoid without the top plate. Figure 6.4 shows the experimentally measured on-axis magnetic field profile and its comparison with ANSYS. The maximum field is 3.2 kG for a current of 130 A, which is in excellent agreement with the design value. The cathode is 217 mm away from the center of the solenoid and magnetic field at the cathode is 8.8 G when the peak field is 3.2 kG, as shown in Fig. 6.4. A picture of the assembled solenoid is shown in Fig. 6.5.

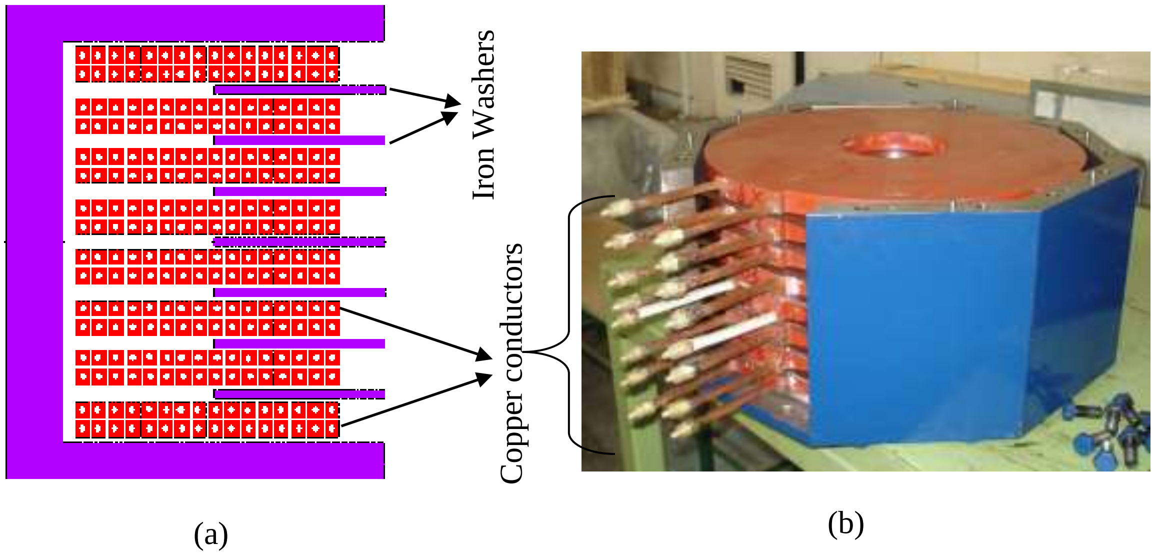

Fig. 6.3: (a) Schematic of coil arrangement and (b) picture of assembled solenoid.

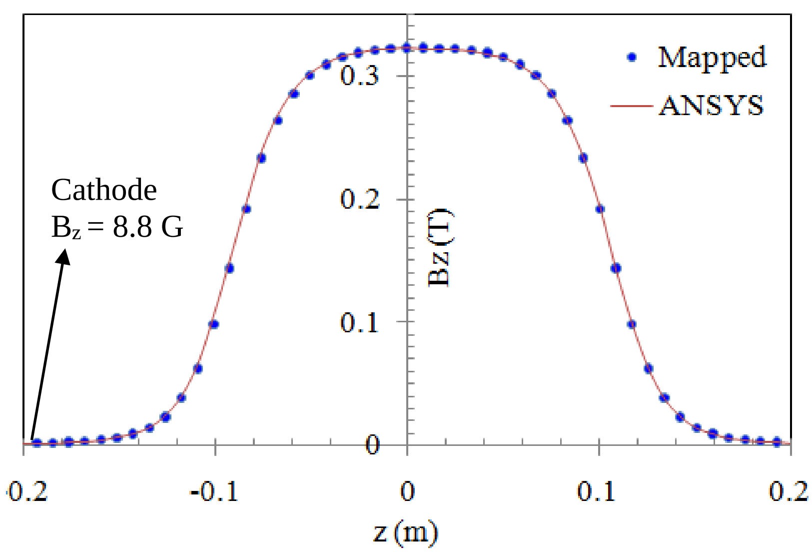

Fig. 6.4: Variation in on-axis magnetic field along solenoid length.

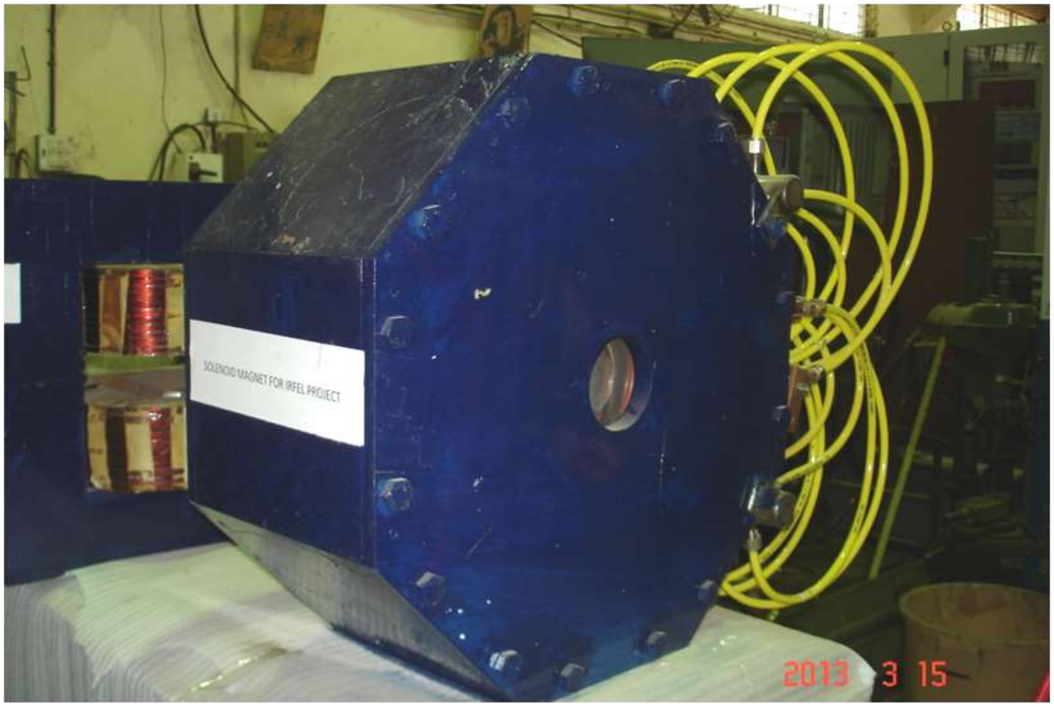

Fig. 6.5: Picture of assembled solenoid.

6.1.5 Quadrupole Magnets

The magnetic field of the emittance compensation solenoid is set for minimizing the emittance and not to focus the beam. When a focused beam is needed, additional optics has to be incorporated in the beam transport line. For this purpose a quadrupole triplet has been designed using the codes POISSON, ANSYS and TRANSPORT, and constructed in-house [97]. The quadrupole magnets have a pole width of 38 mm and the distance between the poles is 40 mm. Each pole consists of 46 windings of copper wire of 2.75 mm diameter. Figure 6.6 shows the front and side views of the assembled magnet while Fig. 6.7 shows the measured magnetic field along the quadrupole length at different transverse locations. Since the magnetic field at $r=0$ is zero, the electrons propagating in the z direction at the center of magnet experience no force while off-axis electrons experience a focusing force. The variation in the transverse magnetic field in the transverse plane at the centre of the quadrupole is shown in Fig. 6.8. The field gradient and effective length of the quadrupoles are 2.7 T/m/A and 82 mm respectively. An alignment and mounting system with XYZ movement has also been designed and developed for mounting and aligning the quadurpole in order to maximize beam transmission.

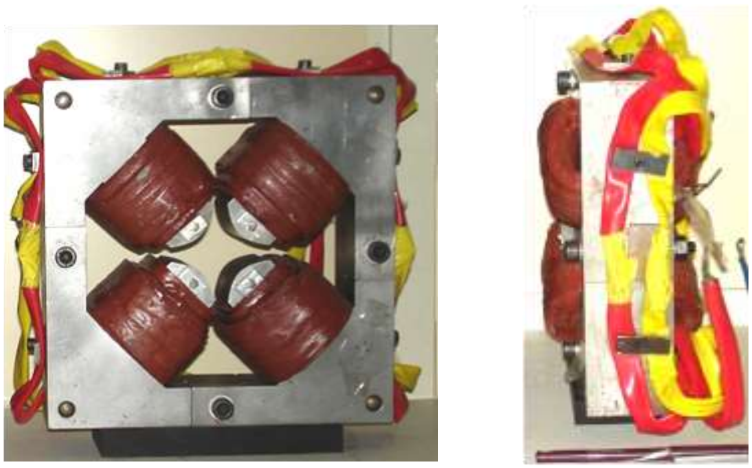

Fig. 6.6: Picture of quadrupole magnet.

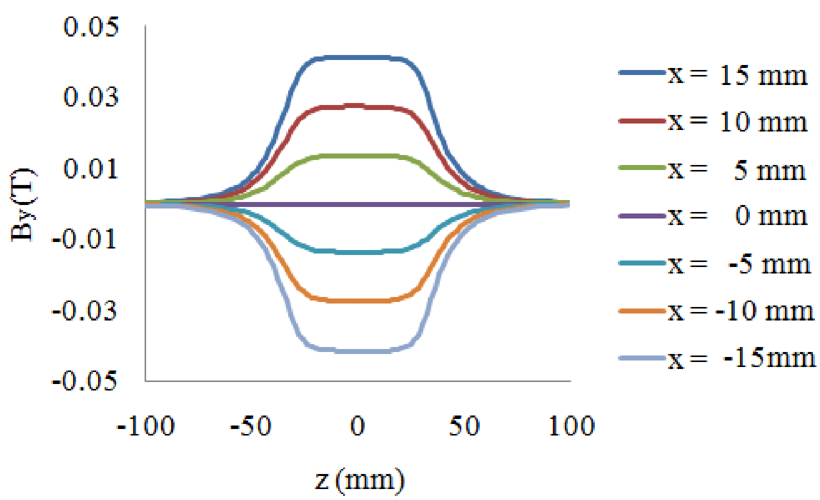

Fig. 6.7: Field variation in B_y along the quadrupole length at different transverse locations, for an excitation current of 10 A.

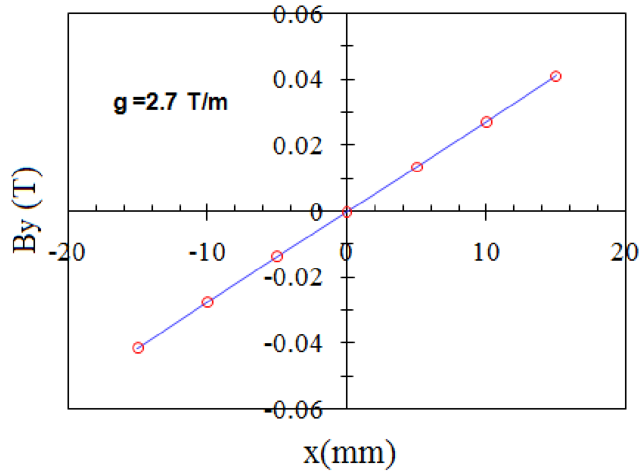

Fig. 6.8: Variation in B_y with x at the longitudinal centre plane of the quadrupole magnet.

6.1.6 Diagnostics

To measure the electron beam parameters, several diagnostic tools are planned to be installed in the beam transport line such as: (1) phosphor-screen based Beam Position Monitors (BPM) for measurement of the transverse profile of the beam, (2) Integrating Current Transformer (ICT) to measure the bunch charge, and (3) spectrometer to measure the beam energy and energy spread. To fully characterize the electron beam quality, an emittance measurement setup is also proposed using the quadrupole scan method [98]. The BPMs and bending magnet based energy analyzer have been designed and fabricated in-house and the ICT has been procured from M/s Bergoz Instrumentation, France, and qualified on the Compact Ultrafast TErahertz Free-Electron Laser (CUTE-FEL) setup [99].

6.1.7 Beam Line Components

The vacuum beam line components are fabricated using SS316L pipes with Con Flat flanges (CF flanges) and copper gaskets in order to achieve vacuum of the order of 10^{-8} mbar or better. Contamination during the manufacturing process can give trouble in achieving the desired vacuum level. To avoid this all components are chemically cleaned after machining, electro-polished and leak tested to better than $2x10^{-10}$ mbar l/s. After qualifying the leak test, all components are baked in a vacuum furnace at 400^0C for 4 hours. Before assembling these components in the beam transport line, all the components are leak-tested again to ensure that Ultra-High Vacuum (UHV) compatibility has not been compromised due to distortions during baking. After assembling the beam transport line, the whole line is again leak tested to test the integrity of the CF flange joints. Distributed pumping using Sputter Ion Pumps (SIPs) backed by Turbo-Molecular Pumps (TMPs) has been employed to achieve the desired vacuum level in beam transport line, which is monitored using integrated atmosphere to UHV gauges (PBR-260) from Pfeiffer Vacuum GmbH, Germany.

6.2 FABRICATION OF PHOTOCATHODE GUN COMPONENTS

The photocathode gun has six major components: (1) full-cell, (2) half-cell, (3) seal-plate, (4) cathode seal-plate, (5) cathode-plate and (6) waveguide, as shown in Fig. 6.9. Except for the seal-plate and cathode seal-plate, all other parts are subject to high accelerating field gradient, and hence were machined from Oxygen Free Electronic (OFE) grade copper, C10100 of ASTM standard F68-93, Metallographic Class I (oxygen content < 5ppm), on account of its high conductivity (5.8 $x10^7$ mho-m), purity and compatibility to operation in UHV conditions. The seal-plate, cathode seal-plate, different ports and CF flanges were machined out of Stainless

Steel (SS), AISI 316L. Since the RF parameters of the gun are affected by the geometrical dimensions of different components of the gun, *viz.* the Inner Diameter (ID) and length of the full- and half-cells, and the ID and thickness of the inter-cell coupling iris, as discussed in Chapter 4, these components are machined using a CNC (Computer Numerically Control) precision lathe. As the cathode plate and the half- and full-cells are subjected to high accelerating fields (of the order of 100 MV/m) one also needs to achieve a surface finish within 0.2 μm. The full-cell, half–cell and cathode plate were machined from a 150 mm Outer Diameter (OD) cylindrical rod of OFE copper. The inner surfaces of the half- and full-cells were machined using a CNC precision lathe after which port openings were machined by jig boring operation. As OFE copper is soft and can be distorted during machining, special soft-jaw chucks were used for holding the outer body of the components during machining. To prevent contamination of the surface, sulfur-free coolant was used during machining. Since polishing may introduce field emission sites on the RF surfaces, the desired surface finish was achieved by machining operation only. The machining process required to achieve the desired surface finish and geometrical tolerances was established by machining multiple prototypes followed by metrological inspections before machining of the final gun structures. As discussed in previous chapters, an asymmetry in the gun geometry deteriorates the beam quality, but several ports are essential in the photocathode RF gun structure, for example for shining the laser, RF power feeding, vacuum pumping and for frequency tuning. To minimize the asymmetry, ports were machined opposite to each other and their axis was maintained within ± 20 μm. Similarly the axes of the ID's of the cells and the inter-cell coupling / beam exit iris were also maintained within ±20 μm. The waveguide is machined out of a rectangular block of OFE copper by the wire-cutting technique with surface finish of 0.8 μm, as the electric field gradient in it is of the order of few kV/m only. After machining the geometrical dimensions and surface finish were confirmed by metrological inspection.

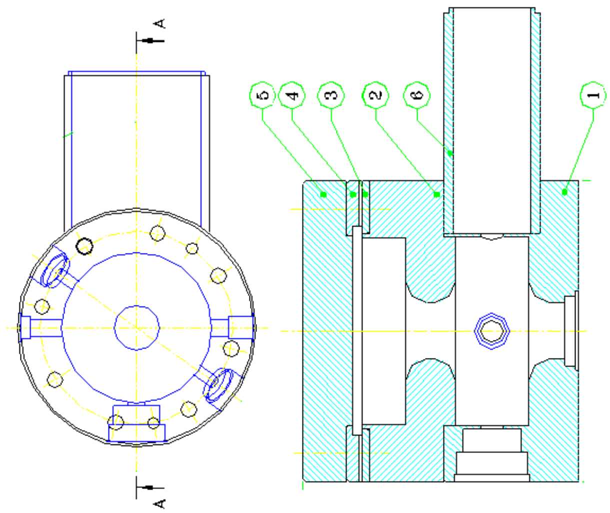

Fig. 6.9: Major components of the photocathode RF gun: (1) Full-cell, (2). half-cell, (3) seal-plate, (4) cathode seal-plate, (5) cathode-plate and (6) waveguide.

6.2.1 Brazing

To achieve Ultra-High Vacuum (UHV) in the gun during operation different components of the gun need to be brazed together. Along with UHV compatibility, the brazing must also ensure good electrical contact and minimum distortion in the gun geometry (in order to minimize variation in the RF parameters). The brazing of the gun involves multiple joints: (1) half-cell to seal-plate, (2) half-cell to laser ports at an angle of 22°, (3) half-cell to full-cell, (4) full-cell to tuner ports, (5) full-cell to rectangular waveguide, (6) full-cell to vacuum port, (7) waveguide to rectangular RF port flange, and (8) cathode-plate to cathode seal-plate. Since brazing of a photocathode RF gun involves joining of copper to SS, gold based alloys are usually employed worldwide at brazing temperatures of ~ 1,000˚C [100]. However, at these high temperatures the copper becomes very soft due to annealing and the geometry might get distorted by external forces which would lead to variation in the RF parameters of the gun, and is therefore not preferred. Although brazing fillers with a melting temperature of ~ 250°C, which is well below the annealing temperature of copper, have also been used for Cu-SS brazing [101] by copper plating the SS, this has a disadvantage that the maximum bake-out temperature for the cavity is restricted to approximately 150°C which gives trouble in achieving the ultimate vacuum. Along with the temperature, the wetting of filler material to the copper and SS surface, and UHV compatibility and, the strength of the braze joint also play a crucial role in filler material selection. Moreover, easy availability of the filler material is also an important consideration. Taking these factors into account, the Copper-Silver eutectic (72-28%) filler alloy (BVAg8), having a brazing temperature of 780°C, was used for brazing of the gun components.

Brazing can be carried out either in vacuum or in a hydrogen furnace [102] and both have their own advantages and limitations. In a vacuum furnace oxides from the copper surface cannot be removed, which may cause problems in the brazing joint. In a hydrogen atmosphere the oxides on the copper surface can be removed easily by reactive hydrogen at brazing temperatures; however diffusion of hydrogen in the copper may cause problems in achieving the desired vacuum. The issue of hydrogen diffusion in copper during the brazing process can however be resolved by subsequently degassing the brazed component in a vacuum degassing furnace at a temperature of > 400°C for few hours. Considering the advantages of hydrogen atmosphere brazing, this was the technique adopted for the photocathode RF gun. The brazing procedure is described below.

Brazing of the photocathode RF gun was carried out in two brazing cycles in a hydrogen furnace (HT 1800 G, Linn, Germany) having hot zone of 30 cm x 28 cm x 30 cm. The atmospheric air was removed from the furnace by flushing with N_2 at a flow rate of 80 SCFH (Standard Cubic Feet per Hour) for 30 minutes; subsequently high purity hydrogen (Iolar grade 1) was passed with a flow rate of 40 SCFH till completion of the brazing cycle. Dew point between -60ºC to -70°C was maintained inside the furnace hot zone to protect the SS 316L parts. All SS 316L parts were electroplated with copper to promote wetting of the brazing alloy. The photocathode RF gun structure has tubular butt-lap and rectangular butt-lap joints. To ensure the strength as well as UHV compatibility of brazing joints brazing clearance of the order of 30-50 μm was maintained in the tubular and rectangular lap joint region. This was ensured by inspection of each component after machining and electroplating. Along with UHV compatibility and strength it is equally important that the brazing filler should not flow on the inner surface of the half- and full-cells; otherwise it may lower the electrical breakdown strength. Considering this fact filler volume requirement for each joint was calculated and 30-50% extra volume of filler alloy was taken for practical considerations. The brazing filler used was in the form of a ring of 0.1 mm thick foil for the butt joints and a ring of wire of 1mm diameter for lap joints.

6.2.1.1 Assembly and Fixturing

During brazing the position of different components that have to be brazed together must be fixed such that the relative movement at brazing temperature is restricted. To ensure this a fixture was designed which has a base plate with curved guide to hold the seal-plate and SS post to locate the laser port on the half-cell. All fixture components were painted with stop-off to avoid the possibility of their being accidentally brazed to the photocathode RF gun components. Firstly, the seal-plate was placed on the base fixture plate, and respective brazing foil was placed on it. The half-cell was then fixed on the seal-plate. Then the laser ports were placed inside the step provided on the half-cell, and fixed in the required orientation by SS fixture blocks. The fixture blocks were then fixed on the base fixture plate by M6 bolts. The full-cell was subsequently placed on the half-cell with the brazing foil. After that the vacuum port, beam exit port and tuner ports were assembled with foil and wires on the full-cell. While assembling, the relative azimuthal orientation of the half-cell and full-cell were made such that the intersection of the laser port, tuner port, vacuum port and waveguide was avoided, as shown in Fig. 6.10. To maintain the brazing clearance and contact of tuner and vacuum ports with the body of the full-cell, they were held tightly by employing a low expansion material wire (molybdenum, 5 mm diameter). Three such wires of sufficient length were intertwined together for strength and fastened on the gun assembly by M5 bolts as shown in Fig. 6.10. A suitable graphite jig was placed inside the RF port slot on the full-cell to avoid any wire marks at the brazing surface. The assembly was ready for the first brazing cycle.

The gun assembly was placed in the furnace and aligned manually before starting the brazing cycle. It was ensured that the hot zone was completely filled with hydrogen by observing the burning of a pilot flame provided at the furnace outlet. The heaters (moly-silicide) were put on and temperature of 300^0C was attained after 10 minutes and soaked for 1.5 hours. The temperature was increased and soaking was done for 1.5 hours at 600^0C, for 1 hour at 700^0C and for 1.5 hours at 800^0C to ensure the equilibrium of temperature on the whole assembly.

Afterwards the temperature was increased to 850^0C in increments of 10^0C and held for 10 minutes at each step. The furnace was put off and job was removed from the furnace after which it cooled down to room temperature naturally. Figure 6.10 shows a picture of the photocathode gun after the first brazing cycle. The leak test of the gun after the first brazing cycle confirms the leak rate of 1.5 x 10^{-9} mbar l/s which was limited by rubber corks used to plug the different port openings.

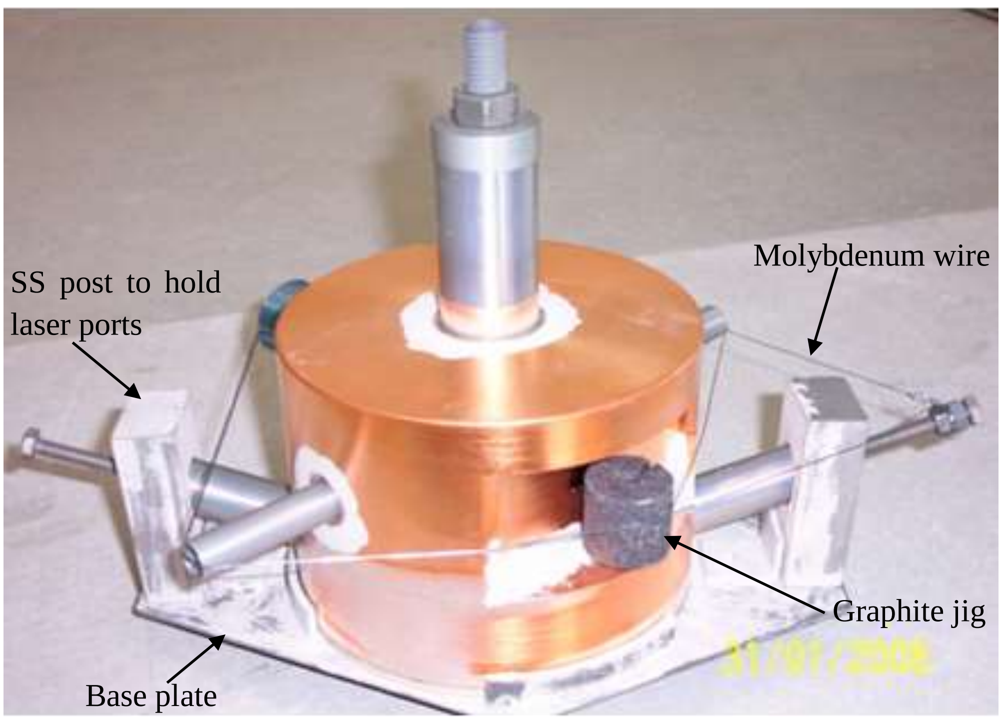

Fig. 6.10: Assembly of photocathode RF gun for first brazing cycle.

The gun from the first brazing cycle was assembled with the waveguide and RF port flange for the second cycle. The jigs and fixtures were held intact as done previously. The second brazing was done with the same thermal cycle as the first. The leak test after the second brazing again confirmed a leak rate of 2.5x 10^{-9} mbar l/s which was again limited by rubber corks used to plug the different port openings. Figure 6.11 shows a picture of the brazed photocathode gun after the second brazing cycle [103, 104]. Two such photocathode RF gun structures (named OFEGUN1 and OFEGUN2) have been developed successfully.

Fig. 6.11: Photocathode RF gun after second brazing cycle.

6.3 RF CHARACTERIZATION OF BRAZED PHOTOCATHODE GUN

6.3.1 RF Characterization in Air

RF parameters of the photocathode structures, such as the π-mode frequency, quality factor, and waveguide to cavity coupling coefficient, were measured using a VNA in reflection mode by feeding low power (mW) RF through the RF port. The photocathode RF gun was assembled with a dummy cathode plate having a hole of 10 mm at its centre and the variation in the on-axis electric field was measured by conducting a bead–pull measurement on the structure using a small dielectric bead (5.4 mm long and 5 mm diameter) made of green putty. A photograph of the bead-pull setup is shown in Fig. 6.12. The shunt impedance of the gun was calculated by using Eq. (2.14). The variation in the on-axis field along the length of the photocathode RF gun is shown in Fig. 6.13, while the experimentally measured RF parameters of the gun are given in Table 6.1.

The π-mode frequency, measured in air, is 2855.402 MHz for OFEGUN1 and 2855.507 MHz for OFEGUN2, which is expected to increase by 0.842 MHz in vacuum for both. The measured quality factor (Q_0) of 11,987 for OFEGUN1 translates to a fill time of 0.69 μs, while the Q_0 of 11,740 for OFEGUN2 gives a fill time of 0.58 μs. The measured shunt impedances of 3.24 MΩ for OFEGUN1 and 3.18 MΩ for OFEGUN2 translate to a requirement of ~ 3.5 MW of RF power to achieve a beam energy of 3 MeV. Figure 6.13 shows that the field balance in OFEGUN1 is 0.98 while for OFEGUN2 it is 1.05, which are both very close to the required value of unity.

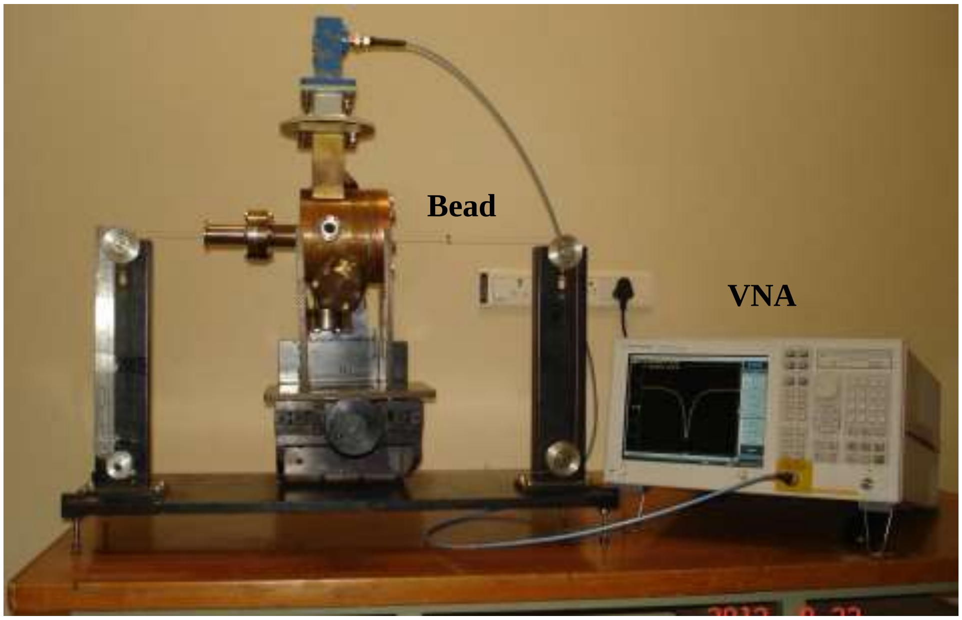

Fig. 6.12: Photograph of the bead-pull setup.

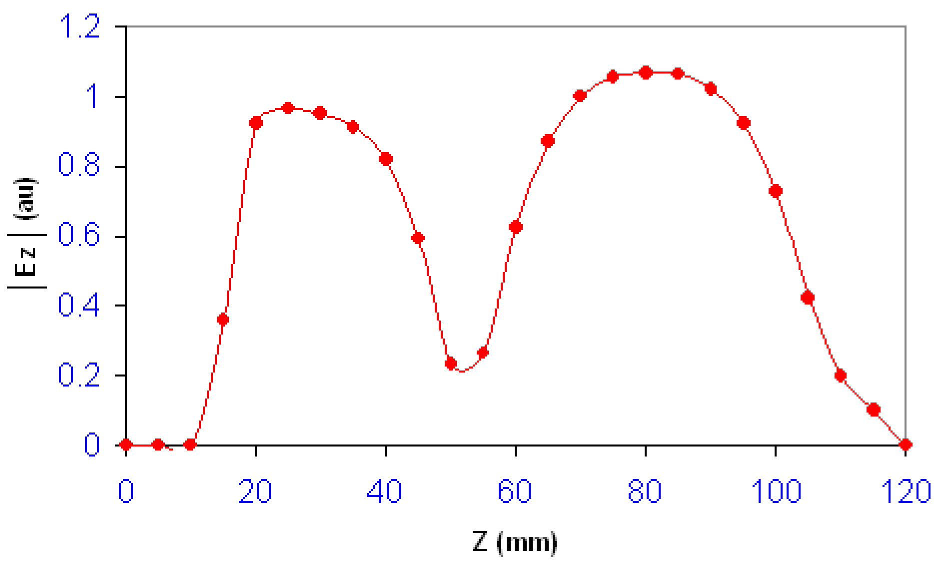

Fig. 6.13: On-axis accelerating field profile along the length of photocathode RF gun.

6.3.2 RF Characterization in Vacuum

All the ports of the gun were blanked off using CF blank flanges except for the RF and vacuum ports. The vacuum port was connected to an SIP-based pumping system and the RF port was connected to an RF window, in order measure the RF properties of the gun under vacuum. The VNA was connected to the RF window through a coaxial cable and a waveguide to coaxial adapter. The frequency spectrum of the photocathode gun under vacuum is shown in Fig. 6.14. The Smith Chart confirmed the critical coupling of the cavity with waveguide for π-mode, as shown in Fig. 6.15. Since bead-pull measurements could not be performed under vacuum the field balance was deduced from the mode separation between the ‘zero’ and ‘π’ modes. The RF properties of the two photocathode guns developed are given in Table 6.1.

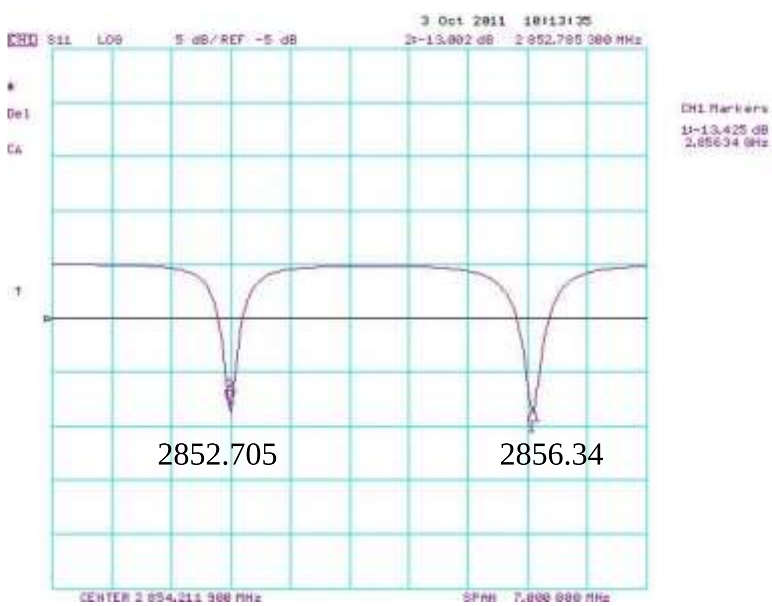

Fig. 6.14: Frequency spectrum of the OFEHUN2 under vacuum.

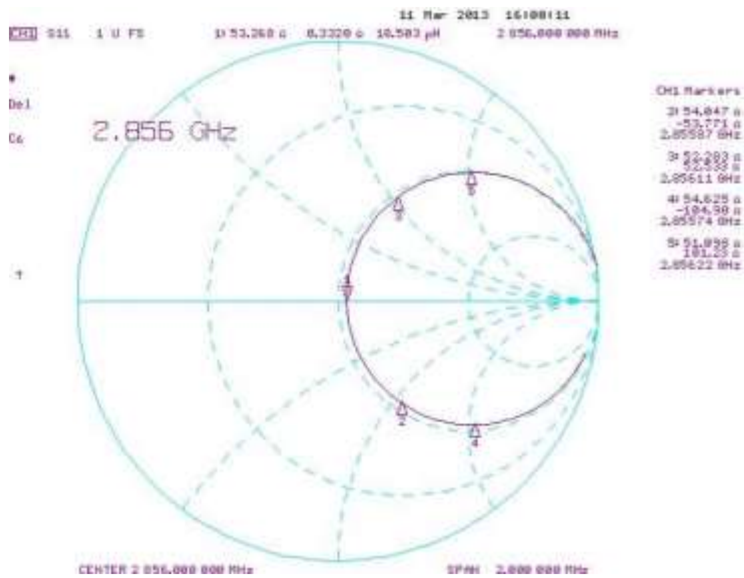

Fig. 6.15: Smith Chart of the OFEGUN1 under vacuum.

From the experimentally measured values of the shunt impedance, the expected beam energy from OFEGUN1 and OFEGUN2 is 3.06 MeV and 3.01 MeV respectively, for an input RF power of 3.5 MW. The variation in beam energy with input RF power is shown in Fig. 6.16.

6.4 TESTING OF UHV COMPATIBILITY

After brazing all the joints were leak-tested using a Mass Spectrometer Leak Detector (MSLD) (Alcatel, ASM 142) by plugging the port openings by using rubber plugs. The required CF flanges were then welded on the respective ports. The leak test at this stage confirmed a leak rate of 2 x10^{-10} mbar l/s for whole gun assembly with RF window. As discussed in the previous section, during brazing in a hydrogen furnace, hydrogen may defuse in the copper surface; to remove that the gun was degassed in a vacuum furnace at 400°C for 4 hours. The gun was mounted on an SIP (pumping rate 140 l/s) with a pumping chamber having provision to connect a vacuum gauge and a TMP (pumping speed 200 l/s). A vacuum level of $3x10^{-8}$ mbar was achieved in the gun within 48 hours.

Table 6.1: RF parameters of photocathode RF guns during cold test measurements.

Parameter	Cold test results			
	OFEGUN1		OFEGUN2	
	Air	Vacuum	Air	Vacuum
f_π (MHz)	2,855.402	2,856.02	2,855.507	2,856.35
Q_0	11,987	11,950	11,740	11,745
β_π	1.03	0.94	1.27	1.27
R (MΩ)	3.24	---	3.18	---
e_b	0.98	---	1.05	---
f_π-f_0 (MHz)	3.34	3.34	3.52	3.53

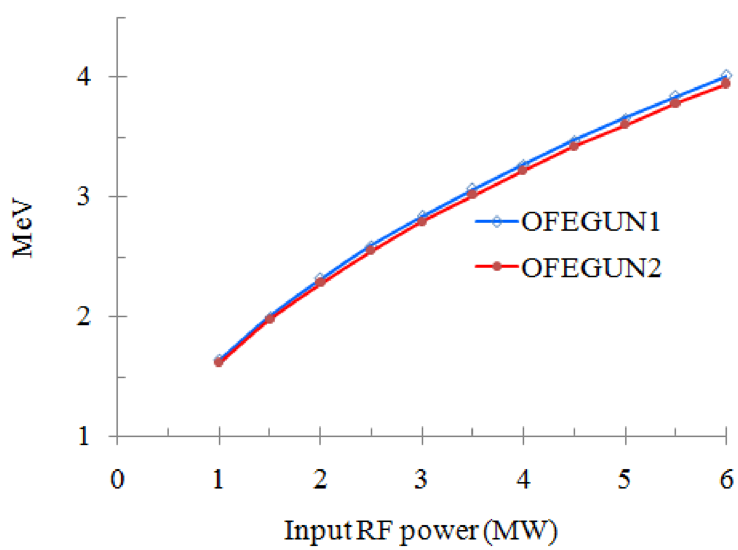

Fig. 6.16: Variation in beam energy with input RF power for OFEGUN1 and OFEGUN 2 based up on cold test results.

6.5 DEVELOPMENT OF HIGH POWER RF CONDITIONING SETUP

It is known that breakdown at high RF power limits the performance of accelerating cavities, and they have to be conditioned offline [105-107]. Therefore, a high power RF conditioning setup for RF conditioning of the photocathode RF gun, before actual beam acceleration, was built offline. A schematic of the RF conditioning setup is shown in Fig. 6.17. The high power RF conditioning beam line contains an FCT just after the exit port of the photocathode RF gun to measure dark current, a 90^0 bending magnet based energy analyzer to measure the energy spectrum of the dark current and two beam profile monitors, one in the straight section and another after the bending magnet, to measure the profile of the electron beam. Three SIPs are connected to achieve vacuum of the order of 10^{-8} mbar. The vacuum level in the RF conditioning beam line is monitored at three different locations by using BA gauges: one at the photocathode RF gun, one in the straight section and one after 90^0 bending. A picture of the assembled RF conditioning beam line is shown in Fig 6.18. The complete beam line has been pumped down to a vacuum of $3x10^{-8}$ mbar and readied for RF conditioning experiments.

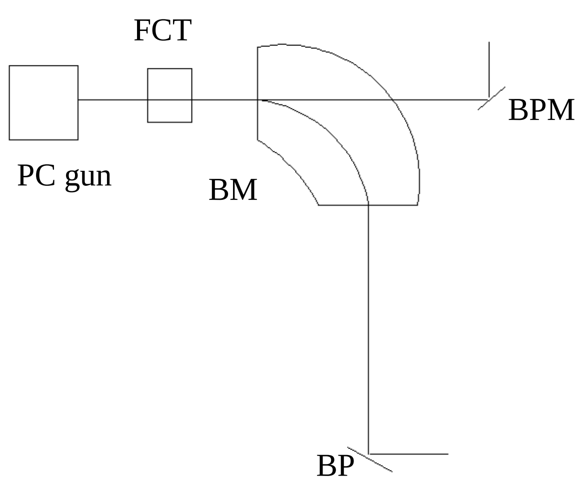

Fig. 6.17: Schematic diagram of high power RF conditioning setup for RF conditioning of photocathode RF gun.

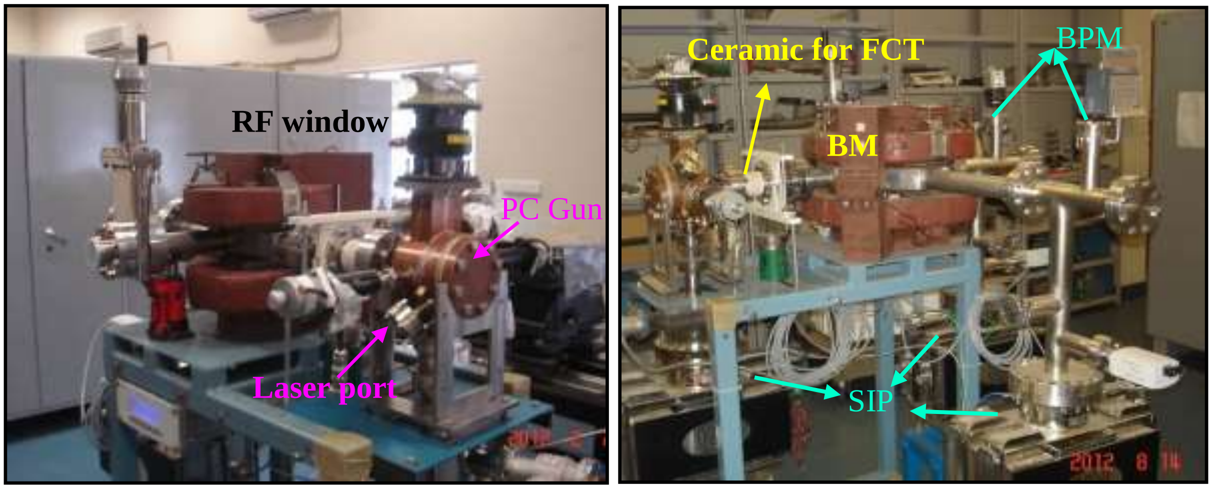

Fig. 6.18: Picture of photocathode RF gun high power RF conditioning setup.

SUMMARY

Two photocathode RF guns (OFEGUN1, OFEGUN2) have been machined, brazed and vacuum tested. The RF parameters of the guns are confirmed by cold test measurements in air and under vacuum. Sub-systems required for operation of the photocathode RF gun have also been developed and characterized. A high power RF setup has been developed and readied for high power RF test of the photocathode RF guns.

CHAPTER 7

CONCLUSIONS AND FUTURE PLANS

7.1 CONCLUSIONS

A 1.6 cell BNL/SLAC/UCLA type S-band photocathode RF gun has been designed using SUPERFISH and CSTMWS and the RF parameters optimized to minimize the emittance of the electron beam. Two structures of the photocathode RF gun have been developed. During development a novel two-step tuning procedure has been established to tune the photocathode RF gun to desired RF parameters. The two-step procedure is further extended to predict the geometrical dimensions of the gun cells during fabrication to achieve the desired RF parameters under operational conditions, which simplifies the tuning of a photocathode RF gun by eliminating the need of tuning of the gun by the iterative cut-and–measure technique used earlier. A procedure of brazing of the photocathode RF gun components in H_2 furnace has also been established and qualified by successful brazing of multiple structures with a leak rate of $2x10^{-10}$ mbar l/s. The gun structures have been characterization experimentally by measuring the RF parameters using a VNA and by confirming that the desired RF parameters were achieved. A high power RF conditioning test setup with the required diagnostics has been developed and pumped down to vacuum of $3x10^{-8}$ mbar and ready for high power test of the gun. The sub-systems required for operation of the photocathode RF gun like emittance compensation solenoid, quadrupole magnets, bending magnet, and vacuum beam line components have been developed in-house and other sub-systems like laser, RF and diagnostics have been procured. A beam transport line has also been designed, different components have developed and beam line readied for beam acceleration experiments. Although the end goal of acceleration of electron beam could not be met, however our research is beneficial to the accelerator physics community in the future, to develop and tune of the photocathode RF guns.

7.2 FUTURE PLANS

The results of our beam dynamics simulations, low power RF measurements, development of high power RF condition test setup and emittance compensation beam transport beam line points the way for future work described below.

As mentioned in previous chapter the high power RF conditioning setup is ready and development of high power RF system is in advance stage. Since RF conditioning has to be performed in a radiation shielded area, which is presently not available. A multipurpose Accelerator Test Area (ATA) for testing of accelerating structures developed in-house has been designed and is proposed to be constructed in near future. The high power RF system presently in advance stage of development will be installed in this area and the photocathode RF gun test setup will also be housed in this area where RF conditioning will be performed.

The RF parameter of the gun such as resonant frequency, quality factor, and waveguide to cavity coupling coefficient at high RF power level will be measured by analyzing the transient response of the reflected RF power. If there is any variation in the RF parameters due to RF power dissipation in the gun, then a algorithm will be developed to tune the gun to the desired RF parameters by controlling the cooling water temperature.

The design of a cathode plate capable to incorporate the cathode of different materials such as Mg, Al etc is underway, hence by replacing adjusting copper cathode plate study of quantum efficiency of different material will be carried out in order to find out the material with high quantum efficiency.

Since the laser system and other sub-systems are ready the beam acceleration experiments will be performed in the shielded area after high power RF conditioning.

The LCR circuit analysis will be further extended for multi-cell accelerating structures in order to establish a tuning method for desired RF parameters which reduce/eliminate the need of tuning by conventional iterative cut-and-measure technique.

REFERENCES

[1] C. Travier, "Rf guns: bright injectors for FEL", Nuclear Instruments and Methods in Physics Research, A 304 (1991), 285-296.

[2] Richard L. Sheffield, "High-Brightness Electron Injectors: A Review", Proceedings of Particle Accelerator Conference 1989, Chicago, USA, pp-1098.

[3] R. Chput *et al.*, "Operation of the CLIO accelerator", Nuclear Instruments and Methods in Physics Research, A 133 (1933), 267-271.

[4] J. L. Adamski *et al*. "THE BOEING DOUBLE SUB-HARMONIC ELECTRON INJECTOR - PERFORMANCE MEASUREMENTS", IEEE Transactions on Nuclear Science, NS-32(5), 2994-2996, 1985.

[5] W. B. Hermannsfeldt, "Low Emittance Thermionic Electron Guns", SLAC-PUB-4843, January, 1989.

[6] R. Alley *et al.*, "The Stanford linear accelerator polarized electron source", Nuclear Instruments and Methods in Physics Research, A 365 (1995), 1-27.

[7] Michael Borlend, "A HIGH-BRIGHTNESS THERMIONIC MICROWAVE ELECTRON GUN", Ph. D. thesis, Stanford University, 1991.

[8] Richard L. Scheffield, "High brightness electron sources", Proceedings of Particle Accelerator Conference 1995, Dallas, pp-882.

[9] O'shea P., "RF photoinjectors", Proceedings of 1st ICFA workshop on "high brightness beam" UCLA, published by World Scientific, 1999.

[10] J. S.Fraser *et al.*, "High brightness photo-injector for electron accelerators", IEEE Transactions on Nuclear Science, NS-32(5), 1791-1793, 1985.

[11] R. L. Sheffield *et al.*, "RF photoelectron gun experimental performance", Proceedings of Linear Accelerator Conference, 1988, Virginia, USA, pp-520.

[12] K. Batchelor, J. Sheehan and M. Woodle, “Design and Modeling of a 5 MeV Radio frequency Electron Gun”, BNL internal report BNL-41766, 1988.

[13] B. E. Carlsten, ‘New photoelectric injector design for the Los Alamos National Laboratory XUV FEL accelerator’, Nuclear Instruments and Methods in Physics Research, A285 (1989), 313-319.

[14] S. G. Anderson and J. B. Rosenzweig, “Nonequilibrium transverse motion and emittance growth in ultrarelativistic space-charge dominated beams”, Physical Review Special Topics – Accelerators and Beams, 3, 094201 (2000).

[15] S. Anderson *et al*., “Commissioning of the Neptune photoinjector”, Proceedings of Particle Accelerator Conference 1999, New York, USA, pp- 2006.

[16] K. Batchlor *et al*., “Performance of the Brookhaven photocathode rf gun”, Nuclear Instruments and Methods in Physics Research, A 318 (1992), 372-376.

[17] D. T. Palmer, “The NEXT GENERATION PHOTOINJECTOR”, Ph. D. thesis, Stanford University, 1998.

[18] Eric Ralph Colby, “Design, Construction and testing of a Radiofrequency Photo-injector for Next Generation Linear Collider”, Ph. D. thesis, University of California Los Angles, 1997.

[19] Arvind Kumar, “Novel rf structures for high-brightness photoinjectors and linear accelerators”, Ph. D. thesis, Raja Ramanna Centre for Advance Technology, 2003.

[20] Martin Reiser, “Theory and design of charge particle beams”, John Wiley & Sons. Inc., 1994.

[21] P. M. Lapostelle, “Possible emittance increase through filamentation due to space-charge in continuous beams”, IEEE Transactions on Nuclear Science, NS-18 (3), 1101-1104, 1971.

[22] Frank J. Sachere, “RMS Envelope Equations with Space Charge”, IEEE Transactions on Nuclear Science, NS-18 (3) 1105-1107, 1971.

[23] J.D. Lawson, “The physics of Charged-Particle Beams”, Oxford University Press, 1988.

[24] Michael Rohrs *et al*., “Slice Emittance Measurement at FLASH”, Proceedings of European Particle Accelerator Conference 2006, Edinburgh, Scotland, pp-77.

[25] Robert Joel England, “Longitudinal Shaping of Relativistic Bunches of Electrons Generated by an RF Photoinjector”, Ph. D. thesis, University of California, Los Angles, 2007.

[26] J. B. Rosenzweig, “High brightness electron sources”, Proceedings of XIX International Linear Accelerator Conference 1998, Chicago, USA, pp-344.

[27] F. Zimmermann *et al*., “A final focus system for the next linear collider”, SLAC-PUB-95-6789, June 1995.

[28] R. Brinkmann *et al*., “A low emittance, flat beam electron source for linear collider”, Proceedings of European Particle Accelerator Conference 2000, Vianna, Austria, pp-453.

[29] B. Hafizi and C. W. Roberson, “Effect of emittance and energy spread on a free electron laser in the gain focusing regime”, Physical Review Letters 68, 3539 (1992).

[30] Charles A. Brau, “Free Electron Lasers”, Academic press, Boston, 1990.

[31] Patrick G. O'Shea and Henry P. Freund, “Free electron lasers: status and applications”, Science 292, 1853, 2001.

[32] J. D. Lawson, “Lasers and Accelerators”, IEEE Transactions on Nuclear Science NS-26 (3), 4217- 4219, 1979.

[33] P.M. Woodward, “A method of calculating the field over a plane”, Journal of Electrical Engineering, 93, 1554, 1947.

[34] Thomas P. Wangler, "Principles of RF Linear Accelerator", John Willey & Sons, Inc. 1998.

[35] Samuel Y. Liao, "Microwave Devices and Circuits", Prentice-Hall of India Pvt. Ltd. 1991.

[36] W. Wuensch, "High- Gradient Breakdown in Normal- Conducting RF cavities", Proceedings of European Particle Accelerator Conference 2002, Paris, France, pp -134.

[37] Mathews Jon and Walker R.L., "Mathematical Methods of Physics", W.A. Benjamin, Menlo Park California, 1970.

[38] J. Gao, "Analytical formula for the coupling coefficient β of the cavity-waveguide coupling system", Nuclear Instruments and Methods in Physics Research, A 309 (1991), 5-10.

[39] Edward L. Ginzton, "Microwave Measurements", McGraw-Hill, New York, 1957.

[40] David M. Pozar, "Microwave Engineering", John Willey & Sons (Asia) Pte. Ltd. Singapore, 1989.

[41] F. Caspers, " Basic Concepts II", Proceedings of CERN accelerator School on "RF Engineering for Particle Accelerators", CERN 92-03,Vol.1, Exeter College, Oxford, UK, April 1991, pp-125.

[42] P.H. Smith, "Transmission line calculator", Electronics Vol. 12, No.1, 29-31, 1939.

[43] L. C. Maier and J. C. Slater, "Determination of field strength in a linear accelerator cavity", Journal of Applied Physics, Vol. 23, No.1, 78-83, 1952.

[44] John Byrd, "RF Cavity bead pull measurements", Microwave Measurements Laboratory USPAS and CCAST Beijing, China, 1998.

[45] Arvind Kumar, “Perturbation technique for characteristic impedance measurement of resonant linac structures”, Proceedings of DAE-BRNS Symposium on Nuclear Physics 2002, Vol. 45B, pp- 492.

[46] Walter Schottky, “Uber den Austritt von Elektronen aus Gluhdrahten beiverzogerden Potentialen”, Annalen der Physik, 44, 1011-1032, 1914.

[47] Kwange-Je Kim, “RF and Space Charge effects in Laser Driven RF electron Guns”, Nuclear Instruments and Methods in Physics Research, A 275 (1989), 210-218.

[48] E. Chojnacki, C. Ho, R. Koneckny, AGN-7, 1991.

[49] Luca Serafini and J. B. Rosenzweig, “Envelope analysis of intense relativistic quasilaminar beams in rf photoinjectors: A theory of emittance compensation”, Physical Review E 5, 7565-7590 (1997).

[50] I. S. Lenhrman *et al*., “Design of a high-brightness high-duty factor photocathode electron gun”, Nuclear Instruments and Methods in Physics Research, A 318 (1992), 274-253.

[51] L. Serafini *et al*., “RF gun emittance correction using unsymmetrical RF cavities”, Nuclear Instruments and Methods in Physics Research, A 318 (1992), 275-281.

[52] J. Gao, “A proposal for Multi- Cavity RF Gun System with Small Emittance Growth”, LAL/SERA 90-44, 1990.

[53] J. Gao, “A Cylindrically Unsymmetrical Cavity Used in a Multi- Cavity RF GUN System as an Trail to Reduce Emittance”, LAL/SERA 90-188/RFG, 190.

[54] J. C. Gallardo and R. B. Palmer, “Emittance Correction of Photocathode Gun”, Nuclear Instruments and Methods in Physics Research, A304 (1991) 345-347.

[55] L. Serafini *et. at.*, “Neutralization of the emittance blowup induced by rf time dependent forces in rf guns”, Nuclear Instruments and Methods in Physics Research, A318 (1992), 301-307.

[56] Christian Travier, “An introduction to photo-injector design*”,* Nuclear Instruments and Methods in Physics Research, A340 (1994), 26- 39.

[57] Rosenzweing and Colby, “Charge and wavelength scaling of RF photo-injetcor design”, American Institute of Physics Conference Proceedings 335, 1995.

[58] W. D. Kilpactric, “Criterion for vacuum Sparking Design to Include both rf and dc”, Review of Scientific Instruments, 28 (1957), 824-826.

[59] G. Suberlunq, “Technological Chaleenges for high brightness photo-injectorors” Proceeding of European Particle Accelerator Conference 2004, Lucerne Switzerland, pp - 64.

[60] A. H. Sommer, “Photoemissive materials”, Robert E. Kreiger Publishing Company, New York 1980.

[61] P. A. McIntosh, “RF cavity computer design codes”, Proceedings of Particle Accelerator Conference, Dallas, TX, 1995, (IEEE, Piscataway, NJ, 1995), pp- 2353

[62] J. N. Corlett, “Experience with cavity design programs”, Proceedings of CERN Accelerator School on “RF Engineering for particle accelerators”, CERN 92-03, Vol. II, Exeter College, Oxford, UK, 3-10 April 1991, pp-301.

[63] K. Halbach and R. F. Holsinger, “SUPERFISH- ACOMPUTER PROGRAM FOR EVALUATION OF RF CAVITIES WITH CYLINDRICAL SYMMETRY” Proceeding of Particle Accelerators 1976, Albuquerque, New Mexico, USA, Vol. 7, pp -222.

[64] www.cst.com.

[65] B. Biswas *et al.*, “thermal simulations of a photocathode RF gun”, Proceedings of Asian Particle Accelerator Conference 2007, RRCAT, Indore, India, pp- 482.

[66] www.asnsys.cm

[67] Lloyd M. Young, “Computer code PARMELA”, Los Alamos National Laboratory, Technical report No. LA-UR-96-1835, 1996.

[68] Stan O. Schriber, “Analog Analysis of π-mode structures: Results and implications”, Physical Review Special Topics – Accelerators and Beams 4, 122001(2001).

[69] D. A. Edwards and and M. J. Syphers, “An Introduction to the Physics of High Energy Accelerators”, John Wiley & Sons, Inc., 1993.

[70] Arvind Kumar, K. K. Pant and S. Krishnagopal, “Design and beam dynamics simulations of an S-band photocathode RF gun”, Physical Review Special Topics – Accelerators and Beams 5, 103501 (2002).

[71] D. J. Gibson *et al*., “Electron bean and rf characterization of a low emittance X-band photoinjector”, Physical Review of Special Topics- Accelerators and Beams 4, 090101(2001).

[72] L. Faillance *et al*., “Experimental Characterization of the RF gun Prototype for the SPARX-FEL Project”, Proceedings of International Particle Accelerator Conference 2010, Kyoto, Japan, pp-3688.

[73] Jin-Soo, Roger Miller and Christopher Nantista, “ Design of a standing-wave multicell radio frequency cavity beam monitor for simultaneous position and emittance measurement”, Review of Scientific Instruments, 76, 073302(2005).

[74] J-H Han *et al*., “S-BAND PHOTOCATHODE GUN WITH A 1kHz REPETITION RATE” Proceedings of Linear Accelerator Conference 2010, Tsukuba, Japan, pp-974.

[75] SHI Jia Ru *et al*., “ RF deflecting cavity for bunch length measurement in Tsighua Thomas scattering X-ray source” Chinese Physics C, Vol. 33 Suppl. II, Jun 2009, 161-164.

[76] E. Vlieks *et al*., “ DEVELOPMET OF AN X-BAND PHTOINJECTOR AT SLAC”, Proceedings of Linear Accelerator Conference 2002, Gyeongju, Korea, pp- 164.

[77] Abhay Deshpande *et al*., “Experimental results of an rf gun and the generation of a multibunch beam”, Physical Review of Special Topics- Accelerators and Beams 14, 063501 (2011).

[78] J. B. Rosenzweig *et al*., “RF AND MAGNETIC MEASUREMENTS ON THE SPARC PHOTOINJECTOR ANDSOLENIOD AT UCLA”, Proceedings of Particle Accelerator Conference 2005, Knoxville, Tennessee, pp- 2624.

[79] S. Lal, K. K. Pant, S. Krishnagopal, “A new two-stp tuning procedure for a photocathode gun”, Nuclear Instruments and Methods in Physics Research, A592, 180 (2008).

[80] J. W. Wang, “International X-band Linear Collider Accelerator Structures R&D, SLAC-PUB-13554, February 2009.

[81] Kwok Ko *et al*., “Advances in Parallel Electromagnetic Codes for Accelerator Science and Development”, SLAC-PUB-14349.

[82] N. Terunuma *et al*., “Improvement of an S-band RF gun with a Cs_2Te photocathode for the KEK-ATF”, Nuclear Instruments and Methods in Physics Research, A613 (2010), 1-8.

[83] A. Murata *et al*., “IMROVEMENT OF AN S-BAND RF-GUN CAVITY WITH A CS-TE PHOTOCATHODE”, Proceedings of European Particle Accelerator Conference 2008, Genoa, Italy, pp - 721.

[84] Y. Kamiya *et al.*, "DEVELOPMENT OF AN S-BAND Cs_2Te-CATHODE RF GUN WITH NEW RF TUNERS", Proceedings of Particle Accelerator Conference 2007, Albuquerque, New Mexico, USA, pp - 2808.

[85] S. Rimijaem *et al.*, "TUNING AND CONDITIONING OF A NEW HIGH GRADIENT GUN CAVITY AT PITZ", Proceedings of European Particle Accelerator Conference 2008, Genoa, Italy, pp - 244.

[86] Juho Hong *et al.*, "High-power Beam Test of the Photocathode RF Gun at the Pohang Accelerator Laboratory", Journal of the Korean Physical Society, Vol. 58, No.2, 198-204 (2011).

[87] S. M. Gierman and J.F. Schmerge, "Cold test measurements on the GTF prototype RF gun, LCLS-TN-06-15 (2006).

[88] http://laacg.lanl.gov/laacg/services.

[89] S. J. Park *et al.*, "DESIGN STUDY OF LOW-EMITTANCE INJECTOR FOR SASE XFEL AT PHOHANG ACCELERATOR LABORATORY", Proceedings of Free-Electron Lasers Conference 2004, Trieste, Italy, pp - 179.

[90] J. C. Slater, "Microwave electronics", Van Nostrand, Princeton, NJ, 1950.

[91] J. Gao, "Analytical formula for the resonant frequency changes due to opining apertures on cavity walls", Nuclear Instruments and Methods in Physics Research, A 311 (1992), 437-443.

[92] L. Grant Hector and Donald L. Woernely, "The Dielectric Constants of Eight Gases", Physical Review 69 (1949) 101-105.

[93] M. J. de Loos *et al.*, "Construction of the ALPHA-X photo-injector cavity", LAL/RT 06-15 October 2005.

[94] Shankar Lal, K. K. Pant and S. Krishnagopal, “An analytical formulation for prediction of geometrical dimenions of a photocathode gun for desired RF properties”, Proceedings of International Particle Accelerator Conference 2010, Kyoto, Japan, pp -3679.

[95] Shankar Lal, K. K. Pant and S. Krishnagopal, “A novel scaling law relating the geometrical dimenions of a photocathode RF gunto its RF properties”, Review of Scientific Instruments 82, 123304 (2011)

[96] F. Kiewiet *et al.*, “Femto-second synchronization of a 3 GHz RF oscillator to a mode-locked Ti:Sapphire laser,” Nuclear Instruments and Methods in Physics Research, A 484 (2002), 619–624.

[97] B. Biswas, S. Lal and V. Kumar, “DEVELOPMENT OF IN-VACUUM MIRROR SYSTEM COMPACT MAGNETS AND UNDULATOR BEAAM LINE FOR CUTE-FEL”, Proceeding of Indian Particle Accelerator Conference 2009, RRCAT, Indore, India.

[98] M. Minty, “ Beam Diagnostics”, CERN Accelerator School on “Introduction to Accelerator Physics” CERN 2004, Hotel Schloss Weikersdorf, Baden bei Wien, Austria.

[99] B. Biswas *et al.*, “Signature of build of coherence in an indigenously buit Compact Ultrafast Terahertz Free Electron Laser set-up”, Current Science Vol. 105 No.1, 10 July 2013.

[100] L.D. Hansborough *et al.*, “BRAZING TECHNIQUES FOR SIDE COUPLED ELECTRON ACCELERATOR STRUCTURES”, LA-UR-86-3564, 1996.

[101] Fredericus Bernardus Kiewiet, “Generation of ultra-short, high-brightness relativistic electron bunches”, Ph. D. thesis, Eindhoven University of Technology Netherlands, 2003.

[102] http://www.wer.ir/files/368657BrazingHandbook.pdf and Editor-in-chief: Markku Ainali, “Brazing handbook”, Edition Nr 8, September 2006, Västerås, Sweden.

[103] Ajay Kak, P. K. Kulshreshtha and Shankar Lal, "DEVELOPMENT OF BRAZING TECHNIQUE FOR A 1.6 CELL BNLS/SLAC/UCLA TYPE PHOTOCATHODE RF GUNS BY HYDROGEN BRAZING", Proceedings of Indian Particle Accelerator Conference 2009, RRCAT, Indore, India.

[104] Ajay Kak *et al*., "Brazing of Photocathode RF gun structures in Hydrogen atmosphere: Process qualification, Effect of brazing on RF properties, and Vacuum compatibility", Proceedings of the International Vacuum Symposium 2012, VECC, Kolkata and Journal of Physics: Conference Series 390 (2012) 012025.

[105] V. A. Dolgashev et al., "High Power Tests of Normal Conducting Single cell Structures", SLAC-PUB-12956, 2007.

[106] X. Xu *et al*., "RF breakdown studies in X-band klystron cavities", SLAC-Pun-7505, 1997.

[107] N. A Solyak, "Gradient Limitation in Room Temperature and Superconducting Acceleration Structures", FERMILAB- CONF-08-435-TD, 2008.